UNIVERSITY OF ZAGREB
FACULTY OF SCIENCE
DEPARTMENT OF PHYSICS

IVO PLETIKOSIĆ

ELECTRONIC STATES OF EPITAXIAL GRAPHENE ON IRIDIUM

FROM ALMOST NEUTRAL TO HIGHLY DOPED GRAPHENE

Doctoral Thesis

Zagreb, 2012

SVEUČILIŠTE U ZAGREBU
PRIRODOSLOVNO-MATEMATIČKI FAKULTET
FIZIČKI ODSJEK

IVO PLETIKOSIĆ

ELEKTRONSKA STANJA EPITAKSIJSKOG GRAFENA NA IRIDIJU

OD GOTOVO NEUTRALNOG DO VRLO DOPIRANOG GRAFENA

Doktorski rad

Mentor: dr. sc. Petar Pervan

Zagreb, 2012.

ABSTRACT

Graphene has been grown on the (111) face of iridium as a coherent, single-domain monolayer. Its angle-resolved photoemission (ARPES) spectrum shows intact Dirac cone, marginally p-doped. Fortuitous gap in the bands of Ir(111) at the position of the Dirac cone makes the interaction with the substrate weak, mostly of van der Waals type. Due to the mismatch of the lattices, a moiré superstructure of graphene is formed, that leaves a unique footprint — minigaps in the π band of graphene.

By intercalating alkali atoms, graphene can be n-doped, in steps all up to -1.4 eV. Spectroscopy shows a pronounced renormalization of the π^* band and a step-like change of its width at the kink, 0.2 eV below the Fermi level. The renormalization is due to the coupling to two distinct phonons. High structural quality of graphene and high experimental resolution enabled us to observe an apparent gap at the position of the kink. A self-consistent recursive procedure has been used to extract the bare band, real and imaginary parts of the self energy, and determine the electron-phonon coupling constant.

KEYWORDS: graphene / iridium / moiré superstructure / minigap / electron-phonon coupling / angle-resolved photoelectron spectroscopy (ARPES)

PROŠIRENI STRUKTURIRANI SAŽETAK

UVOD

Grafen

STRUKTURA (IDEALIZIRANA) Ugljik stvara mnoštvo alotropa zahvaljujući različitim mogućnostima hibridizacije vanjskih orbitala $2s$ i $2p_{x,y,z}$. Tako primjerice dijamant nastaje kovalentnim vezanjem orbitala sp^3 usmjerenih prema vrhovima pravilnog tetraedra. Grafit ili pak ugljikove nanocijevi grade hibridi tipa sp^2. Njihova se struktura može uvelike opisati dvodimenzionalnom slagalinom ugljikovih atoma imena grafen, gdje su hibridne orbitale sp^2 kovalentno vezane tvoreći σ veze u ravnini pod kutovima od 120°, a preostale orbitale p_z strše okomito na ravninu. Jedinična ćelija strukture dobivene vezanjem ugljika u šesterokutne saćaste oblike sastoji se od dvaju atoma. Oba dijele jednaku kemijsku okolinu, međutim njihove veze sa susjednim atomima su zrcalno simetrične. Stoga je uobičajeno na strukturu grafena gledati kao na dvije trigonalne isprepletene mreže atoma — mrežu atoma A i mrežu atoma B međusobno pomaknute u ravnini za duljinu veze dvaju ugljika. Pokazuje se da upravo takva struktura grafenu daje najvažnija obilježja, posebno kad su u pitanju elektronske vrpce π stvorene tuneliranjem među orbitalama p_z.

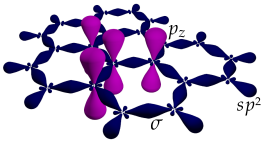

ELEKTRONSKA STRUKTURA (IDEALIZIRANA) Struktura elektronskih vrpca grafena najčešće se razmatra u približenju čvrste veze (eng. *tight binding approximation*). Linearna kombinacija atomskih orbitala p_z napravi se takvom da zadovoljava Blochov uvjet o diskretnoj periodičnosti, uvrsti u Schrödingerovu jednadžbu sastavljenu od atomskih Hamiltonovih funkcija i kristalnog potencijala kao popravka do stvarne Hamiltonove funkcije. Popunjena vrpca π i nepopunjena vrpca π^* koje se dobiju kao dva rješenja ovog problema simetrične su s obzirom na ishodište u energiji, dodiruju se u šest točaka naizmjenično zvanih K i K′, u uglovima šesterokutne Brillouinove zone, a disperzija im je u okolini tih točaka brza, izotropna i najvažnije — linearna. Pokazuje se da je valnu funkciju elektrona u vrpcama π moguće reducirati na doprinose po dvjema podrešetkama, a zatim u granici niskih energija te valnih duljina uz granicu Brillouinove zone i po indeksu pripadnosti dolini (stošcu) u neekvivalentnim točkama K i K′. Prvi rastav uvodi razlikovanje po kvantnom broju pseudospina, a drugi po izospinu; valna se funkcija može raspisati kao spinor u Diracovoj jednadžbi za bezmasene fermione. Ovakve se čestice nazivaju Diracovim fermionima, a šest točaka u recipročnom prostoru

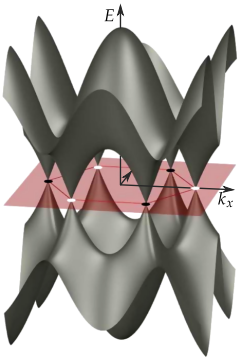

Diracovim točkama. Dalje od područja primjenjivosti ovog modela stožaste vrpce ipak prestaju biti izotropne, i dolazi do njihovog iskrivljavanja u tri smjera visoke simetrije, prema takozvanim točkama M recipročnog prostora popločanog Brillouinovim zonama u proširenoj shemi. U tim točkama brzina vrpca iščezava, dovodeći gustoću stanja po energiji u van Hoveove singularitete.

SVOJSTVA GRAFENA Posljedice ovakve strukture elektronskih vrpca, kao i strukturne postojanosti omogućene jakim σ vezama vidljive su u mnogim makroskopskim svojstvima grafena. ◇ Sposobnost ambipolarnog vođenja električne struje dolazi kao posljedica simetrije dviju π vrpca i nepostojanja energijskog procjepa među njima. Primjenom vanjskoga polja nosioce naboja moguće je izmjenjivati između šupljina u djelomično ispražnjenoj π vrpci i elektrona u punjenoj π^* vrpci. Krivulja otpornosti je simetrična s obzirom na izmjenu polariteta polja odnosno dopiranja vrpca, svjedočeći ekvivalentnost vođenja šupljinama i elektronima. ◇ Mobilnosti nosilaca naboja u grafenu dosežu i do 200000 $cm^2V^{-1}s^{-1}$ te se ne mijenjaju značajno od vrlo niskih pa do sobne temperature. Ostaju visoke i uz jako dopiranje, bilo električnim poljem bilo adsorbiranim dopandima. Ovim se potvrđuje balističko vođenje na mikrometarskim skalama, odnosno činjenica da su raspršenja naboja rijetka a njihovo gibanje u električnom polju ubrzano duž tolikih udaljenosti. ◇ Premda Fermijevu plohu neutralnog grafena čini samo šest točaka, a tamo iščezava i gustoća stanja, vodljivost mu ne prestaje nego pokazuje vrijednosti kvanta vodljivosti $\frac{e^2}{\hbar}$ po svakom od moguća dva spina i dva izospina (ukupno $4\frac{e^2}{\hbar}$). ◇ Dok su u dvodimenzionalnim materijalima s kvadratnom disperzijom vrpca Landauovi nivoi raspoređeni linearno s magnetskim poljem, u grafenu se njihova energija mijenja s kvadratnim korijenom polja, a postoji i stanje nulte energije s polovicom degeneracije ostalih nivoa. Mijenjajući popunjenost trenutno najvišeg nivoa pomicanjem Fermijeve energije dopiranjem ili degeneraciju nivoa promjenom toka magnetskog polja, dobivaju se poznate oscilacije u magnetizaciji (de Haas – van Alphen) i otpornosti (Šubnikov - de Haas) te kvantni Hallov efekt. ◇ Posebnost kvantnog Hallovog efekta u grafenu proizlazi iz postojanja Landauovog nivoa nulte energije. Zasićenja transverzalne vodljivosti događaju se na polucjelobrojnim vrijednostima kvanta vodljivosti $4\frac{e^2}{\hbar}$, dok na istim vrijednostima gustoće naboja longitudinalna otpornost iščezava (pokazujući kad su Landauovi nivoi popunjeni). Kvantni Hallov efekt koji se opaža čak i na sobnoj temperaturi uzima se za najjasniji dokaz postojanja Diracovih fermiona u grafenu.

PROIZVODNJA GRAFENA Budući da se slabo vezani slojevi grafena u prirodi nalaze kao sastavni dio grafita, prva ideja o dobivanju izoliranog sloja bila bi ona o njegovom izljuštenju. Koliko god ideja bila

jednostavna, tek je grupa Geima i Novoselova 2004. uspjela dobiti i prepoznati jednosloj među ostacima višeslojnih dijelova odljuštenih ljepljivom trakom i prebačenih na SiO_2. Uslijedila su prva mjerenja transportnih i optičkih svojstava na uzorcima veličine desetak mikrometara, a na nekima od njih su dobivene i već spomenute izvanredno velike mobilnosti. Ovakav način proizvodnje davao je uzorke vrlo malih dimenzija i to među višeslojnim ostacima.

Drugi je način dobivanja bio sublimacijom silicija s površine SiC(001) u vakuumu na temperaturama iznad 1600 K, a zatim i poboljšanom metodom u atmosferi argona na 1900 K koja je polučila homogeni jednosloj. Pod njim se međutim u oba slučaja nalazio ugljikov sloj rekonstrukcije ($6\sqrt{3}\times 6\sqrt{3}$), a elektronske su vrpce bile intrisično dopirane, pa se njihovo sjecište u Diracovoj točki nalazilo 0.45 eV ispod Fermijevog nivoa. Po udaljenosti grafenskog sloja od supstrata dade se zaključiti i da je vezanje za podlogu poprilično jako. Pokušaj proizvodnje na drugoj strani istoga kristala, onoj u smjeru ugljikovih ravnina u SiC, dalo je višeslojne grafenove slojeve među kojima je interakcija, vjerojatno zbog međusobne zakrenutosti slojeva, bila tako mala da su izmjerene vrpce bile jednostavni Diracovi stošci, a ne vrpce kakve se inače nalaze u grafitu.

Premda se smatra da je grafen moguće iskoristiti samo kad se nalazi na izolatorskoj podlozi, to ipak ne znači da se on na takvoj mora i proizvoditi. Rast grafena na površinama prijelaznih metala odavno je poznat, i obično je uziman za smetnju prilikom dobivanja čistih površina. Uspjeh grafena nakon prve karakterizacije njegovih svojstava obnovio je odmah i interes za epitaksijski grafen na metalnim površinama, a u nadi da će ga se moći od njih odvojiti. Dva su načina dobivanja: bilo izlučivanjem ugljika iz volumena kristala na površinu, bilo raspadom spojeva koji sadrže ugljik (raznih ugljikovodika, primjerice). Prvom je metodom teško izbjeći pojavljivanje više slojeva grafena odjednom, jer bi se takav rast mogao zaustaviti samo ograničenjem izvora ugljika i preciznom kontrolom vremena i temperature rasta. U drugoj metodi, molekule ugljikovodika se raspadaju katalitičkom reakcijom na površini metala pri povišenoj temperaturi, a ugljik koji preostane stvara rastuće otoke grafenske strukture. Takav grafen je na površinama Ni(111), Ru(001), Co(001) i Pd(111) poprilično jako vezan, udaljen od njih za manje od polovice udaljenosti slojeva u grafitu, a izmjerene π vrpce izobličene, pomaknute na više vezivne energije i sa zamjetnim energijskim procjepom tamo gdje bi se očekivalo njihovo sjecište. Potpuno drugačiji je grafen na površinama Pt(111), Cu(111), Ag(111) i Ir(111): udaljenost od supstrata tu je usporediva s udaljenostima ploha u grafitu, a elektronske vrpce su uglavnom samo pomaknute u energiji zbog dopiranja elektronima ili šupljinama iz supstrata.

Za grafen na iridijevoj površini (111) pokazuje se da ga je moguće dobiti u jedinstvenoj orijentaciji s obzirom na supstrat, tako da se

glavne osi obiju rešetaka poklapaju. Ključan korak u rastu je stvaranje prvih otoka grijanjem adsorbiranog etena na temperaturi od 1600 K, dok daljnji rast može ići bilo kontinuirano, bilo mnogobrojnim u koracima s adsorpcijom ugljikovodika na sobnoj temperaturi pa snažnim zagrijavanjem. Grafen tada jednolično prekriva gotovo makroskopske površine, zadržavajući koherenciju i preko rubova terasa prisutnih na supstratu. Upravo će ova svojstva biti iskorištena u istraživanju π vrpca grafena naraslog na Ir(111), metodom kutnorazlučive fotoelektronske spektroskopije (ARPES), budući da je za nju zbog usrednjavanja po većoj površini homogenost strukture jedan od važnijih preduvjeta.

Geometrija grafena na Ir(111)

Tunelirajuća mikroskopija (STM) otkriva da je površina iridija, kao supstrata na kojem raste grafen, nerekonstruirana heksagonalna mreža atoma s jediničnom ćelijom veličine 0.272 nm, dok jedinična ćelija grafena ima veličinu 0.246 nm. Obje su ćelije jednako orijentirane. Zbog nepodudaranja njihovih veličina od ~10% dolazi do pravilnog mreškanja grafenskog sloja, u takozvanoj moiré superstrukturi dimenzije 2.53 nm. Kontrast se u mikroskopiji mijenja kako ugljikovi atomi mijenjaju svoj položaj prema atomima iridija u površinskom sloju, no nije samo uzrokovan geometrijom nego se primjećuje i preraspodjela gustoće elektrona.

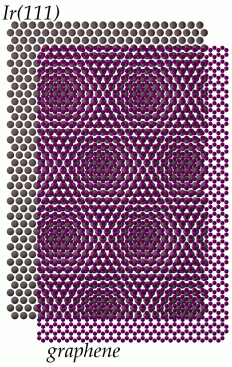

Dokaz postojanja superperiodičnosti nalazi se i u difrakcijskim slikama (LEED), gdje su oko maksimuma u uglovima jednako orijentiranih šesterokuta proizašlim iz difrakcije na periodičnostima atoma iridijeve površine (111) i grafena, prisutne i dodatne točke raspoređene na uglovima deseterostruko manjih šesterokuta. One su često vidljive i u višim redovima difrakcije, svjedočeći tako dugosežnu pravilnu strukturnu uređenost grafena.

Oblik i veličina Brillouinovih zona za Ir(111) i grafen mogu se odrediti i iz realnog i iz recipročnog prostora. Brillouinove zone su šesterokutne, jednako orijentirane, ali je iridijeva oko 10% manja od grafenove. Tako se K točke iridijeve zone nalaze na 1.53 $Å^{-1}$, a grafenove na 1.70 $Å^{-1}$ od centra Brillouinove zone Γ.

elektronska spektroskopija grafena na ir(111)

Podloga: Ir(111)

Za heterostrukture je često poželjno da slabo interagiraju sa supstratom. Jedan od preduvjeta za to može biti i nepostojanje podudarnih elektronskih stanja koja bi se iz nadstrukture širila u dubinu supstrata. To se može ostvariti ili različitom simetrijom stanja, ili nepostojan-

jem stanja u supstratu na pojedinim područjima u faznom prostoru (E, $k_{||}$) gdje postoje stanja nadstrukture.

Pri istraživanju elektronskih stanja nadstrukture poželjno je zato znati osobine površinske projekcije stanja iz dubine supstrata. Budući da fotoelektronski spektri u ARPES-u predstavljaju superpoziciju nekoliko vršnih atomskih slojeva uzorka, karakterizacija stanja supstrata, promijenjenih ili nepromijenjenih dodanom nadstrukturom, potrebna je i iz tog razloga.

Spektri Ir(111) pokazuju mnoštvo vrpca centriranih u ishodištu Brillouinove zone čije se vezivne energije mijenjaju s energijom pobude u ARPES-u. To pak znači da većina njih dolazi od emisije iz dubinskih stanja s trodimenzionalnom disperzijom. Neka pak stanja ne pokazuju ovisnost o pobudnoj energiji, pa ih se može smatrati stanjima dvodimenzionalnog karaktera lokaliziranim uz površinu. Područja u spektrima gdje se nalaze takva stanja obično su ona gdje ne postoje projekcije dubinskih vrpca na površinu, u takozvanim energijskim procjepima. Računi u teoriji funkcionala gustoće zaista potvrđuju takve procjepe. Nama će najznačajniji biti onaj u blizini točke K u Brillouinovoj zoni za Ir(111). Pokazuje se da je on tolike veličine da se proteže i do K točke u Brillouinovoj zoni grafena, a u energiji dublje od 1 eV ispod Fermijevog nivoa.

Elektronska struktura grafena na Ir(111)

Narastanjem grafena u ciklusima adsorpcije etena i njegove termolize na 1600 K u spektrima s površine iridija pojavljuje se Diracov stožac, odnosno cijela π vrpca. Stožac kojem se vršak nalazi na 1.70 $Å^{-1}$ prolazi energijskim procjepom u vrpcama iridija. Prilagodbom krivulje dobivene za disperziju π vrpce u približenju čvrste veze na eksperimentalnu vrpcu dobije se da je ona blago dopirana šupljinama, tj. pomaknuta na više energije za ~0.1 eV, da je preklop susjednih orbitala p_z uistinu malen, te da je energija preskoka između susjednih orbitala od -2.848 eV vrlo blizu vrijednosti dobivenoj u teoriji funkcionala gustoće za samostojeći grafen. Možemo reći da grafen slabo interagira sa supstratom jer se ne vidi zakrivljenje vrška konusa i otvaranje procjepa među π vrpcama kakvo postoji kad su supstrati Ni(111) ili Ru(001). Računi također ukazuju na slabo vezanje, uglavnom van der Waalsovog tipa. Neobična odlika spektara grafena na Ir(111) su replike Diracovog stožaca na šest mjesta u njegovoj okolini. Ispostavlja se da su posljedica difrakcije, odnosno promjene zaleta elektrona u iznosima recipročnih vektora superperiodične strukture grafenovog moiréa. Uz to se, na mjestima gdje replike sijeku osnovni stožac u njemu otvaraju tzv. minigapovi, i to kao posljedica izbjegnute hibridizacije vrpca. Širina minigapova kreće se od 100 do 200 meV, a te vrijednosti nam daju i procjenu jačine superperiodične komponente kristalnog potencijala u grafenu nastale uređenjem u moiré.

Dopiranje grafena elektronima

Jakim elektronskim dopiranjem grafena dovodimo vrpcu π^* na Fermijev nivo tamo gdje se njena gustoća stanja u energiji jako povećava, približavajući se van Hoveovom singularitetu. U spektrima ARPES-a primjećuje se renormalizacija vrpce s naglim lomom odnosno smanjenjem brzine disperzije iznad energija od cca. -0.2 eV. Renormalizacija potječe od vezanja elektrona u vrpci na fonone, što onda smanjuje energiju vezanja elektrona u tom području energija. Drugi učinak na spektre dolazi od rekombinacije šupljine stvorene fotoemisijom uz asistenciju fonona. U takvim procesima sudjeluju elektroni, što znači da je rekombinacija moguća samo na energijama nižim od onih -0.2 eV, pa ispod mjesta pregiba vrpce dolazi do skoka u širini spektralnih krivulja.

Budući da dolaze iz istoga izvora, oba se efekta mogu iskoristiti u procjeni jačine vezanja elektrona s fononima u grafenu. Ovdje smo za to upotrijebili novu metodu koja poboljšava samosuglasnost realnog i imaginarnog dijela vlastite energije preko Kramers-Kronigovih relacija rekurzivno rafinirajući neinteragirajuću (golu) vrpcu.

Kada se grafenu na Ir(111) doda kalij i sistem blago zagrije iznad sobne temperature, kalij prelazi ispod grafenskog sloja i stvori uređene strukture 2×2 ili $\sqrt{3}\times\sqrt{3}$ u odnosu na površinu iridija. Budući da je izrazit donor elektrona, on napuni grafensku π^* vrpcu toliko da je spusti za oko 1.4 eV (0.05 elektrona po jediničnoj ćeliji). Pritom se moiré superstruktura grafena izgubi, i on postane poprilično ravan. Birajući povoljnu polarizaciju pobude – ultraljubičastog svjetla – grana K-M vrpce π^* snimljena je u izvrsnom razlučenju. Oko pregiba je uočeno udvostručenje vrpca za koje se pokazuje da dolazi od stvaranja složene kvazičestice elektron-fonon na rezonantnoj energiji jednog optičkog fonona od ~170 meV. Rekurzivna procedura ukazuje na skok u imaginarnom dijelu vlastite energije od 55 meV na energiji tog fonona, i za prvu procjenu konstante elektron-fonon vezanja λ daje približno 0.17, u oba smjera visoke simetrije K-Γ i K-M. Takva se procjena može dobiti i iz promjene brzine na Fermijevom nivou od neinteragirajuće do renormalizirane vrpce, i za oba je smjera podjednaka, oko 0.2. U imaginarnom i realnom dijelu vlastite energije, jednako kao i u promjenama spektralnog intenziteta duž vrpce može se uočiti da u vezanju na elektrone sudjeluje još jedan fonon, energije oko 75 meV. Po svemu sudeći njegov je doprinos renormalizaciji manji od doprinosa fonona od 170 meV.

ZAKLJUČAK

Osim što sam po sebi predstavlja zanimljiv sistem zbog superperiodične uređenosti i tragova koje ona ostavlja na vrpce, grafen na (111) površini iridija je zbog velike strukturne uređenosti primjeren i za

općenitija istraživanja, posebno mnogočestičnih interakcija s fononima. U takvoj smo studiji, promatrajući renormalizaciju vrpca grafena, uspjeli doći do pouzdanih vrijednosti konstante elektron-fonon vezanja u jako dopiranom grafenu. Procedura koju smo pritom razradili pokazala se učinkovitom i jednostavnom te će se moći koristiti i za druge sisteme s jakim elektron-fonon vezanjem.

DECLARATION

The work presented in this thesis has been conducted at the Institute of physics in Zagreb under the supervision of dr. sc. Petar Pervan. The results have been published in several peer reviewed articles. Article references for each chapter of the thesis are given below.

Chapter 3 — The substrate: Ir(111)

> I. Pletikosić, M. Kralj, D. Šokčević, R. Brako, P. Lazić, P. Pervan: *Photoemission and density functional theory study of Ir(111); energy band gap mapping*. Journal of physics: Condensed matter **22** (2010), 135006

Chapter 4 — Electronic structure of graphene on Ir(111)

> I. Pletikosić, M. Kralj, P. Pervan, R. Brako, J. Coraux, A. N'Diaye, C. Busse, T. Michely: *Dirac cones and minigaps for graphene on Ir(111)*. Physical Review Letters **102** (2009), 056808

> M. Kralj, I. Pletikosić, M. Petrović, P. Pervan, M. Milun, A. N'Diaye, C. Busse, T. Michely, J. Fujii, I. Vobornik: *Graphene on Ir(111) characterized by angle-resolved photoemission*. Physical Review B **84** (2011), 075427

Chapter 5 — Electron doping of graphene

> I. Pletikosić, M. Kralj, M. Milun, P. Pervan: *Finding the bare band: Electron coupling to two phonon modes in potassium-doped graphene on Ir(111)*. Physical Review B **85** (2012) 155447

CONTENTS

ACRONYMS

ARPES	Angle-resolved photoelectron spectroscopy
CVD	Chemical Vapor Deposition
DFT	Density Functional Theory
EDC	Energy Distribution Curve
FWHM	Full width at half maximum
LEED	Low-energy electron diffraction
MDC	Momentum Distribution Curve
STM	Scanning tunneling microscopy
TBA	Tight Binding Approximation
TPG	Temperature Programmed Growth

PROLOGUE

The first realization of a truly two-dimensional material! – cried the news, *Relativistic physics of massless particles on a piece of paper!* Graphene was born! Though it existed in laboratories[1,2,3], was theoretically investigated[4,5,6], even given a name[7] decades before, though it was hidden in pencil marks for centuries. But it was only in 2004 that graphene was isolated as a monolayer by the University of Manchester group of Geim and Novoselov[8,9,10] and its potential recognized for technological advances and fundamental research.

Graphene /ˈgræf.iːn/ is a name for atomically thin layer of carbon atoms in a honeycomb structure which is sufficiently isolated from its environment to be considered free-standing. Stacked together graphene layers form naturally occurring allotrope of carbon called graphite /ˈgræfaɪt/.

It their top-down approach, the group of Geim and Novoselov succeeded in what was long considered impossible — by repeatedly cleaving a graphite crystal with an adhesive tape they obtained monoatomic samples on an oxidized silicon wafer and made first transport measurements, receiving much attention by peculiar results under magnetic field. The discovery of an atom-thick defect-free material showing extremely mobile massless charge carriers resembling Dirac fermions,[10,11] started one of the fastest growing fields of research in condensed matter physics. Findings just poured in: anomalous quantum Hall effect; ballistic transport; the apparent existence of a minimal conductivity in a sheet with vanishing electron density; absence of the Anderson localization due to relativistic tunneling; capable of controllable gap opening in its narrow stripes; having high thermal conductivity; being one of the strongest materials ever measured (comparable in strength with diamond), yet one of the softest and highly impermeable as a membrane... The discovery also encouraged many on remembering some old techniques of producing epitaxial graphene layers on metal surfaces from external sources of carbon, or on metal carbides by controlled sublimation of contained metals, and a race to produce large enough high-quality samples began. The race should be soon turned on finding ways to produce patterned graphenes. While the big homogeneous samples could outperform indium tin oxide in modern light emitting displays, nanoelectronics can only use building blocks of nanometer extent. That is where the questions of gap opening will emerge, as well as achieving better on/off current ratio, which is still too low. Needless to say, the task of making reproducible nanostructures whose properties strongly de-

pend on positions and bonds between just a few tens of atoms is not easy at all.

We should probably leave technological aspects to true technologists at this time, and see what we can say about physics of graphene. Be it a technological hype or not, graphene is interesting for its fundamental properties just as well. Physicists should therefore explore its structure, all possible interactions within it and its interactions with various substrates.

In this thesis we will investigate graphene epitaxially grown on the (111) surface of iridium, primarily its electronic structure, possible interactions with the supporting substrate, and the impacts that enforced electron doping has on its bands. The thesis is organized as follows:

In the first introductory chapter, we give an overview of the basic properties of graphene. Starting with the very definition of its structure, we continue by describing its electronic bands, the most notable consequences they leave to transport properties, and ways of producing graphene. In Chapter 2 the geometry of graphene grown on the (111) surface of iridium is described in both real and reciprocal space, special attention being given to the properties that will serve in describing the electron spectra in the following chapters.

The main part of the thesis, that on electron spectroscopy of graphene on Ir(111), starts with spectroscopic characterization of the substrate in Chapter 3, which is a necessity since the features of the band structure of the substrate will appear in the spectra when graphene is added. Chapters 4 and 5 bring the main points of the thesis. Chapter 4 is on the electronic structure of graphene, and the changes its superstructural ordering has brought to it. Chapter 5 brings more complexity to the system, by electron doping of bands through alkali intercalation. A striking change of the bands is observed due to electron-phonon coupling, and a contribution to the general discussion on the strength of the coupling is given.

Part I

INTRODUCTION

1 GRAPHENE

Owing to the possibility of various hybridizations of its outer atomic orbitals ($2s$ and $2p_{x,y,z}$), carbon exhibits a wealth of allotropes. Diamond is a three-dimensional crystal formed by sp^3 orbitals whose major lobes have tetrahedral geometry. Carbyne consists of sp hybrid orbitals that are linear chains with alternating single and triple bonds. Graphite or carbon nanotubes are built out by hybrid orbitals of sp^2 type. It is their two-dimensional building block, called graphene, that we shall deal with in the following.

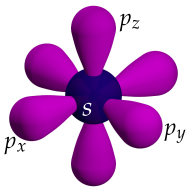

$s+p_{x,y,z}$

1.1 STRUCTURE (IDEAL)

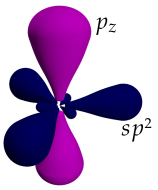

sp^2+p_z

The structure of graphene is usually understood in terms of σ bonds that form between sp^2 hybrid orbitals of carbon. This understanding, however, comes only *a posteriori*, as the linear combination of an s and two p orbitals has been made such that the bond directions reproduce those in graphene — that they are planar, and at angles of 120° to each other. Figure 1 shows how graphene is built: σ bonds form the characteristic hexagons of carbon atoms in a plane, while the dangling p_z orbitals stick out, at the positions of carbon nuclei and to both sides of the plane. It is then the extraordinary strength of the σ bonds that gives graphene robustness, while the tunneling between the p_z orbitals becomes responsible for the electrical properties.

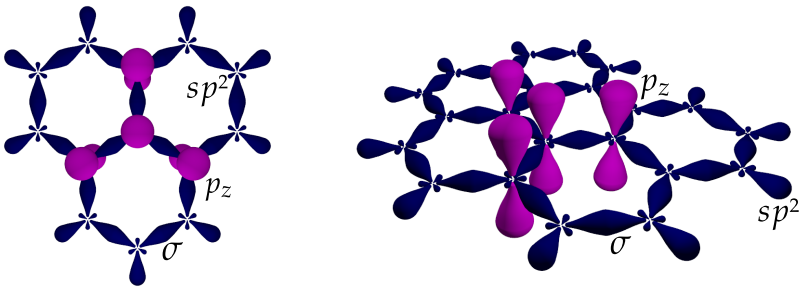

Figure 1: Characteristic appearance of graphene's honeycomb lattice is formed when sp^2 hybrid orbitals of carbon bind into planar σ bonds. The p_z orbitals remain sticking out of the plane. Only one p_z orbital with its three first neighbors is shown here for clarity.

Aerial view onto a region of a two-dimensional crystal of graphene, Figure 2, allows us to identify repeating elements that form the structure. It can be seen that the primitive unit cell consists of two carbon atoms. The two atoms share the same chemical neighborhood except that their bonds to neighboring atoms are mirror images of each other.

The crystal can be thought of as if consisting of two interpenetrating trigonal networks of A and B atoms — a fact that will have consequences in the wave function of conducting electrons, as we will see later.

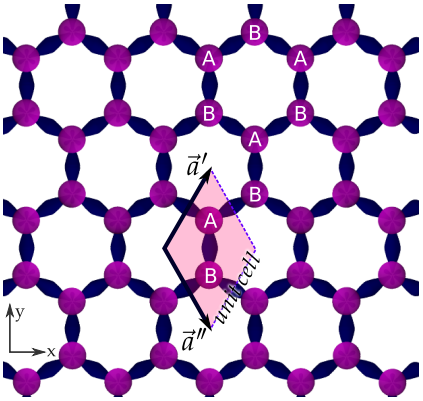

Figure 2: A two-dimensional lattice of graphene is obtained by repeating the unit cell consisting of two atoms (A and B) by primitive translation vectors $\vec{a}' = \frac{a}{2}[1, \sqrt{3}]$ and $\vec{a}'' = \frac{a}{2}[1, -\sqrt{3}]$.

The construction of the reciprocal net associated with the repeating network of two-atom unit cells of graphene starts by identifying the reciprocal vectors corresponding to the primitive vectors of the real-space structure. Vector $\vec{g}'$ is then, by definition, perpendicular to $\vec{a}''$ and the length of its projection to $\vec{a}'$ is $2\pi a$; vector $\vec{g}''$ is calculated in a similar way. The reciprocal net — a set of points obtained by translating the origin (Γ) by any combination of the two reciprocal vectors — can be seen in Figure 3. From it, a construction of Brillouin zone is easily made, and the whole reciprocal space pawed with Brillouin zones in the extended scheme. A few high-symmetry points at the border of Brillouin zone are labeled for convenience: the M points are at the middle of the sides, whereas the K points are at the corners of the zone. Only opposing M points (two M′, M″ and M‴ at a time) are equivalent in a sense that they can be connected by a combination of reciprocal lattice vectors, the same is true for three K and three K′ points separately.

1.2 ELECTRONIC STRUCTURE (IDEAL)

Tunneling between the atomic p_z orbitals forms π bands in graphene. A general idea on the structure of the π bands can be inferred from the tight binding calculation, where a linear combination of all the p_z orbitals of a crystal is taken. Each of these is positioned inside a unit cell at $\vec{R}_c$ and belongs either to sublattice A or B (labeled as $b = A, B$). The atomic orbitals $\left|\vec{r} - \vec{R}_c - \delta_b\right\rangle$ can be simply denoted $\left|b\,\vec{R}_c\right\rangle$, bearing in mind their dependence on $\vec{r}$ and the phase emerging from the

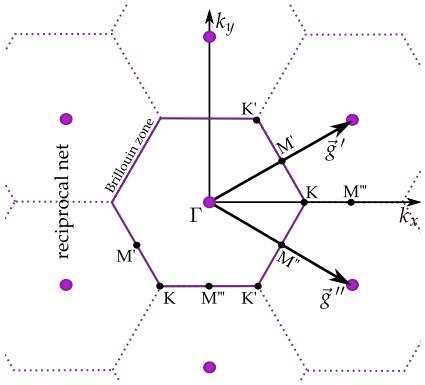

Figure 3: The reciprocal net of graphene obtained by translating the origin Γ by reciprocal vectors $\vec{g}' = \frac{2\pi}{a}[1, \sqrt{\frac{1}{3}}]$ and $\vec{g}'' = \frac{2\pi}{a}[1, -\sqrt{\frac{1}{3}}]$. Drawn is also a set of Brillouin zones in the extended scheme, having high-symmetry points labeled by K and M.

positions δ_b of the two atoms in the unit cell. Respecting the discrete translational symmetry, one obtains for the wave function

$$\left|\mu\vec{k}\right\rangle = \sum_c e^{i\vec{k}\vec{R}_c} \sum_{b=A,B} f_{\mu b} \left|b\,\vec{R}_c\right\rangle \tag{1.1}$$

The wave function depends on a set of quantum numbers μ and the wave vector $\vec{k}$.

The wave function is inserted into the Schrödinger equation where the hamiltonian consists of a set of atomic hamiltonians centered at the positions of atomic nuclei, $\mathscr{H}_o$, and a crystal potential $\mathscr{V}$ that is a difference of a true hamiltonian and $\mathscr{H}_o$. Multiplying the equation by $\left\langle b'\,\vec{R}_o\right|$ one attains

$$\sum_{b=A,B} f_{\mu b} \sum_c \left\{ \left\langle b'\,\vec{R}_o\right| \mathscr{H}_o + \mathscr{V} \left|b\,\vec{R}_c\right\rangle - \left\langle b'\,\vec{R}_o\right| E_\mu \left|b\,\vec{R}_c\right\rangle \right\} e^{i\vec{k}\vec{R}_c} = 0$$

As two choices for b' exist (A and B), two equations for $f_{\mu A}$ and $f_{\mu B}$ are written, and a nontrivial solution for the coefficients sought. Naming

- $\varepsilon_o = \left\langle A\,\vec{R}_o\right| \mathscr{H}_o \left|A\,\vec{R}_o\right\rangle$ the energy of the atomic orbital,
- $\alpha = \left\langle B\,\vec{R}_o\right| A\,\vec{R}_c\right\rangle$ the overlap between the adjacent atomic orbitals,
- $\beta = \left\langle A\,\vec{R}_o\right| \mathscr{V} \left|A\,\vec{R}_o\right\rangle$ the atomic level shift due to the potential coming from the neighboring atoms,
- $\gamma = \left\langle B\,\vec{R}_o\right| \mathscr{V} \left|A\,\vec{R}_c\right\rangle$ the tunneling matrix element between the orbitals on two adjacent atoms,

one finally has for the energy dispersion

$$E_\mu(\vec{k}) = \varepsilon_o + \frac{\beta \pm \gamma\sqrt{s(\vec{k})}}{1 \pm \alpha\sqrt{s(\vec{k})}} \tag{1.2}$$

Here, $s(\vec{k}) = 3 + 2\cos\vec{k}\,\vec{a}' + 2\cos\vec{k}\,\vec{a}'' + 2\cos\vec{k}\,(\vec{a}' + \vec{a}'')$ is a structure factor emerging from the positions of the cells containing three neighboring orbitals (cf. Figure 1).

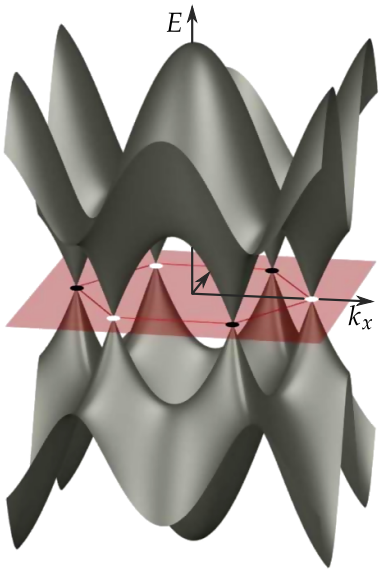

Figure 4: Tight-binding π bands for the allowed energies of p_z electrons in a two-dimensional graphene, $E(k_x, k_y)$. Brillouin zone is depicted in the (k_x, k_y) plane as a hexagon having 3+3 equivalent corners.

The bands obtained in eq. 1.2 are readily depicted in a graph where the components of the wave vector $\vec{k} = [k_x, k_y]$ are in the x-y plane, and the energy along the z direction. Figure 4 shows the bands when the parameters are chosen such that the bands are symmetric with respect to zero energy. The lower π band can accommodate all the available electrons and is completely filled, while the upper band, usually designated as π^*, remains empty. The six points where the bands intersect are the corners of the Brillouin zone, so-called K points. Although only three + three of these are equivalent in a sense that they can be connected by a reciprocal lattice vector, the bands are the same at all six points.

Tight-binding wave function from equation 1.1 can be divided into two parts, each belonging to one of the two sublattices,

$$\left|\mu\vec{k}\right\rangle = f_{\mu A}\,|A\rangle + f_{\mu B}\,|B\rangle \tag{1.3}$$

where $|A\rangle \equiv \sum_c e^{i\vec{k}\vec{R}_c}\left|A\,\vec{R}_c\right\rangle$ and $|B\rangle \equiv \sum_c e^{i\vec{k}\vec{R}_c}\left|B\,\vec{R}_c\right\rangle$. The two parts are orthogonal when the overlap of the adjacent atomic orbitals is

negligible, i.e. when $\alpha = 0$, which usually shows to be true. When $\alpha = 0$, having $\varepsilon_o = \beta = 0$ in equation 1.1 is just the matter of choosing an energy reference. As the wave function is spun by $|A\rangle$ and $|B\rangle$, those can be used as a basis in which to express the hamiltonian:

$$\left|\mu\vec{k}\right\rangle = \begin{pmatrix} f_{\mu A} \\ f_{\mu B} \end{pmatrix}, \qquad \mathscr{H} = \gamma \begin{pmatrix} 0 & \mathcal{S} \\ \mathcal{S}^* & 0 \end{pmatrix} \tag{1.4}$$

where $\mathcal{S} = 1 + e^{-i\vec{k}\vec{a}'} + e^{+i\vec{k}\vec{a}''}$, and $\mathcal{S}^*$ its complex conjugate. Obviously, $E_\mu = \pm\gamma\sqrt{\mathcal{S}\mathcal{S}^*}$. Comparing with equation 1.2, $s(\vec{k}) = \mathcal{S}\mathcal{S}^*$.

Note that this decomposition enables labeling of the electronic states of graphene by so-called pseudospin quantum number, wave function having more weight in one or the other sublattice depending on the mixture of pseudospin states.

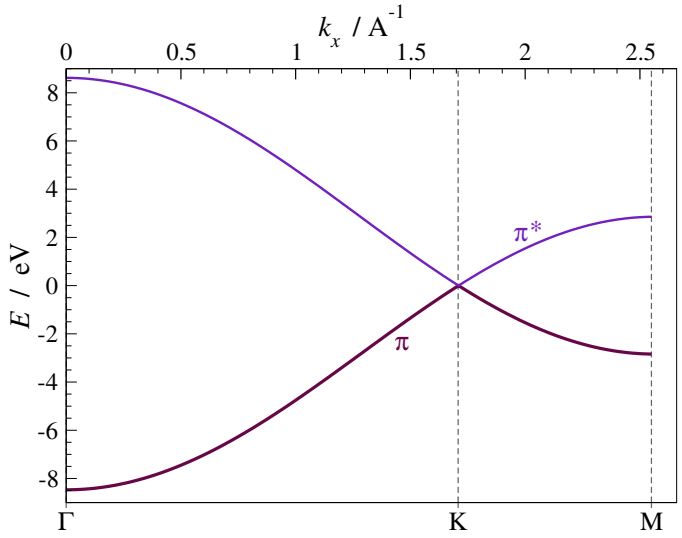

Figure 5: Tight-binding π bands of graphene along the high-symmetry direction Γ–K–M. The TBA parameters set to equation (1.2) were $\varepsilon_o = 0\,\text{eV}$, $\alpha = 0$, $\beta = 0\,\text{eV}$, $\gamma = -2.8\,\text{eV}$.

A cut of the bands along the k_x direction, starting from the Γ point of the Brillouin zone, continuing through K all to the M point, Figure 5, illustrates an important property that graphene has become famous for: in the vicinity of the K point where they only touch with their apexes, the bands π and π^* are highly *linear*. As we will see later, this has a profound effect on all the physics of graphene. The linearity can be shown by expanding the hamiltonian around all the K (K′) points where the band energy vanishes; writing their positions as $\vec{K}^\xi_{mn} = \xi\frac{\vec{g}'+\vec{g}''}{3} + m\,\vec{g}' + n\,\vec{g}''$ ($\xi = \pm 1$ represents a valley index, K or K′) and expanding by $\vec{q} = \vec{k} - \vec{K}^\xi_{mn}$ one has $\mathcal{S} = -\xi\frac{\sqrt{3}}{2}\vec{q}\cdot(\vec{a}' + \vec{a}'') + \frac{i}{2}\vec{q}\cdot(\vec{a}' - \vec{a}'')$, or $\mathcal{S} = \frac{\sqrt{3}}{2}a[-\xi q_x + iq_y]$ in the basis chosen above.

Putting $\frac{1}{\hbar}\frac{\sqrt{3}}{2}a\gamma = v$, one obtains

$$\mathscr{H}_\xi(\vec{q}) = -\hbar v \begin{pmatrix} 0 & \xi q_x - iq_y \\ \xi q_x + iq_y & 0 \end{pmatrix}$$

and

$$E_\mu = \pm\hbar v\,|\vec{q}|\,.$$

Here, if one takes $\gamma = 2.8$ eV, the velocity v equals $0.9 \cdot 10^6$ m/s. One can see that the tight-binding model has now been reduced to a form analogous to the one of the Dirac equation for massless fermions, only that the spinor state here represents association with one of the two sublattices and not the real spin. Low-energy bands — six cones at Brillouin zone corners $E_\mu = \pm\hbar v\,|\vec{q}|$ are thus called Dirac cones, and the quasiparticles obeying the relativistic wave equation the Dirac fermions. The degeneracy of the states at nonequivalent Brillouin zone corners justifies labeling by a two-component isospin quantum number, previously identified as a valley index. The whole low-energy hamiltonian can be further expanded with regard to two possible pseudospin/sublattice components and two possible isospin/valley indexes: (A K, B K, B K′, A K′). This would allow us writing it in a 4×4 space by using the Dirac α and β matrices, thus giving it a genuine form of the Dirac equation $(v\,\alpha \cdot \hat{q} + 0\,\beta v^2)\Psi = E\Psi$. We will not go into those details here, but only refer the reader to some additional literature[12,13,14,15] and references therein.

Electron spectrum in graphene described in terms of Dirac massless fermions is a kind of continuum-medium description that is adequate for electron wavelengths much larger than interatomic distances. However, even at these distances there is still some reminiscence on the existence of two sublattices. In terms of continuum field theory, this can be described only as an internal degree of freedom of the electrons, usually called chirality.[16]

We should note here that the bands of graphene are isotropic only in a small energy range around the Dirac point, which is a name for the position of their apex. The constant energy slices are thus circular just in a narrow area around K, as illustrated in Figure 6. Farther away from the vertex at K the isotropy ceases. The bands become trigonally warped in the directions of the three M points surrounding the K. Even though the M points are not equivalent with respect to translations by reciprocal vectors, equivalency of the band dispersions towards all three of them is obvious. The warping has to do with the slowing down of the bands, all up to the point M where the band velocity comes to naught, resulting in van Hove singularity in the density of states (cf. Figure 5).

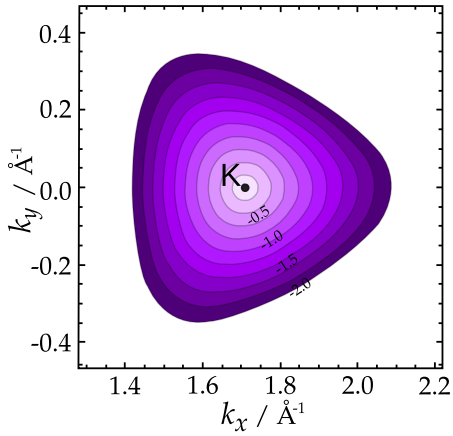

Figure 6: Isoenergy contour map of graphene's π band around the K point. Adjacent contours are displaced in energy by 0.2 eV.

1.3 PROPERTIES

The above mentioned structural and electronic basic properties manifest themselves in a plethora of peculiar effects. We give a survey of the most notable:

AMBIPOLAR CONDUCTION Graphene is genuinely a gapless semiconductor with zero density of states at the Dirac point. Through electrical doping by an external field charge carriers can be switched between electrons and holes, and their concentration tuned continuously from zero to as much as 10^{13} cm^{-2}. Unlike the ordinary condensed matter materials, where there is no symmetry between valence and conduction bands, electrons and holes in graphene are equivalent, quite like the charge-conjugated particles in quantum electrodynamics. The equivalency, as we have seen, comes from the symmetry of the two π bands, having origin in the crystal symmetry and the possibility of describing the quasiparticles in the basis of the two sublattices, i.e. with the pseudospin internal degree of freedom.[16] Experimental evidence comes from the resistivity measurements of a field-effect device, where the gate voltage induces (dis)charging of an isolated graphene layer, charge concentration being proportional to the voltage. The resistivity curve, shown aside, is symmetric with respect to zero voltage and doping, witnessing ambipolar conduction.

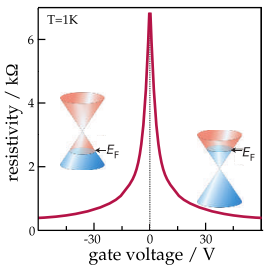

BALLISTIC TRANSPORT Charge mobilities measured in a field effect experiment were as high as 15 000 cm^{2}V^{-1}s^{-1}, and could be easily increased to 200 000 cm^{2}V^{-1}s^{-1} in suspended, impurity-free samples. These high mobilities, observed before mostly in highly electron-doped semiconductor heterostructures, do not noticeably change with temperature rising even to 300 K, and remain

high at high carrier densities in either electrically or chemically doped devices. This all testifies that the transport is ballistic at nearly micrometer scale, i. e. that the scattering events are rare and the motion of charge carriers accelerated over such distances.

MINIMAL CONDUCTIVITY Although the Fermi surface of neutral graphene represent only six points as well as the density of states vanishes where the bands intersect, conductivity of graphene in that case does not disappear but exhibits values close to the conductivity quantum $\frac{e^2}{h}$ per carrier type ($4\frac{e^2}{h}$ in total). No theory has explained the exact value of minimal conductivity in graphene yet.

LANDAU LEVELS The energy spectrum of two-dimensional systems is discretized by virtue of Landau quantization of trajectories when the systems are put in a perpendicular magnetic field B_z. In common systems the spectrum of Landau levels is linear in magnetic field — $E_N = \frac{\hbar e}{mc} B_z \left(N + \frac{1}{2}\right)$, N being an index of Landau level. In the case of massless Dirac fermions the energy spectrum changes as a square root of the magnetic field — $E_{N\sigma} = \pm v_F \sqrt{2\hbar e B_z \left(N + \sigma + \frac{1}{2}\right)}$, $\sigma = \pm\frac{1}{2}$ being a projection of electron's pseudospin. The most peculiar thing in Landau level spectrum is the existence of zero-energy states ($N = 0, \sigma = -\frac{1}{2}$) that are shared by electrons and holes. Landau levels are highly degenerate. Usually they all have the same degeneracy, but in the case of graphene the zero-energy level has half the degeneracy of any other Landau level.

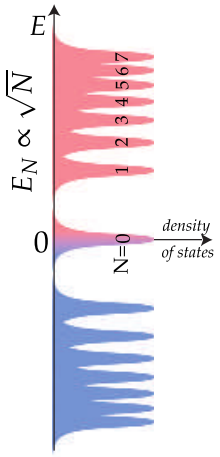

The occupation of the topmost Landau level can be tuned by shifting the Fermi level by varying electron concentration, or by changing the degeneracy of the levels by varying the flux of the magnetic field. The occupation can range from entirely empty to completely full, leading to oscillations in various electronic properties, most famous being oscillations of magnetization (de Haas – van Alphen), resistance magneto-oscillations (Schubnikov – de Haas), and quantum Hall effect.

CHIRAL QUANTUM HALL EFFECT Plateaus in transversal Hall conductivity σ_{xy} are normally at integer multiples of the conductance quantum $\frac{e^2}{h}$. These correspond to filling the first N Landau levels. The existence of half-degenerate zero-energy Landau level leads to an anomalous quantum Hall effect for massless Dirac fermions in graphene. Plateaus emerge at half integers of $4\frac{e^2}{h}$ for both electrons and holes (factor 4 appearing due to double valley and double spin degeneracy); longitudinal resistivity ρ_{xx} vanishes at the same carrier concentrations, indicating when the Landau levels are full. Quantum Hall effect is easily

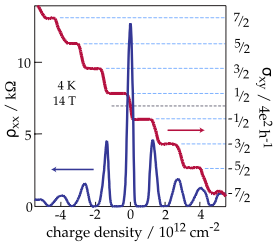

observed even at room temperatures: orbital splitting of Landau levels in graphene being huge (the energy gap between the first two Landau levels in a magnetic field of 20 T is of the order of 2000 K), thermal scattering events between the levels are pretty rare. It is often noted that such an anomalous quantum Hall effect is the most direct evidence for Dirac fermions in graphene.

1.4 WAYS TO PRODUCE GRAPHENE

mechanical exfoliation of graphite

Occurring naturally as weakly-bound layers that form graphite, graphene could have been produced by exfoliation. Yet it was not until the work of the groups of Ruoff[3] and particularly Geim and Novoselov[8,9] that this was achieved. Single, double and multiple layer graphene flakes up to 10 μm in size have been obtained and thoroughly characterized in transport and optical measurements. Placed on an insulating substrate or suspended, samples have been produced with electron mobilities as large as 200 000 $cm^2V^{-1}s^{-1}$.

The method, however, has been soon recognized as one that suffers from a range of limitations: samples that can only be manufactured on a small scale are not quite reproducible, contain an unpredictable number of graphene layers, and the films obtained are exceedingly wrinkled.

epitaxy on insulating substrate (SiC)

Another route to fabricate graphene has been deployed by a group of de Heer.[17,18,19] Large-area growth was achieved on silicon carbide (SiC) wafers through high temperature (1600 K) sublimation of silicon from the crystal surface in vacuum. The decomposition turns out to be a non-self-limiting process, having as a result coexisting areas of various graphene thicknesses. Moreover, graphene growth is accompanied by substantial changes in the morphology of the SiC substrate, leading to considerable roughening. A refined method by Emtsev *et al.*[20] based on atmospheric pressure graphitization of SiC(001) at even higher temperatures (1900 K, 0.9 bar of argon) accomplished a greatly improved surface morphology. Graphene monolayer homogeneously covers large, atomically flat terraces, showing well ordered lattice at an angle of 30° to that of the substrate. The layer is decoupled from the substrate by a non-metalic buffer of carbon atoms of a $(6\sqrt{3}\times6\sqrt{3})$ reconstruction. Nevertheless, the Dirac point is shifted 0.45 eV below the Fermi level, owing to electron doping ($1 \cdot 10^{-13}$ cm^{-2}) from the substrate.[20] Judging only from the 0.165 nm distance of the graphene layer to its support,[21] which is half the distance of weakly bonded graphene layers in graphite, on could conclude that the interaction between the two is rather strong.

All this is true when the silicon-terminated face $(0,0,1)$ of SiC is used. In contrast, when graphene is grown on the carbon-terminated face $(0,0,\bar{1})$ of SiC, it is bound by weak forces directly to the substrate. Multilayer graphenes grown on this face exhibit the linear low-energy dispersion of a single layer, the interaction being minimized by rotational disorder between the layers.[17,22]

epitaxy on transition metal surfaces

The common opinion that graphene can only be exploited on insulating supports does not mean that it should be *produced* as such. There has been a long experimental experience of assembling carbon (mono)layers on transition metal surfaces, that could be tailored now in producing well ordered large scale graphene. The emergence of carbon formations was first observed during preparation of some single crystal surfaces, and was usually considered a nuisance. The case was that carbon, during the usual annealing of the samples at high temperatures, segregated from the bulk to the surface. The present success of graphene has lead to a renewed interest in graphene adsorbed on metal surfaces.

In addition to producing graphene by carbon segregation from the bulk, graphene can be prepared by surface decomposition of carbon compounds, in particular hydrocarbons. The molecules are either directly decomposed on a hot metal surface — in a method called Chemical vapor deposition (CVD) — or first adsorbed on a metal, where they are possibly partially decomposed, then heated to temperatures when nothing but carbon remains — a method called Temperature programmed growth (TPG). Simultaneous growth of multiple layers is hard to avoid when graphene is manufactured by segregation, whereas the processes including external sources of carbon are often self-limiting, as they seem to involve catalytic reaction on the metal surface that is suppressed wherever the surface is already covered.

Graphene growth has been tried on many metal surfaces, most notably cobalt, nickel, copper, ruthenium, rhodium, palladium, iridium, and platinum. In the following, we give an overview of their structural and electronic properties, finishing with Ir(111) that will be the subject of our study.

Carbon overlayers seem to be relatively strongly bound to the substrate at the surfaces of Ni(111), Ru(001), Co(001) and Pd(111).[23] Tunneling microscopy and diffraction studies of their separation from the substrate conclude that the distances that are almost half the distance of graphene layers in graphite should indicate bonding that is well beyond van der Waals. Changes in vibrational spectra, density functional (DFT) calculations of binding energies and significant changes in the structure of the electronic bands corroborate the conclusions. Angle-resolved photoemission (ARPES) data on the electronic structure of graphene on these substrates still show the characteristic σ and π bands, but these are somewhat distorted and shifted to higher

binding energies by about 1–2 eV. The observed gap opening at the crossing point of the π bands signals a covalent electron localization due to the coupling of the p_z orbitals to the valence bands of the substrate.[23] Such behavior was characterized by ARPES for graphene on Ni(111)[24] and Ru(0001)[25].

The other class make the substrates to which graphene is seemingly weakly bound — Pt(111), Cu(111), Ag(111), and Ir(111).[23] Their distance to graphene is generally larger than 0.3 nm, close to the value of 0.35 nm separation of layers in graphite that are bound by van der Waals forces. Electronic bands of these show in essence only rigid shifts, due to non-localized charge redistribution.[26] Interestingly, the same happens with the abovementioned strongly bound graphenes when alkali or noble/coin metal atoms are intercalated.[24] This not only liberates the π electrons, but stiffens the σ bonds to the strengths seen in graphite.

The lattices of all these metal surfaces differ in size from the lattice of graphene. The mismatch is smallest for Ni(111), just about 1%, and leaves no trace in the structure of epitaxial graphene, probably also because the strong bonding. On other surfaces, large coincidence (quasi)periodicities arise as a result of 10–12% larger lattices of the substrates. In addition, owing to extraordinarily strong carbon-carbon bonds that are hard to deform, many of these graphenes buckle, presumably in order to catch energetically favorable adsorption positions. The emerging supercells are of a tenfold size. Height modulations in such buckling appear to be quite appreciable, amounting to around 0.1 nm.[27,28]

Graphenes that are strongly bound to the substrate often grow in a single orientation as there is a strong preference on where to bind on the supporting surface. The others usually exhibit domains of several different orientations. However, it has been shown that graphene on Ir(111) can be grown in a single orientation, where the principal directions of the lattices of graphene and the supporting surface coincide.[29] Moreover, the observations on micrometer-large single domains strongly suggests that structural coherence of the graphene lattice is maintained even across atomic steps.[30] It is important to note that different domains of graphene can be produced on Ir(111) as well, depending on the growth method chosen, annealing temperature, growth speed, etc.[29,31,32,33]

Carbon solubility in iridium is insignificant at the temperatures used for graphene formation, and no carbon segregation from the bulk is ever expected. The growth using hydrocarbon decomposition happens to be a self-limiting process. The CVD procedure thus ensures the completion of just a single layer, given a sufficient supply of hydrocarbons. Nevertheless, the best orientational order of graphene on Ir(111) is achieved when the TPG procedure is used, specifically at the temperatures above 1300 K. To complete a layer, dozens of TPG cycles

are needed, as each cycle leaves graphene on just a 20% of iridium surface that remained uncovered in the previous cycle.[34] If the TPG is used as the initial stage of graphene growth that will fix graphene flakes in the proper orientation and the layer completed with CVD, excellent orientational order of TPG flakes is preserved and the full coverage achieved in a short run.[35]

In this work, graphene samples were produced by iterating the TPG procedure over twelve to fifteen times. In each cycle iridium surface was saturated with ethene (C_2H_4 adsorption for 40 seconds at $2{\cdot}10^{-5}$ Pa, 300 K), the whole crystal then vigorously heated to 1300 K for 20 seconds by back-side electron bombardment, and left to cool down for the next cycle for about 10 minutes. Graphene arising from such a procedure showed an exceptional quality. We continue by giving its structural characterization in the next chapter.

2

GEOMETRY OF GRAPHENE ON IR(111)

Since ARPES is a surface integrating technique and not a local probe, single-domain monolayer graphene is a prerequisite for high resolution measurements. We give here an overview of the structure of such a graphene grown on Ir(111). The geometry of the emerging structures will be discussed — first in real, then in reciprocal space.

2.1 GEOMETRY IN REAL SPACE

2.1.1 *Iridium (111) surface vs. graphene*

A scanning tunneling (STM) micrograph made after the first cycle of ethene decomposition in the TPG procedure, Figure 7a, shows wide terraces of iridium (111) surface decorated with flakes of graphene. Zooming to the border of one of the flakes, Figure 7b, reveals the atomic structure of both iridium and graphene. As iridium is a face-centered cubic (FCC) crystal, its (111) surface exhibits a hexagonal net of atoms. In a close-up picture of the surface, shown on the right, rhombus marks a unit cell of Ir(111). The surface is usually thought of as non-reconstructed, and the parameter of the surface unit cell taken from the bulk value, as $a_{\mathrm{Ir}} = a_{\mathrm{bulk}}/\sqrt{2} = 0.272\,\mathrm{nm}$.

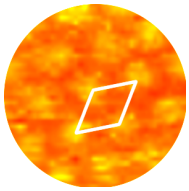

unit cell of Ir(111)

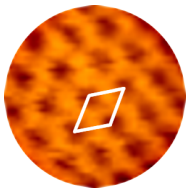

unit cell of graphene

The presence of graphene is witnessed by a honeycomb structure of atoms on the right part of Figure 7b. The repeat distance of the structure, a_{gr}, equals 0.246 nm. Although the individual atoms are not resolved, the unit cell can be marked by the centers of carbon rings, as in the close-up image on the right.

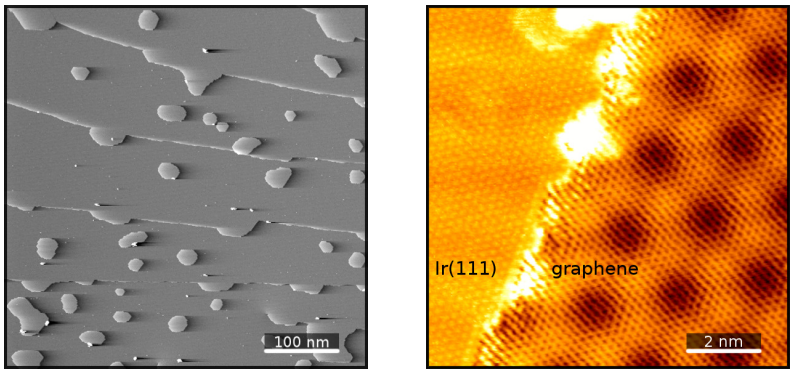

Figure 7: (a) Patches of graphene on terraces of Ir(111) after the first growth cycle. The coverage is around 20% (b) Zoom-in to the border of one of the patches. Surfaces of Ir(111) and graphene are visible in atomic resolution. STM images by N'Diaye[36]

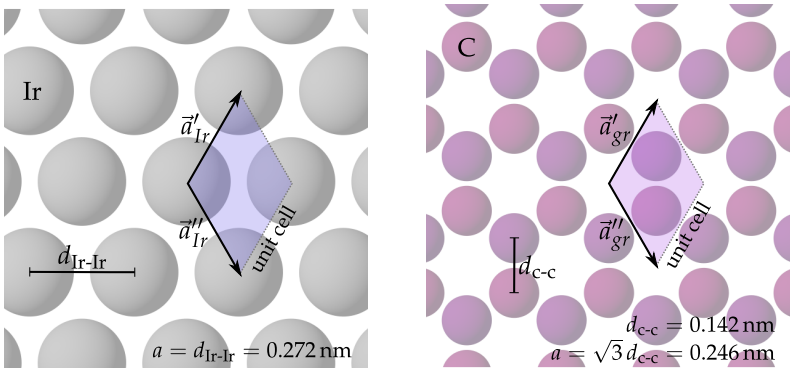

Figure 8: Hexagonal structures of atoms at the (111) surface of iridium (left) and in graphene (right). Marked are unit cells, their repeat vectors, and the relevant dimensions.

The relation of the two structures can be best inferred from illustrations in Figure 8. As both nets are hexagonal and equally oriented, the unit cells have the same appearance, only the dimensions of the unit cell of graphene being by a factor of 0.9 smaller than those of Ir(111).

The contrast on the right of an STM micrograph in Figure 7b changes also over much bigger distances than the size of a unit cell of graphene. This indicates a superstructural ordering on graphene that will be discussed in the next section.

2.1.2 *Moiré of graphene on Ir(111)*

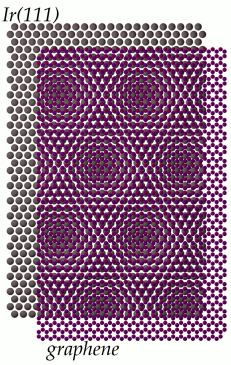

Were the interaction between graphene and iridium surface structureless, i.e. only constant, graphene would be a flat sheet — an ideal graphene. By having a preference on where and how to bind, either the atoms of carbon in graphene or the surface atoms of iridium should adapt by changing their mutual distance. In either case energetically costly reconstruction would result. A different scenario seems to be happening: as graphene is a two-dimensional sheet, it buckles with ease, and forms what is known as a moiré superstructure — a superposition of the atomic structures of the substrate and the overlayer.

As we have seen, the unit cells of both graphene and Ir(111) are hexagonal and differ in size by 10%. A mere geometrical superposition of such a two periodicities, as can be seen on the side, leads to the pattern we encountered in Figure 7b. In this case, iridium stays an ideal termination of the crystal in the (111) plane, while graphene only slightly ripples in order to pin the energetically favorable positions every a while. STM micrographs, shown in Figure 9, exhibit a contrast with a periodicity of $a_m = 2.53\,\text{nm}$, which is about 10 times larger than the periodicity of graphene. The contrast changes as the carbon atoms change their position relative to the underlying iridium

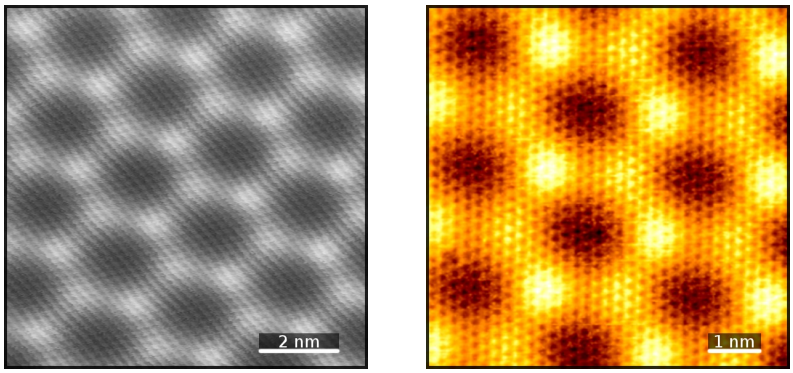

Figure 9: Two STM micrographs showing the moiré superstructure of graphene on Ir(111). The supercell of moiré is about 10 times larger than the unit cell of graphene in each dimension.[36]

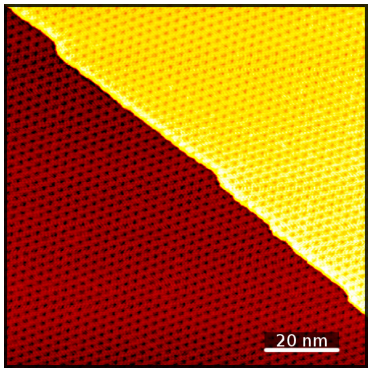

Figure 10: An STM micrograph of the moiré of graphene on Ir(111) at the full coverage.[36] Coherency of the moiré supercells across the substrate steps testifies long-range structural order.[30]

atoms. The contrast, however, also changes with the tunnelling parameters, proving that the reconstruction is not purely geometrical but a redistribution of the electrons is involved as well.

The supercell of the moiré has the same shape and orientation as the unit cells of both graphene and iridium.

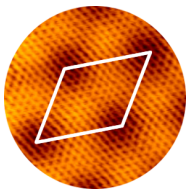

moiré supercell

2.1.3 *Coherence of graphene on Ir(111)*

In the course of ethene decomposition cycles ever-growing graphene patches can be imaged by STM all upon the closure of the layer. Graphene starts growing from patches nucleated at Ir(111) step edges and proceeds to both sides of the edge.[30] At full coverage a regular structure of moiré supercells can be traced over the whole surface. It extends across the steps on the surface of iridium in a regular fashion, retaining the same orientation over the terraces. Samples can be produced where no defects can be observed over micrometre distances.

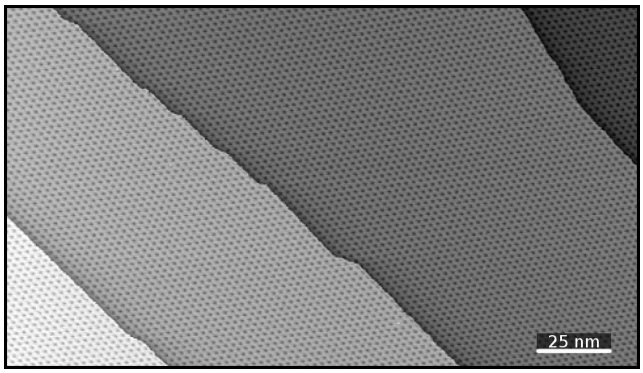

Figure 11: STM image of graphene grown on Ir(111) at 1300 K. A regular pattern of moiré supercells extending over several steps can be seen. Taken from[30].

2.2 GEOMETRY IN RECIPROCAL SPACE

Another insight into the structure of graphene on Ir(111) comes from the diffraction techniques. Low-energy electron diffraction images show, in essence, a reciprocal net of the surface investigated. Diffraction pattern from the clean (111) surface of iridium, Figure 12a, is a hexagonal net corresponding to the hexagonal structure of Ir atoms on the surface in real space. Diffraction image obtained upon the closure of the graphene layer, Figure 12b, contains a set of additional spots. The ones farther away from the center and the spots originating from Ir(111) can be assigned to the diffraction on the periodic array of carbon atoms. This is corroborated by comparing the distance from the center of the diffraction image to the spots marked with Ir and C on Figure 12b. These should relate as the reciprocal values of the unit cell dimensions of the two. And indeed, the spot distance ratio is $d_{\mathrm{Ir}} : d_{\mathrm{C}} = 0.906 \pm 0.003$, while the ratio of the cell dimensions is $a_{\mathrm{Ir}}^{-1} : a_{\mathrm{gr}}^{-1} = 0.904$.

At equal distances from the spots of Ir(111) and graphene, a series of additional spots is observed. These arise from the diffraction on the periodicity of moiré. Specifically, the ratio of their mutual separation to the size of the reciprocal net of Ir(111), which is $d_{Ir} : d_{\mathrm{moiré}} = 9.5 \pm 0.3$, matches the ratio of the unit cell dimensions of Ir(111) and moiré as measured by STM, $a_{\mathrm{Ir}}^{-1} : a_{\mathrm{moiré}}^{-1} = 9.3$.

In this case, diffraction on competing periodicities leads to the diffraction image that is a convolution of separate processes — the diffraction on the net of graphene or Ir(111) unit cells and the diffraction on the net of moiré supercells. Hence, around each C or Ir spot a hexagonal array of first order diffraction maxima from the moiré is present. These further extend to the faint second order maxima, proving also a long-range order of the structures.

Reciprocal nets, readily seen on the low-energy electron diffraction (LEED) images, can also be constructed from the real-space geometry

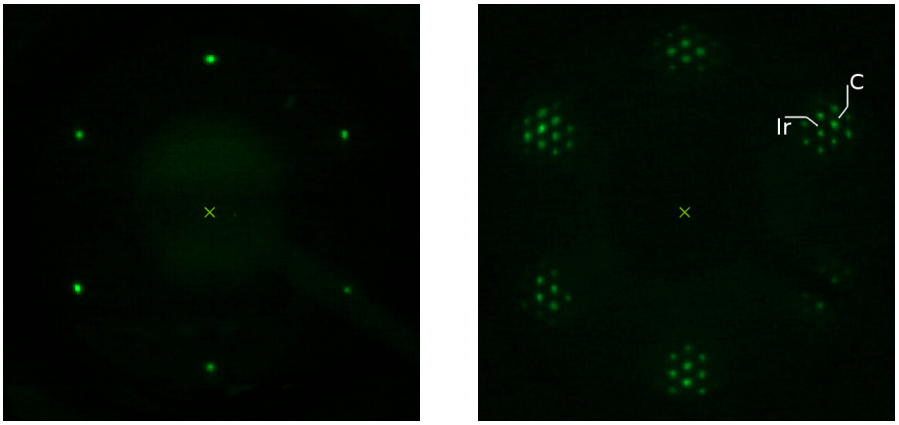

Figure 12: LEED images of (a) a clean Ir(111) surface and (b) graphene epitaxially grown on Ir(111)

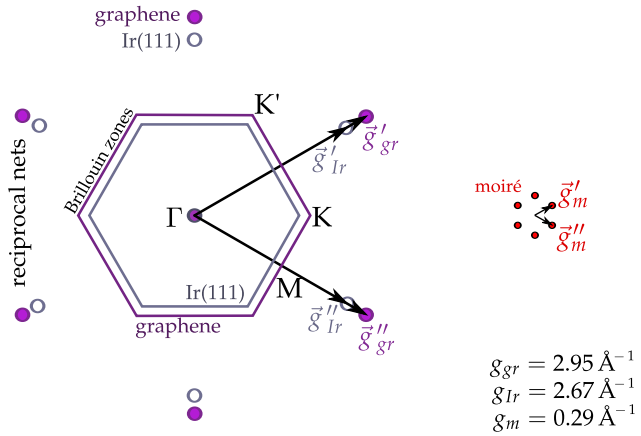

Figure 13: Reciprocal nets of graphene, iridium (111) surface and moiré superstructure of graphene on Ir(111). Drawn are also Brillouin zones of Ir(111) and graphene.

previously depicted in Figure 8. The construction, shown in Figure 13, starts from the reciprocal lattice vectors complemental to the lattice vectors from Figure 8. Their lengths, $g = \frac{2\pi}{a \sin 60°}$, are given as a part of the figure. The whole reciprocal nets of Ir(111) (empty dots) and graphene (filled dots) are then built through the translation of the origin by a number of these vectors. Also shown is a construction of Brillouin zones with some of their high-symmetry points labeled. The K and K′ points of graphene, where the vertices of the Dirac cones are expected, lie at a distance of 1.70 Å^{-1} from the center Γ of the Brillouin zone. Those of Ir(111) are at 1.53 Å^{-1}. The M points are at 1.48 Å^{-1} for graphene, and 1.34 Å^{-1} for Ir(111). The M points can also be reached at the extension of the Γ-K line (in the extended zone scheme); their distances to the Γ point are then 2.55 Å^{-1} in the case of graphene, and 2.30 Å^{-1} for Ir(111).

The moiré superstructure is defined by the reciprocal lattice vectors of the same orientation as those of Ir(111) and graphene, but their length is reduced to $g_{\text{moiré}} = 0.29$ Å^{-1}. This is imaged to scale on the right of Figure 13.

2.3 DEPARTURES FROM THE IDEAL GEOMETRY

Numerous defects appear in graphene epitaxially grown on Ir(111) and their relevance for ARPES has to be taken into account. Topological defects such as carbon vacancies or additional atoms that result in the formation of pentagon or heptagon rings, as well as various cracks and wrinkles that appear during the preparation of graphene can all develop their own localized states, and can also affect the coherency of the intrinsic delocalized states. These defects, however, are relatively rare and their influence on the spectra is believably negligible.[30,32,37]

Nonideal growth conditions, in particular too low temperature during the initial stages of graphene formation, can lead to rotated domains when not only the orientation matching the orientation of the substrate is found but also the minority domains that are rotated by 30°, 19° or 14°.[32] If these domains are of a large enough size their ARPES signals simply add, complicating the analysis of the spectrum. Studies by using nano-beam ARPES that were conducted specially on these domains claim that graphene rotated by 30° is even more weakly bound to Ir(111) than graphene in registry with the substrate.[33]

Yet another departure from the ideal geometry is observed in graphene on Ir(111), that of a slight scatter of graphene orientations with respect to the substrate. This can lead to averaging over a certain area in momentum space and to an augmentation of the spectral band widths. STM studies on the substrate covered with graphene by 20% (after the first growth cycle in TPG) yield a 0.25° scatter of the orienta-

tions of various graphene patches.[34] With greater coverages, however, this scatter is reduced, such that it becomes comparable with the 0.1° angular resolution of an electron analyzer.

Summarizing, most of the departures from the ideal geometry of graphene on Ir(111) should be of minor relevance to ARPES spectra, as graphene with lateral dimensions over a few micrometers can be produced in great structural quality and insignificant orientation scatter.

Part II

ELECTRON SPECTROSCOPY OF GRAPHENE ON IRIDIUM

3

THE SUBSTRATE: IR(111)

It is often desired that bulk substrates supporting the nanostructures built on their surface have as little influence as possible on the electronic states inherent to the nanostructure. Localized electronic states develop at the surface of a crystal or adsorbate heterostructure when the propagation to the bulk of an electron in a certain state is forbidden either by the symmetry of the state that is incompatible with the symmetry of the bulk states, or if there is a complete absence of the bulk states of given energy and momenta. In the latter case there usually exist whole regions in the k_z projection of the bulk band structure where no states can be found. As the projection is simply a collection of states irrespective of the part of their wave vector perpendicular to the surface, k_z, the gaps ensure that the propagation in the plane parallel to the surface cannot be extended into the bulk, for there are no states to extend to.

Insulators and semiconductors have a total energy gap over the whole Brillouin zone, providing a complete barrier for penetration. In metals, electrons within the supported nanostructure may, depending on the direction of propagation, experience potential barriers at the interface, as the electronic states in some points of the phase space (E, k) in the substrate bulk band structure are not allowed. It is therefore of great interest to know the electronic structure at the surface of the supporting material, and to compare it to that of the nanostructure it supports.

There is yet another reason to investigate the electronic structure of the substrate. Photoemission spectra contain information from a few topmost atomic layers of a surface. Taken on a heterostructure, they will therefore represent a superposition of the electronic states of the substrate, altered or not, and the states of the nanostructure.

In the present chapter we will show an experimental and calculational study of the electronic structure of the (111) surface of iridium along the high-symmetry directions of the surface Brillouin zone. Special attention will be given to the existence of gaps in the projected band structure, a feature that we hope will keep graphene's electronic states preserved.

Previous photoemission and spin polarized photoemission experiments on Ir(111) were primarily focused on the bulk electronic structure along the Γ-Λ-L high symmetry direction[38,39,40,41] which projects onto the center of the surface Brillouin zone. Most of the observed features were explained in terms of direct optical transitions from bulk iridium states. Furthermore, a surface state was observed at around

0.4 eV below the Fermi level, and the spin-orbit splitting of the Λ_2 (Λ_3) and Λ_4 bands determined to be 0.89 eV.[38] Good agreement with a relativistic one-step theory of photoemission was found.[41]

3.1 ELECTRONIC STRUCTURE OF IR(111)

3.1.1 *High symmetry direction* (K′) Γ K M

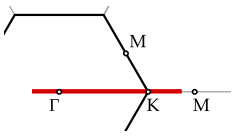

Brillouin zone scan direction

Figure 14 shows two ARPES spectra of Ir(111) along the (K′)-Γ-K-M high symmetry direction obtained with photon excitations from Ne I line (doublet 16.85 eV and 16.67 eV) and He I line (21.22 eV) .

The ARPES spectrum acquired with Ne I excitation shows several bands dispersed around the surface Brillouin zone center Γ. Their binding energies in the zone center have been established from a cut of the spectrum at $k_{||} = 0$, and read $E_A = 0.93\,\text{eV}$, $E_B = 1.35\,\text{eV}$, $E_C = 2.87\,\text{eV}$, $E_D = 3.99\,\text{eV}$. Two bands cross the Fermi level at $k_{||} = 0.78$ Å^{-1} and $k_{||} = 0.86$ Å^{-1}. Close to the K point at the zone boundary two almost flat bands are resolved, one at -1 eV (S_2) and the other at -1.3 eV (S_3).

The spectrum acquired with He I excitation is dominated by a band labeled F. Its dispersion starts from the binding energy of $E_F = 1.04\,\text{eV}$ at the zone center and continues positively towards the Fermi level. At around $k_{||} = 0.5$ Å^{-1} the band bifurcates, the two bands reaching the Fermi level at $k_{||} = 0.68$ Å^{-1} and $k_{||} = 0.72$ Å^{-1}. The band G has a band minimum at the binding energy $E_G = 2.4\,\text{eV}$ and exhibits dispersion only up to $k_{||} = 0.45$ Å^{-1}. What appears to be its extension are two bands reaching the Fermi level at around $k_{||} = 0.85$ Å^{-1}.

Another distinctive feature of the band structure of Ir(111) are two bands labeled E and H that in parallel disperse downwards. The details of the dispersion at their maxima could not be resolved in our study due to low intensity of the spectra and possibly too low resolution when using gas discharge excitation.[42] A study of Varykhalov *et al.*[43] reveals that these two are actually spin-polarized Rashba split bands, being displaced by a wave vector of 0.075 Å^{-1}.

The part of the phase space around the K point is characterized by three states with almost no dispersion. They delimit a wide dark area in the shape of a parallelogram. The state labeled S_1 is characterized by a strong photoemission intensity right at the Fermi level. Two other, labeled S_2 and S_3, disperse in parallel until 1.8 Å^{-1} where S_3 loses on intensity, and S_2 apparently changes to a strong linear dispersion towards the Fermi level, reaching it at $k_{||} = 2.2$ Å^{-1}.

The spectral features displayed in Figure 14 exhibit rather strong dependence on excitation energy, which in turn is a manifestation of the selection rules of optical transitions in photoemission. Mapping the whole structure of the bulk bands of iridium would require an abundance of excitation energies, perhaps even more. In quest of the

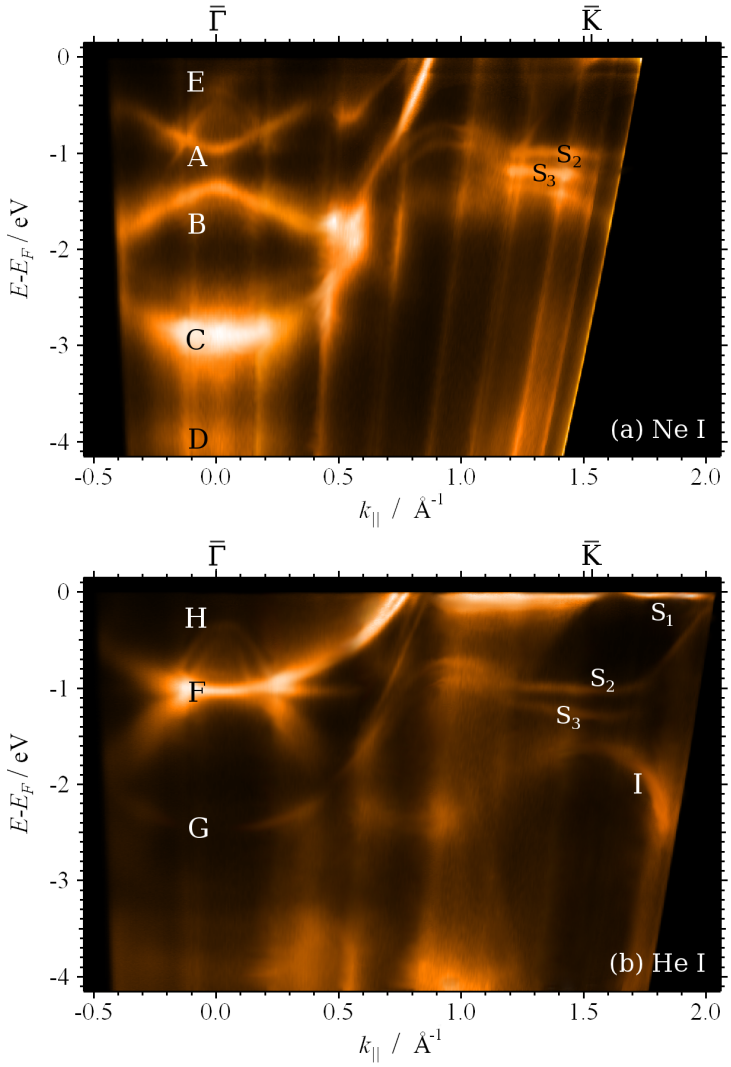

Figure 14: Photoemission intensity maps as a function of electron binding energy and the component of electron momentum parallel to the surface along the (K′)-Γ-K-M high symmetry direction. (a) Ne I photon excitation, 16.85 eV and 16.67 eV (b) He I excitation, 21.22 eV

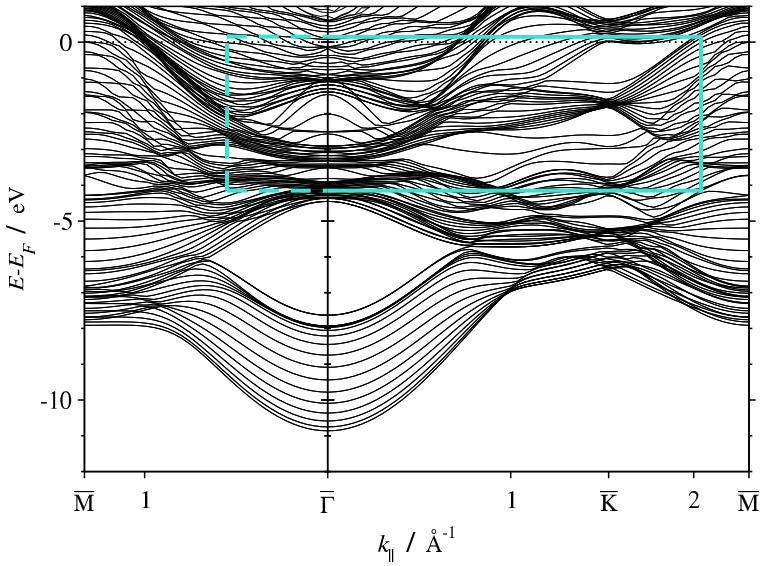

Figure 15: The band structure calculated along high symmetry directions of the surface Brillouin zone. The light rectangular frame denotes an approximate range of experimental intensity maps shown in Figure 14.

gaps in the surface projection of the bulk bands it is thus better to rely on the calculated band structure and use the bands found experimentally only to justify the calculations.

Projection of the bulk band structure of iridium computed using *ab initio* density functional theory with spin-orbit taken into account is depicted in Figure 15.[42] The data shown only along the high symmetry directions of the surface Brillouin zone, Γ-M and Γ-K-M, reveal a number of energy gaps with a few clearly distinguished surface states passing through them. We first analyze the gaps around the center of the surface Brillouin zone. Near the bottom of a large gap extending from -4.5 eV to -8.0 eV a split-off surface state exists which starts at -7.6 eV and runs parallel to the bottom of the gap. A similar state, having most of its weight close to the surface, starts at -2.5 eV; yet this one is not situated within a true energy gap but extends through the low density of bulk bands, probably of incompatible symmetry. At larger momenta $k_{||}$ several other gaps exist, virtually all supporting creation of surface states. A wide gap between -4 eV and -2 eV contains two pairs of surface states that are spin-orbit split. Their identification of being spin-orbit split comes from a density functional calculation that disregarded spin-orbit interaction, giving only two bands, roughly in between each of the two.[42]

The gap most interesting for our study of epitaxial graphene is definitely the one around the K point of Ir(111) at $k_{||} = 1.53$ Å^{-1}, extending all over to the K point of graphene at $k_{||} = 1.70$ Å^{-1} where Dirac cones are expected to emerge. The gap starts right at the Fermi level and reaches down to -1.6 eV. Near the bottom a pair of spin-

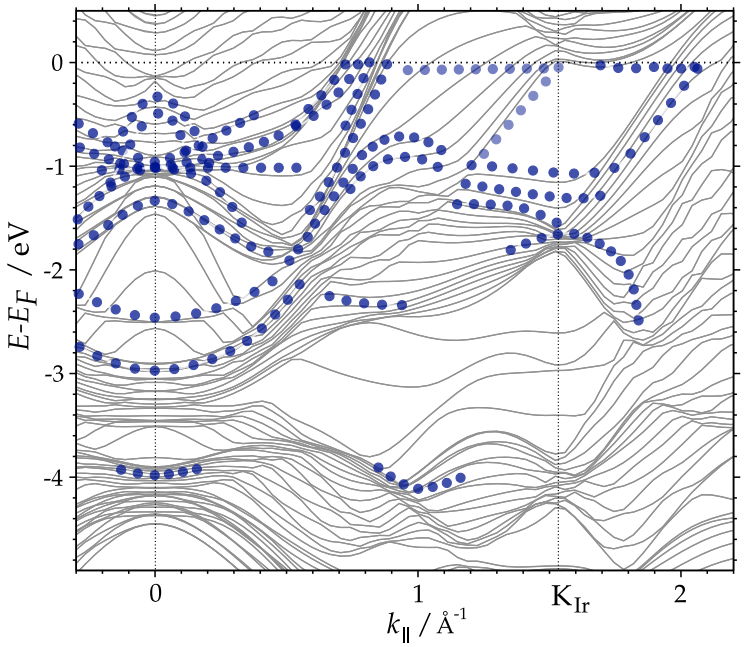

Figure 16: Experimental data extracted from the spectra in Figure 14, here shown as dots, superimposed to the calculated band structure of Ir(111) along high symmetry directions of the surface Brillouin zone.

orbit split and almost dispersionless states is visible. From the upper side, the gap is delimited by another, almost flat surface state that just crossed the Fermi level. Although the calculations cannot differentiate the true surface states and surface resonances that join bulk bands, by comparing the bulk density functional calculations and those of periodic slabs of finite thickness separated by enough empty space (thus simulating surface), one certainly can say which states are localized at the surface and which propagate through the bulk.

The experimental data obtained with both excitations can now be compared to the computed bands. Figure 16 which shows them combined suggests very good agreement.

In the energy range between 1.3 and 3 eV around the center of the surface Brillouin zone, both ARPES maps (Figure 14) indicate the possible existence of an energy band gap, as the corresponding energy range is characterized by very low photoemission intensity. Figure 15 shows that this part of the surface Brillouin zone is not a true band gap as it is occupied by low density bulk bands. Despite this fact, it looks as if this band structure supports the existence of a surface state. Namely, from Figure 16 which summarizes experimental observations with respect to density functional (DFT) calculations, one can see an *s*–*p*-like band which starts off at 2.5 eV at the zone center and runs parallel to the bottom of the gap. Figure 16 shows that this band should be associated with the band G from Figure 14. Additional cal-

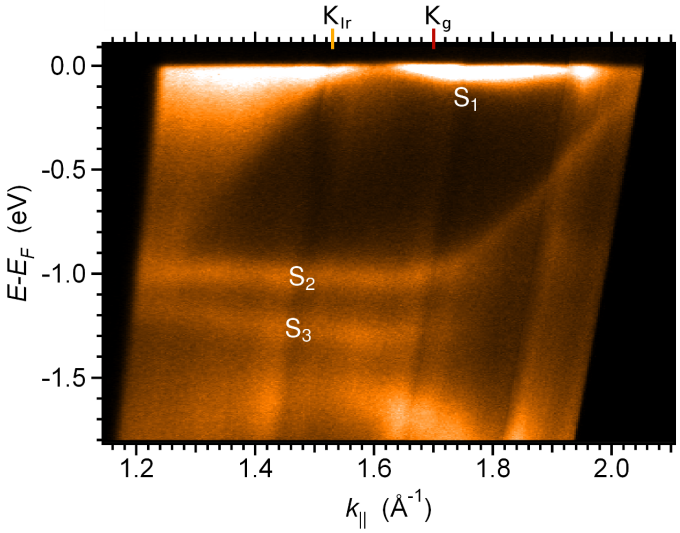

Figure 17: Close-up of an ARPES spectrum of Ir(111) along the Γ-K-M direction in the region of a large gap around the K point. Excitation energy 21.22 eV (He I).

culations have shown that this band is highly localized at the Ir(111) surface,[44] supporting the notion of a surface character of this band. The surface nature of band G also explains our finding that this band disperses up to $k = 0.45$ Å^{-1} , where it merges with the bulk states (cf. Figure 15). Figure 15 also shows good agreement between the energy of band C and the bottom of this energy band gap.

The DFT calculation also shows that a large energy gap extends almost from the zone center beyond the Brillouin zone corner K within the energy range of 1.8 and 4 eV below the Fermi level. From the comparison of the DFT calculation and the shape of band I we can assign the band I as the top edge of this gap. However, as Figure 16 shows, there is an energy shift (0.3 eV) between the experimental spectrum and the calculated position of the band edge. The origin of this discrepancy is yet unknown. DFT calculations in Figure 15 also show that this band gap supports several surface states. While the spectroscopic evidence of this gap is clear — namely, there are no distinct photoemission features in this portion of the Brillouin zone, the same photoemission spectra do not provide any evidence of surface states within the gap. Photoemission spectra in Figure 14 do not show maxima which can be associated with these surface states.

3.1.2 *The gap around K*

We now turn our attention to the band gap in the shape of a parallelogram centered around the K point. From Figures 15 and 16 we see that two bands almost merge at the K point and that band I can be

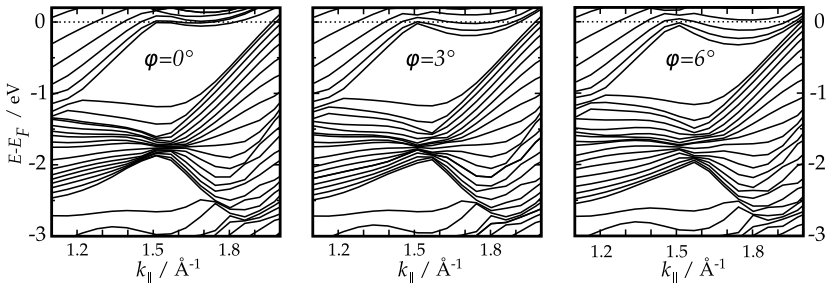

Figure 18: Tomography of the projected DFT band structure of Ir(111) along the rays from the Γ point to the azimuths of 0°, 3° and 6°.[44]

regarded as the bottom of this gap. In fact, along $k = 1.53$ Å^{-1} a large fraction of the surface Brillouin zone is not occupied by bulk electronic states (see the dotted line in Figure 16) and band I is the only bulk band in the wide energy range of 3.8 eV. Based on both the DFT calculation and photoemission spectra we conclude that a large portion of the surface Brillouin zone around the K point is occupied by a true band gap. The DFT calculation (see Figures 15 and 16) suggests that the states having labels S_1, S_2, S_3 in our ARPES maps are surface states. DFT calculation also shows that S_3 and S_2 bands are spin–orbit split surface states with the splitting somewhat smaller than 0.3 eV. A large fraction of the S_1 surface band is above the Fermi level (Figure 17). The other two surface states, S_2 and S_3, are clearly visible in both ARPES maps (Figure 14). Spectrum obtained with 21.22 eV photon excitation, clearly displays the complete band gap with corresponding surface states. From the figure one can note that surface state S_2 is for the most part dispersionless, all up to $k = 1.68$ Å^{-1} where it apparently changes its direction towards the Fermi level. The surface state S_3 also shows very weak dispersion with a strong attenuation of the spectral intensity beyond $k = 1.68$ Å^{-1}.

Additional insight into the the structure at the projected band gap around the K point can be gained from the tomography of the calculated band structure shown in Figure 18 along the rays from the Γ point at the azimuths of 0°, 3° and 6°.[44] Noticeable is the gap narrowing by the bands that cross the Fermi level at higher azimuths, where k_x is ~1.7, and k_y amounts to ~0.15 Å^{-1}. As we will see later, this has little possibility on influencing the bands of graphene because of their fast dispersion (which is approximately -0.5 eV per 0.1 Å^{-1}).

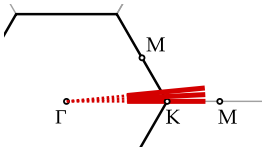

Brillouin zone scan directions 0°, 3°, 6°

4

ELECTRONIC STRUCTURE OF GRAPHENE

After a few growth cycles in by a TPG procedure, a salient footprint of graphene starts to appear in photoemission spectra: two linear bands enlighten the band gap of Ir(111), dispersing sharply to and from the Fermi level, meeting at the anticipated position of the Dirac point at $k_{||} = 1.70$ Å^{-1}.

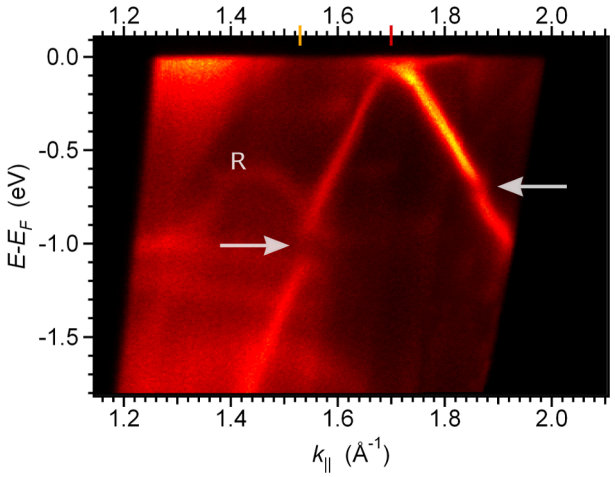

Figure 19: ARPES spectrum of graphene grown on Ir(111) in twelve TPG cycles. Visible is the cut of a Dirac cone along the Γ-K-M direction (±0.5°), a replica band R and two minigaps, marked with arrows. Excitation energy 21.22 eV (non-polarized He I line), temperature 60K.

Such a spectrum, recorded along the Γ-K-M line of the Brillouin zone, shown here in Figure 19, demonstrates all the essential spectroscopic features of graphene grown on the (111) surface of iridium: (1) presence of a Dirac cone, (2) marginal doping, (3) additional bands, (4) opening of minigaps. In what follows we will analyze these features in detail.

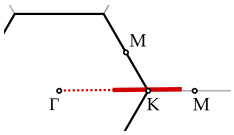

scan direction
Γ-K-M (±0.5°)

4.1 THE DIRAC CONE

The brightest bands in the spectrum shown in Figure 19 are easily recognized as a cut of the π band of graphene through, or close to the vertex of the Dirac cone. Complex ultrahigh-vacuum experimental setup allows only rough alternations of the azimuth of the sample, and its verification by LEED does not yield absolute value, but only relative changes can be recorded, but with an accuracy that is

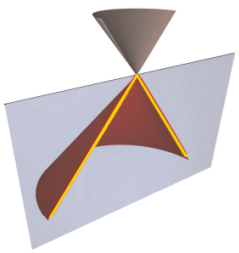

not better than ~2°. High precision full-Brillouin zone mapping with ARPES would be the best way to assess the principal points and high-symmetry directions of the spectrum, but such experimental setups are still very rare and hardly affordable. We will see below how fitting to the TBA bands provided us with the means of determining the azimuthal angle with a precision of just 0.1°.

The bands in Figure 19 are notably linear in the low-energy region, from the Fermi level down to -0.6 eV. Their sharp crossing at the Fermi level readily implies that graphene interacts only weakly with Ir(111). Namely, in strongly bound systems like graphene/Ni(111)[24] and graphene/Ru(001)[25], the apex is usually rounded off due to the opening of an appreciable band gap between the π and π^* bands that hybridize with the substrates. Density functional (DFT) calculations also suggest weak bonding of graphene to Ir(111) substrate,[45,46] visible through the large average graphene to Ir(111) separation of 0.34 nm, which also explains the defect free growth of graphene flakes over the substrate step edges.[30] Based on our measurements on Ir(111) this can be ascribed to the dearth of metallic states of appropriate symmetry, in particular to the existence of the band gap around the K point of the surface Brillouin zone of Ir(111).[42] Two studies, however, give a possibility of graphene's π bands hybridization with the bands of iridium. Starodub *et al*.[33] tune the spectral intensity of the two bands in the vicinity of the Fermi level by changing the excitation energy. The intensity varies for iridium bands but not for the π band, hence they suggest that the states in the apex of the Dirac cone are hybridized as they follow the behavior of the states of iridium. We restrain from accepting such an argument as it is unclear how Starodub *et al*. resolve the individual contributions of the bands in the apex region when both are visible, i. e. it is unknown whether the apex contribution is lower compared to the rest of the π band, iridium band being visible or not. A study by Sánchez-Barriga *et al*.[47] advocates hybridization with a band of iridium at around -3 eV that is seen in the form of an avoided crossing of the bands. Noting that the mere existence of iridium bands crossing the π band does not ensure hybridization, we find their second-derivative spectrum (with possible artifacts) unconvincing, and stay with our interpretation of the origin the gap that will be given below.

Band velocities of the two branches of the Dirac cone are evidently unequal. The velocity in the K-Γ is $0.95 \cdot 10^6$ m/s, whereas in the K-M branch it amounts to $0.73 \cdot 10^6$ m/s. This is simply a manifestation of the known anisotropy of the dispersions, so-called trigonal warping (cf. Figure 6, for example).

Two branches of the Dirac cone cut along the Γ-K-M direction have noticeably anisotropic ARPES intensity. The effect was earlier observed on graphite[48,49] and explained by a structure factor coming from the unit cell consisting of two atoms, i. e. from the interference of electron

waves emerging from the two sublattices. These tight-binding based calculations were further simplified in ref. 50 and directly applied to Dirac fermions in the low-energy model of graphene. A notion has been made of a possibility of testing the A-B sublattice symmetry through the emergence of photoelectron intensity in what is known as the dark corridor in constant energy maps (illustrated aside in two constant energy maps of graphene on Ir(111)). Namely, when the two sublattices are equivalent, it should be observed that one side of the constant energy contour is strictly absent. Breaking that symmetry would then destroy the phase cancellation and the dark corridor would be enlightened.[51] In that sense, according to Figure 19, the symmetry of A and B sublattices of graphene on Ir(111) would be appreciably violated.

the dark corridor

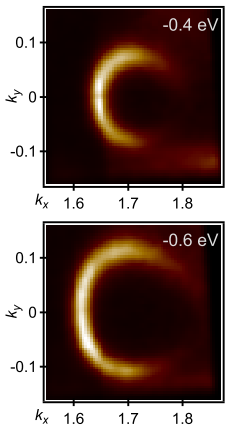

Unfortunately, the models mentioned above do not take into account a possible influence of the polarization of excitation light in ARPES. The model of Shirley *et al.*[49], for example, predicts no intensity at all when the polarization vector is perpendicular to the momentum of photoelectrons (i. e. in *s* polarization). We have conducted a detailed study for graphene on Ir(111), the results being shown in Figure 20. When using the *s* polarization both branches are visible and are almost even in intensity. The completely dark corridor appears in neighboring Brillouin zones (in the direction of K-M, $k_x > 1.7$ Å^{-1}) only when the *p* polarization is used. Accordingly, graphene on Ir(111) can be considered weakly perturbed by the substrate, for certain asymmetry of the lattices could be expected solely from the running positions of graphene atoms with respect to those of iridium were their interaction any stronger.

The spectrum in Figure 19 has to been considered as a superposition of spectra obtained by a certain mixture of polarizations, in a certain experimental geometry and with a certain excitation energy that gives more intensity to the K-M than to the K-Γ branch.

A study by Gierz *et al.*[52] shows that the descriptions of the photoemission process in graphene by both Shirley *et al.*[49] and Mucha-Kruczynski *et al.*[50] are inadequate and that a linear superposition of a whole range of plane-wave final states should be used to account for the effects seen with *s* polarized light. This equals to saying that the final state is not a pure free electron plane wave, but one that can be decomposed to a number of plane waves by Fourier analysis. These considerations have been further extended by Liu *et al.*[53] and Hwang *et al.*[54] in studies with circularly polarized light, bringing in the means of direct measurements of quantum Berry phases.

ARPES maps are analyzed through energy distribution curve (EDC) cuts at selected momentum, or momentum distribution curve (MDC) cuts at selected energy. Both of these have been extracted from a high-resolution spectrum shown in Figure 21 that was recorded with monochromatized 55 eV synchrotron radiation in the *p* polarization

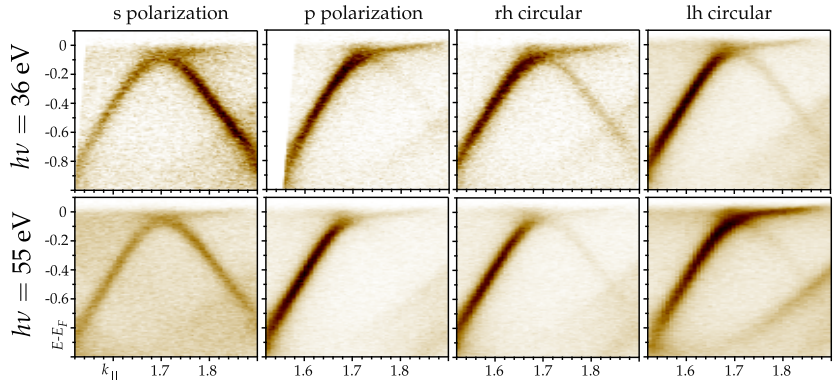

Figure 20: Dependence of the visibility of the two branches of the π band on polarization (s and p polarization, right and left handed circular polarization) of the excitation radiation and its energy (here 36 eV and 55 eV). The dependence for iridium (surface) bands is just as notable.

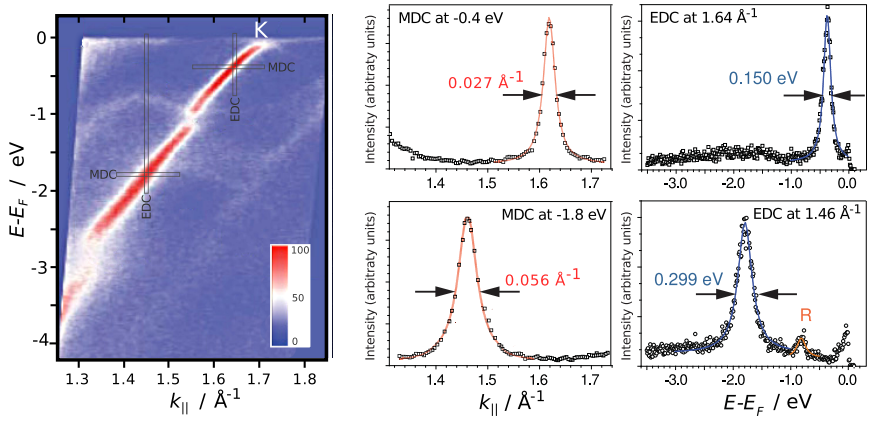

Figure 21: (left) Photoelectron intensity map of graphene on Ir(111) acquired along the Γ-K-M direction (±0.4°), at T=80 K. Due to the p polarization of synchrotron light, only the K-Γpart of the π band is visible. (right) Momentum and energy distribution curves taken at two parts of the K-Γ branch of the π band, as marked on the spectrum left. Full widths at half maximum of fitting Lorentzians are denoted for each curve.

of the field. The peaks were fitted with single Lorentzians, yielding exceptionally low full width at half maximum (FWHM) values, as a signature of a high photohole lifetime — hence high quality graphene, low in defects that could act as scattering centers. It should be noted that the value 0.027 $Å^{-1}$ for the FWHM of an MDC at -0.4 eV is almost equal to that obtained for multilayers of effectively isolated graphene on the carbon face of SiC.[55]

4.2 SLIGHT P-DOPING

Linear extensions of the two bands taken in the low-energy region in Figure 19 cross slightly above the Fermi level. TBA fit to the whole π band that we will deal with below, estimates the position of the Dirac point (0.10 ± 0.02) eV above the Fermi energy, implying a marginal hole doping of the bands. Such a small extent of the p doping comes out as a consequence of a favorable match of several system parameters: proper graphene – Ir(111) distance, work function difference, and weak chemical bonding.[56]

As the Dirac point is not accessible with ARPES, we are unable to judge whether a band gap opens at the Dirac point or not. However, if there is one, it is certainly smaller than twice the distance from the Fermi energy to the estimated Dirac point, i. e. its width must be less than 0.20 eV.

In a later study, Rusponi *et al.*[57] argue that the rounded summit of a cut of the cone is a clear signature of a gap at the Dirac point, and give it a size of at most 140 meV. The fact is, however, that reaching the vertex of the Dirac cone by ARPES is a demanding task in which one can never be sure if some averaging is taking place through a finite instrument resolution, or if there is even the slightest error in positioning the sample. Furthermore, Rusponi *et al.* use rather high excitation energy (120 eV), and collect the photoelectrons in a limited number of slices over a large acceptance angle of 30°; both of these spoil the angular resolution considerably, leading to averaging over a finite region in momentum space. We thus find no proof of a gap in the rounded apex, still allowing for its existence.

4.3 REPLICA BANDS

Besides the primary Dirac cone, Figure 19 displays an additional band, a faint replica band labeled R. As the cause of the band replication we recognize the reconstruction of graphene on Ir(111) in the form of a moiré superstructural ordering. Generally, a regular geometric (re)arrangement of atoms brings with it a new (component of the) crystal potential felt by the electrons, periodicity of the potential being the same as that of the atomic structure. Electrons diffracted at the periodic potential show up in new bands, that are displaced

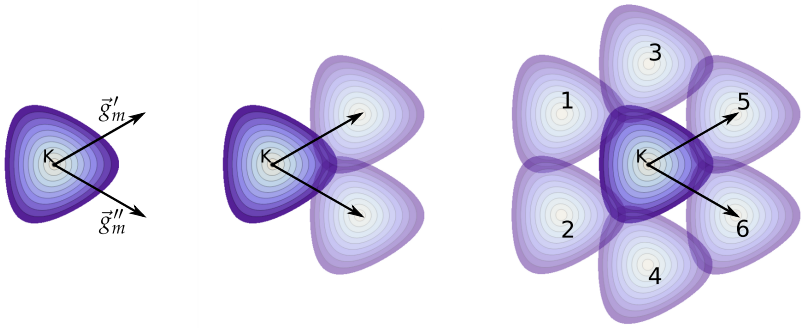

Figure 22: Electrons in the Dirac cone undergo a diffraction and their momentum is changed by the reciprocal lattice vectors of the moiré, $\vec{g}_m$. The result is cloning of the original to six so-called replica bands. They are enumerated on the right for further reference.

in momentum space from the original band by the reciprocal lattice vectors of the new atomic arrangement. This equals to saying that electrons, as a consequence of the diffraction, gain or lose momentum in the amounts of Fourier components of the new potential.

That the electronic potential in graphene is modulated by the substrate is evident from the dependency of the moiré contrast on tunnelling parameters as well.[34] This superperiodic potential replicates the Dirac cones through the reciprocal lattice vectors $\vec{g}_m$ of a moiré (see Figure 13). Schematically, every Dirac cone at K (K′) becomes surrounded by six first-order replicas, their apexes being at the points labeled 1–6 in Figure 22.

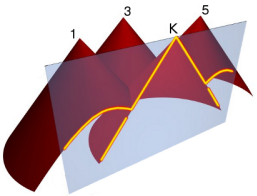

Figure 23 displays the spectrum already shown above, now focusing to additional features. Namely, an ARPES scan along the direction Γ-K-M (k_x axis of the momentum space) contains not only a signature of the Dirac cone, but traces of all of its replicas are visible. Their naming can be followed in Figure 22:

1&2 Coming from the left, where the center Γ of the Brillouin zone is, a hyperbolic cut of the replicas 1 and 2 emerges, having a maximum on energy -0.63 eV at $k_{||} = 1.46$ Å^{-1}, or 0.24 Å^{-1} away from the K point. This band intersects the main cone at $k_{||} = 1.55$ Å^{-1}; -0.89 eV.

3&4 A faint signal from the replicas 3 and 4 occurs without a clear clue for the position of a maximum. As the ARPES scan direction is now more distant from the apex positions of the replica cones the cut appears lower in energy – at about -1.5 eV

5&6 Finally, a fast dispersing tail of replica cones 5 and 6 shows up, reaching the main cone at about $k_{||} = 1.86$ Å^{-1}; -0.66 eV.

The ARPES intensity of the replica bands is an order of magnitude weaker than the intensity of the main cone. This can be seen from the

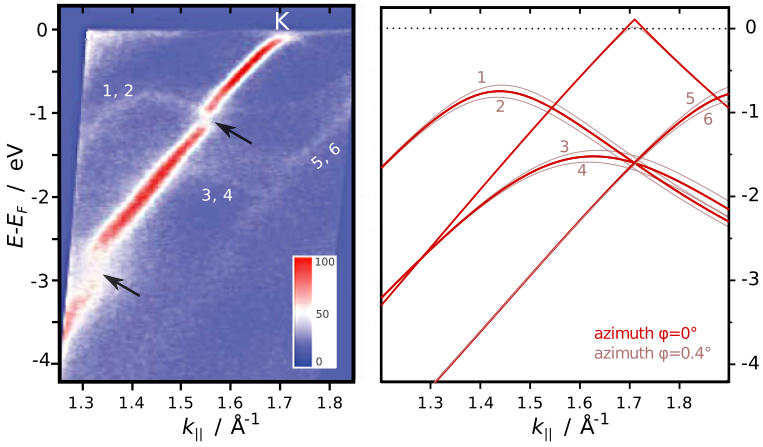

Figure 23: (left) Photoelectron intensity map of graphene on Ir(111) acquired along the Γ-K-M direction, at T=80 K. In addition to the main band, faint contributions of some of the six replicas is visible. Arrows mark the gaps in the Dirac cone that open at the crossings of the replicas with the main band. (right) Simulation of the bands shown on the left using tight-binding formula. Best matching to the experimental bands has been achieved using the scan azimuth $\varphi = (0.4 \pm 0.1)°$, the tight-binding parameters from the density functional calculation by Reich *et al.*[58] and an upward rigid shift of the bands by (0.10 ± 0.02) eV.

EDC in Figure 21. Taken at $k_{||} = 1.46$ Å^{-1} it represents a cut through the main and replica cone (R).

Figure 23 contains a simulation of the experimentally observed bands as well. It has been created by using the tight-binding formula from equation 1.2 with parameters fitting the density functional band calculation by Reich *et al.*[58]: $\gamma = -2.84$, $\alpha = 0.070$. Each replica has been translated around the primary cone by the corresponding reciprocal lattice vector of the moiré, like in Figure 22. Then a cut through the two-dimensional map of band energies in momentum space has been made along the direction (azimuth $\varphi = 0.4°$) that matched the main cone and the replicas the best. This is how the value of marginal p doping, or a rigid shift of the band by (0.10 ± 0.02) eV was obtained as well. Notable is a great sensitivity of the bands to the changes of the azimuth, coming from their fast dispersion. Figure 24 shows the case of azimuth -1.4° where, due to excitation energy used, both replicas 1 and 2 are clearly visible. A cut at momentum 1.42 Å^{-1} has been superimposed to the two-dimensional spectrum, witnessing two peaks at -0.6 eV and -0.8 eV.

At the locations where the replica bands intersect the main Dirac cone a band gap is visible. This has been indicated by arrows in Figures 19 and 23. In the following, the gap in the Dirac cone will be referred to as minigap. The very creation of minigap is an example found in any textbook on condensed matter physics: just as with

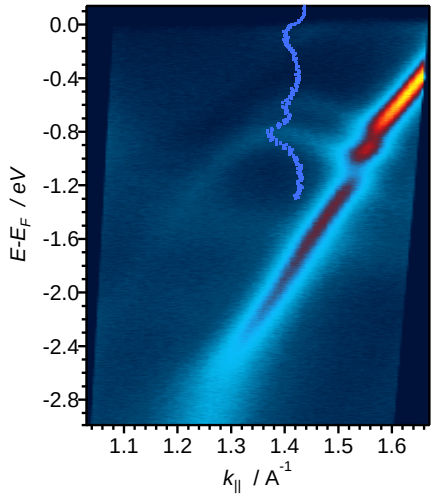

Figure 24: ARPES spectrum using 44.3 eV p polarized excitation of graphene on Ir(111) at the azimuth -1.4° off the Γ-K direction. Two replica bands are highlighted by a cut appended to the spectrum, showing the intensity dependence along the line $k_{||} = 1.42$ Å^{-1}.

nearly free electrons in a periodic potential, a gap opens at the intersection of two hybridizing bands to lift of their degeneracy.

Replica cones in epitaxial graphene could also arise as an effect in the final state of photoemission through an umklapp by $\vec{g}_{Ir}$ at the (111) surface of iridium. This mechanism, proposed for replicas in graphene on SiC(001),[51] is not easy to reconcile with the clear presence of the superperiodic contrast in STM[59,60] and *ab initio* calculations[60] for that system. Though we cannot exclude its contribution to the intensity of the replica cones, the surface umklapp alone cannot create the minigap reported here. Therefore, we consider the presence of the minigap as an evidence for the initial state effect, in other words, as a proof for the existence of a moiré superperiodic potential.

We will see in the next chapter that replica cones and minigaps are lost in the system when alkali atoms are intercalated, leading to a disappearance of the moiré superstructure. That gives a clue that the origin of the replicas is genuinely connected with the moiré, excluding the mechanism of backscattering on the substrate once more.

The question which remains is why the effects of periodically modulated graphene were not found for graphene on SiC(001), a system where graphene is even more strongly superperiodically corrugated than on Ir(111).[60] SiC(001) has been the substrate of choice for ARPES studies of graphene electronic properties so far. It is likely that some controversies (whether or not a band gap opens at the Dirac point)[61] or still poorly understood features (why does the superperiodic structure not open an energy gap)[59,60 51,62] are linked to the complexity of graphene on SiC(001) and its limited structural quality, with the typical domain size in the submicrometer range.

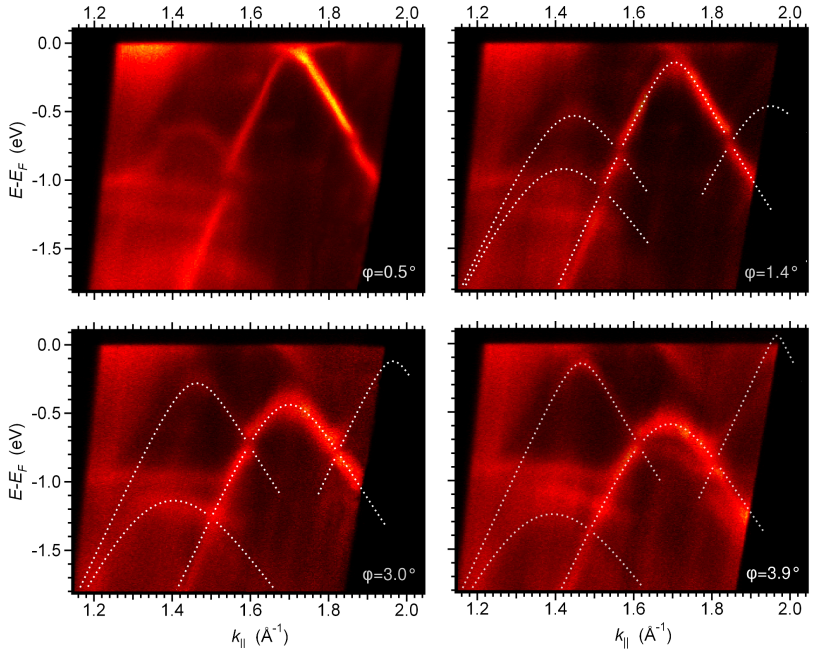

Figure 25: Spectra of graphene on Ir(111) obtained after azimuthal rotations off the Γ-K-M direction. The dashed lines are TBA electronic bands. They simulate the expected contributions of the main Dirac cone and its replicas #1, 2, and 5 from Fig. 22, of which only replica 1 is clearly visible here, and the others only through the effect they leave on the main cone. The best fit to the experimental bands is accomplished by shifting the position of the TBA Dirac point by (0.10 ± 0.02) eV. The TBA fits enable us determine the absolute azimuths of the scan directions, their values being given in each of the panels.

4.4 TOMOGRAPHY OF THE MINIGAP

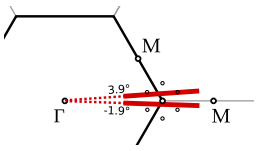

As we turn the scan direction off the Γ-K-M, we move away from the vertex of the primary Dirac cone. Its ARPES cut gets lower in energy, while the opposite happens for the replicas whose vertex is approached, as exemplified in Figure 25 for three additional azimuths φ. The absolute values of the azimuths have been extracted from a series of simultaneous TBA fits to all the spectra shown, comparing them to the relative changes of the azimuths recorded by LEED. Hence, although the fast dispersion of graphene's bands is responsible for sizable changes in the ARPES spectra with changing azimuth, it also enabled us determine the azimuth in the case of a moiré of graphene on Ir(111) with a precision of only 0.1°.

The analysis of the minigaps on these spectra reveals, as shown in Figure 26, that most of them are located on the edge of a hexagonal area centered at the K point of the Brillouin zone of graphene. Its sides are perpendicular to the lines joining the K point and the positions of the vertices of the replica cones, cutting them to half — thus

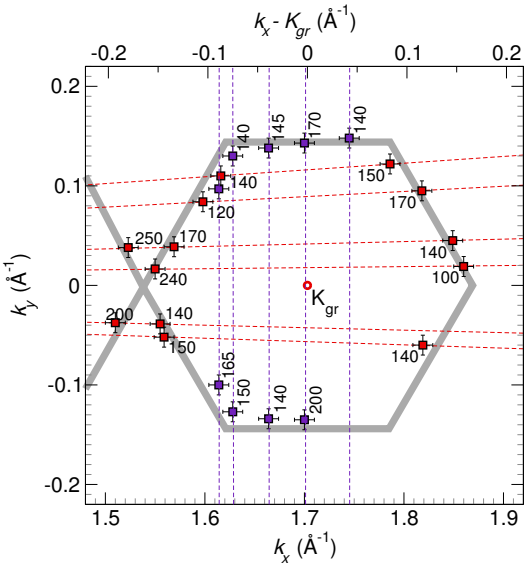

Figure 26: The minigaps determined from ARPES scans along the directions indicated by dashed lines fall at the edge of a regular shape surrounding the K point of graphene. Their widths are annotated in meV. The red dashed lines originating from the center of the Brillouin zone Γ correspond to the azimuths of $-1.9°$, $-1.4°$, $0.5°$, $1.4°$, $3.0°$, and $3.9°$. They were taken at the setups at Zagreb (p. 63) and Elettra (p. 66). The values on vertical scans, having constant k_x value, were extracted from a full 2D mapping of the reciprocal space around the K point, at the BNL/NSLS setup (p. 67).

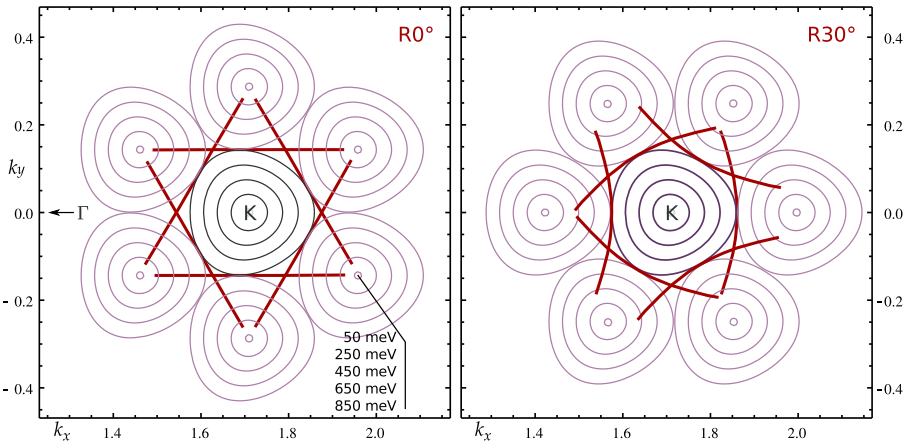

Figure 27: Construction of lines in reciprocal space where the main and six replica bands avoid hybridization by opening a gap. The bands are displayed as isoenergy curves. Depending on the symmetry relation of the lattices of graphene and its superstructure, the shapes change. Here only two cases are considered, those of the matching orientations and those rotated by 30°. Note that the superperiodicity needs not to be hexagonal, different configurations of the replica bands are possible as well.

resembling the construction of a Wigner-Seitz cell around the origin of reciprocal space. However, the origin of the minigap is avoided hybridization of the main and replica cones where they would normally intersect, and is not a purely geometrical construction. Hexagonal zone comes out as a fortuitous consequence of the matching symmetry of the graphene's bands and the moiré. Were the orientation of the moiré turned by 30° with respect to the present, like is the case with in graphene on SiC, our simulation presented in Figure 27 shows that the zone would be distorted. It is our belief that the zone was misleadingly named mini Brillouin zone before,[63,64] and that the full symmetry of the bands and the superstructure has to be considered in saying where the bands cross or where the minigap appears.

The measured minigap widths, annotated in Figure 26 alongside minigap positions, are in the range 0.1–0.2 eV. These values provide an estimate on the strength of the moiré component of the crystal potential. Note however that the minigap size also seems to depend on the angle of the assumed band intersection, and that the fact that it widens in certain regions can be a consequence of a few replica bands crossing in close vicinity. Both Starodub *et al.*[33] and Sánchez-Barriga *et al.*[47] made a full mapping of the bands and extracted the minigap width. While the results of Starodub *et al.* agree well with our measurements, giving a variation of the minigap in the range 100–230 meV, Sánchez-Barriga *et al.* report on an almost constant width, although their data suggest a variation from 150 to 230 meV.

In a calculation of periodic potentials applied to graphene an anisotropic band gap was found, which even vanishes at specific points at

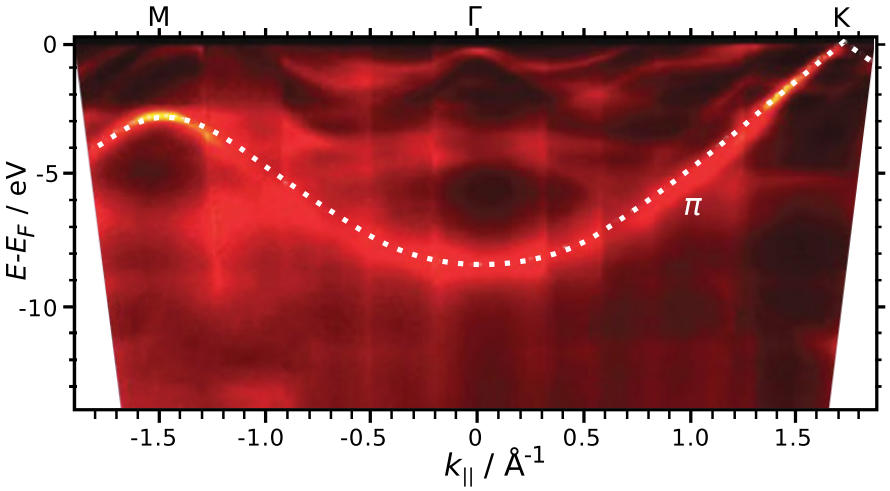

Figure 28: The full π band of graphene on Ir(111) along the high-symmetry directions Γ-M and Γ-K taken with excitation energy of 55 eV. The band has been fitted with a tight binding dispersion function from equation 1.2.

the border of the *mini Brillouin zone*.[63] We have not observed any closing of the moiré gap. Note that the model of Park *et al.*[63] assumes full equivalence of the two sublattices of graphene. However, for graphene supported by Ir(111) a global and local symmetry breaking is possible. In addition, their calculation does not take into account the trigonal warping of the bands, which could have an effect on the minigap widths and positions.

4.5 FULL π BAND

Wide energy scans throughout the Brillouin zone provide us with a map of the overall dispersion of the bands of graphene on Ir(111). Figure 28 shows such a scan along the Γ-K and Γ-M directions of the graphene's Brillouin zone. The dominant feature in the spectrum is the π band. The bottom of the measured band at Γ is on $E_\Gamma = -8.73$ eV and its saddle point at M on $E_M = -2.74$ eV. Another feature of the electronic structure of graphene are the σ bands, which originate from the in-plane hybridized electron orbitals. For a wide range of photon energies the photoemission cross section for these bands is much smaller than for the π band. For a photon energy of 55 eV (Figure 28), the dispersion of the sigma band is barely visible. However, for some photon energies its intensity can be notable.[65]

The measured energies of the π band at Γ and M cannot be captured using the TBA parameters derived from a fit of density functional bands for freestanding graphene by Reich *et al.*[58] Although their nearest-neighbor hopping energy $\gamma = -2.84$ eV and overlap $\alpha = 0.07$ accurately describe the measured π band dispersion for graphene on Ir(111) in the vicinity of the K point, the overall band

width is underestimated due to some known issues with DFT.[44] These parameters set the bottom of the π band E_Γ to -6.96 eV, and the saddle E_M to -2.56 eV. Two other published sets of nearest neighbor parameters describing the measured π band of graphene on SiC ($\gamma = -3.28$ eV, $\alpha = 0.0425$) and second layer graphene on Ru ($\gamma = -3.28$ eV, $\alpha = 0.03$) fail to reproduce the observed dispersion of graphene on Ir(111), the disagreement at the two extremes being larger than 0.15 eV.

In order to better describe the whole band dispersion within the nearest neighbor tight-binding approximation, we varied the parameters to best reproduce the measured features. The outcome is displayed as the dashed line in Figure 28. The obtained parameters $\alpha = 0.0029$, $\beta = 0.1$ eV, and $\gamma = -2.848$ eV prove, as much as such a simple calculation can prove, that

A. the overlap between the neighboring p_z orbitals is indeed negligible

B. the intrinsic doping is +0.1 eV, as found before

C. the hopping energy is quite close to the value usually used for the freestanding graphene.

5

ELECTRON DOPING OF GRAPHENE

In this chapter we will study photoemission spectra of highly doped graphene, where a striking effect on the bands just below the Fermi level happens due to the coupling of electrons to phonons. Signatures of two separate processes will be observed that have an origin in the same: phonon spectrum and available phase space for electron-phonon interactions. One signature will be a phonon induced renormalization of electronic bands, having an effect of lowering the binding energy of electrons in a narrow region below the Fermi level. The other will come as a consequence of a hole creation in photoemission process, the effect being a complete lack of photohole relaxation through the phonon channel, in the very same region. The first, coming from an unperturbed system, will be seen as a kink in the measured bands at an energy of the most energetic phonon present in the system. The other, that emerges from relaxation processes in the perturbed system, as a steplike increase of the spectral width, signifying much shorter scattering times for holes below the threshold energy.

Adsorption and/or intercalation of alkali atoms in epitaxial graphenes can lead to a whole range of n dopings, including an extreme case where graphene's van Hove point is brought to the Fermi level.[66] Doped graphene proves to be an interesting platform to study different aspects of many-body interactions in two-dimensional systems, either experimentally[67,68,69] or theoretically[70,71,72]. A particular accent is put on the electron-phonon coupling in doped graphene.[73,74,75]

Studies on KC_8[73] and CaC_6[74] report strong anisotropy in electron-phonon coupling, with significantly smaller coupling constant λ along the K-Γ, compared to the K-M direction. Despite the fact that these experiments were performed by intercalation of graphite, it had been demonstrated that the intercalation separates single layers of graphite in such a way that it shows all signatures of graphene. Some others have reported smaller value of λ,[76,77,78] and no anisotropy in electron-phonon coupling.[76] Recent results also suggest that electron-phonon coupling progressively increases with doping.[79]

Determination of the renormalization effects in n-doped π^* band due to the electron-phonon coupling is complicated, in particular along the K-M direction, because of a non-linear behavior of the band close to the Fermi level.[80] A simple procedure to establish the strength of electron-phonon coupling by a comparison of the quasiparticle velocity at the Fermi level and the velocity well beyond the

phonon energy scale is shown to be compromised by a significant change of the quasiparticle velocity due to the nonlinearity of the π^* band.[80] Some other procedures rely on the bare-band dispersion.[81] The choice of the bare-band may, however, influence an accurate determination of the magnitude and shape of the self-energy.[82] A self-consistent GW approximation was applied in *ab-initio* density functional (DFT) calculation to model graphene's bare band that includes all electron-electron correlations.[73] In order to avoid any arbitrariness, determination of the bare band dispersion from the experimental data is desirable. Different approaches based on self-consistent procedures have been developed to determine the bare band, self-energy and ultimately, electron-phonon coupling strength.[76,82,83]

A self-consistent method has already been applied to the photoemission data of potassium doped graphene on Ir(111).[76] Several aspects of the low-energy quasiparticle dynamics were addressed: renormalization of the π^* band close to the Fermi level due to the coupling to phonons; phonon spectrum associated with the renormalization; the width of spectral lines in connection with the electron scattering rate. A model with a spectrum of five evenly spaced phonons participating in the coupling to graphene's π^* band was used in the self-energy analysis. The electron-phonon coupling constant was found relatively small (0.28) and isotropic around K. Rather broad peaks were interpreted in terms of an increased electron scattering rate caused by the loss of translation symmetry induced by the incommensurability of the system graphene/Ir(111).[76] An ARPES study on another metallic system — graphene on a copper foil — questions all previous findings, proposing an order of magnitude smaller electron-phonon coupling strength.[78]

We present here the results of an ARPES study of highly ordered graphene on Ir(111)[64,65] intercalated[84] with potassium. We use maxima of momentum distribution curves (MDC) and energy distribution curves (EDC) to determine the exact dispersion of the π^* band along the K-M direction. Peak positions and widths of MDCs are used in a self-consistent method to reconstruct the bare band E_b and the corresponding $\mathfrak{Im}\Sigma(E)$ and $\mathfrak{Re}\Sigma(E)$. Both show, consistently with the spectral intensity $A(E)$, that the renormalization is due to the coupling to two distinct phonon excitations. From the velocity renormalization and an increase of $\mathfrak{Im}\Sigma(E)$ with energy electron-phonon coupling constant is determined.

5.1 ELECTRON-PHONON COUPLING EXTRACTION METHOD

Photoemission spectra offer a wealth of information about many-body interactions in solids, in particular two-dimensional ones. The single-particle spectral function, that the intensities in the photoemission spectra are proportional to, is given by:

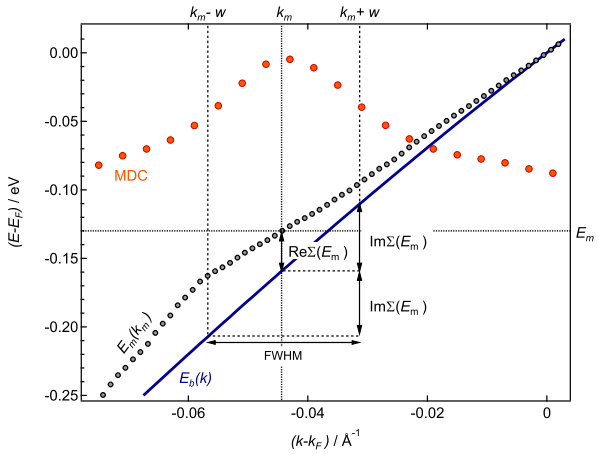

Figure 29: The figure illustrates the relations for $\mathfrak{Im}\Sigma$, $\mathfrak{Re}\Sigma$ and E_b in the case of actual experimental data on $E_m(k_m)$ and FWHM ($2\,w_m$). Also shown is an MDC for $E_m = -0.13$ eV having FWHM of 0.026 Å^{-1}.

$$A(k,E) = \frac{1}{\pi}\frac{\mathfrak{Im}\Sigma(E)}{[E - E_b(k) - \mathfrak{Re}\Sigma(E)]^2 + [\mathfrak{Im}\Sigma(E)]^2} \tag{5.1}$$

Here, E_b is the dispersion relation of the bare band, and $\Sigma = \mathfrak{Re}\Sigma + i\,\mathfrak{Im}\Sigma$ its many-body correction, so-called self-energy. The latter is usually taken to depend only on energy, as its momentum dependence is considered weak.[83]

If a cut at a given energy $E = E_m$ (momentum distribution curve) is made out of a two-dimensional map $A(k,E)$, nearly Lorentzian lineshape is obtained with a maximum at k_m such that

$$E_m - E_b(k_m) - \mathfrak{Re}\Sigma(E_m) = 0 \tag{5.2}$$

and a half-maximum at $k_m - w_{L\,m}$ and $k_m + w_{R\,m}$ ($w_{L\,m} + w_{R\,m} = 2\,w_m$ is then full-width at half-maximum, FWHM), where

$$\mathfrak{Im}\Sigma(E_m) = E_b(k_m) - E_b(k_m - w_{L\,m}) \tag{5.3}$$

as elaborated by Kordyuk *et al.*[82,85] Note that these relations do not rely on any specific dispersion of the bare band $E_b(k)$. The relations are illustrated in Figure 29 on a set of real experimental data for $E_m(k_m)$, FWHM ($2\,w_m$) and an exemplary MDC curve taken at $E_m = -0.13$ eV having FWHM of 0.026 Å^{-1}.

To use a linearized version of eq. 5.3, as it is often done,

$$\mathfrak{Im}\Sigma(E_m) = \hbar v_b(E_m)\cdot w_m \tag{5.4}$$

with

$$v_b(E_m) = \frac{1}{\hbar}\frac{d}{dk}E_b(k)|_{k=k_m(E_m)} \tag{5.5}$$

the measured band should be sufficiently sharp (w_m sufficiently small), and the bare band almost linear over sufficiently large pieces (giving a symmetric peak, $w_{L\,m} = w_{R\,m} = w_m$).

Even in our case of very narrow MDC peaks (0.010 Å^{-1}<w_m<0.022 Å^{-1}, or 0.007 Å^{-1}<w_m<0.018 Å^{-1} if the experimental resolution is deconvolved) this is only partially fulfilled, as can be seen from Figure 29. We have thus not used the linearized version of eq. 5.3.

The analysis of MDCs provides a set of value quadruplets (E_m, k_m, $2\,w_m$, A_m) evenly spaced on E_m. If the lineshape of an MDC is not far from Lorentzian, one has $w_{L\,m} \approx w_{R\,m}$, and can set them both equal to w_m — half-width at half-maximum, HWHM. The fact that each of the quadruplets is supposed to satisfy equations 5.1, 5.2, and 5.3 can help us determine the functional form of the bare-band $E_b(k)$, and the two components of the self-energy $\mathfrak{Re}\Sigma(E)$, $\mathfrak{Im}\Sigma(E)$ in the range of momenta and energies covered by the spectrum.

The procedure of extracting E_b, $\mathfrak{Re}\Sigma$, $\mathfrak{Im}\Sigma$ from the experimental data assumes that (i) the components of the self-energy must, by causality, comply with the Kramers-Kronig relation over the $\pm\infty$ range of energies; (ii) the upper half of the spectral function not accessible to ARPES ($E > E_{\mathrm{Fermi}} \equiv 0$) is substituted by supposing particle-hole symmetry; (iii) the high-energy tails of the three functions are not affected by a finite energy window for which the ARPES spectrum is available.[82,86]

If these criteria are met, the Kramers-Kronig transform of $\mathfrak{Im}\Sigma$ to $\mathfrak{Re}\Sigma$ (and vice versa)

$$\mathfrak{Re}\Sigma(E) = \frac{1}{\pi}\int_{-\infty}^{+\infty} \frac{\mathfrak{Im}\Sigma(\xi)}{\xi - E}\,\mathrm{d}\xi \tag{5.6}$$

if considered as a convolution of two functions, is easily calculated going through the time domain by Fourier transforms (FFT, in the discrete case)

$$[\mathfrak{Re}\Sigma(E)]_{\mathrm{FFT}} = \left[\frac{1}{E}\right]_{\mathrm{FFT}} \times [\mathfrak{Im}\Sigma(E)]_{\mathrm{FFT}} \tag{5.7}$$

In some numerical packages this is already provided as a discrete Hilbert transform.

The bare band and the components of the self-energy are usually reconstructed by assuming a polynomial (most often linear) form of the bare-band, from which $\mathfrak{Re}\Sigma(E)$ is calculated by both eq. 5.2 and a Kramers-Kronig transform of $\mathfrak{Im}\Sigma(E)$. Usually, not even the eq. 5.3 is used, but its expansion to the first order in w. The two forms of $\mathfrak{Re}\Sigma(E)$ are then compared, and the coefficients of the polynomial adjusted until the difference is minimal.[81,82,86,87]

We propose a simpler procedure here, that avoids the need for a minimization of a functional, and achieves the self-consistency in just a few iterations. The procedure also appears to be more stable with

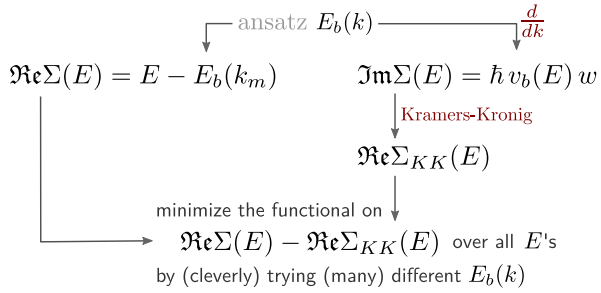

Figure 30: Procedures of finding the bare band $E_b(k)$ commonly rely on minimizing the difference between the two forms of $\Re\mathrm{e}\Sigma(E)$. Parameters that define the bare band are tried using Levenberg–Marquardt algorithm, for example.

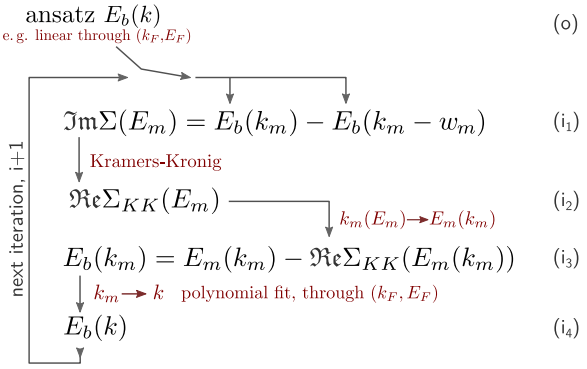

Figure 31: Iterative algorithm that refines the bare band E_b by enforcing the Kramers-Kronig relation between $\Im\mathrm{m}\Sigma$ and $\Re\mathrm{e}\Sigma$ self-consistently.

respect to the noise present in the experimental data, and no denoising[86] or smoothing by fitting to a function[76] is needed.

The algorithm, shown in Figure 31, starts by postulating a form, linear for example, of the bare band $E_b(k)$. Forcing the function to pass through the experimentally determined point (k_F, E_F) can help in faster convergence. Note that this constraint is physically sound, as the renormalized and the bare-band are expected to intersect at the Fermi level. In the first step of the iterative procedure, $\Im\mathrm{m}\Sigma$ is calculated by eq. 5.3. In the second step $\Re\mathrm{e}\Sigma$ is obtained by a discrete Hilbert transform of $\Im\mathrm{m}\Sigma$. This is used by eq. 5.2 to refine the bare band, first on a discrete set of points (step 3), then fitted to a polynomial or a function at wish (step 4). The functional form of $E_b(k)$ is then used to calculate $\Im\mathrm{m}\Sigma$ in the next iteration. The iteration ends when there are no substantial changes in the functions (or parameters) obtained. The full IgorPro code, exemplary input data and some more details on the procedure are given in Appendix B.

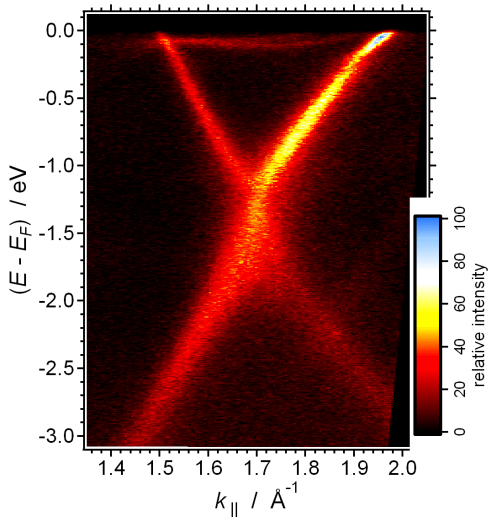

Figure 32: ARPES spectrum (excitation energy 40.5 eV, *s* polarization, scan direction Γ-K-M) showing the intensity of photoemission from the Dirac cone in graphene/Ir(111) saturated with potassium.

Electron-phonon coupling strength can be extracted[88] either from a steplike increase of the imaginary part of the self-energy, $\Delta\Im\mathfrak{m}\Sigma$, as

$$\lambda = \frac{2}{\pi}\frac{\Delta\Im\mathfrak{m}\Sigma}{\hbar\omega_{ph}} \tag{5.8}$$

or from the real part of the self energy, as

$$\lambda = -\frac{\mathrm{d}}{\mathrm{d}E}\Re\mathfrak{e}\Sigma(E)|_{E=E_F} \tag{5.9}$$

Although these two equations are strictly valid only at zero temperature, they are especially good approximation in the case of graphene, where phonon excitations are high in energy.

Instead of calculating the derivative in eq. 5.9 directly, which is liable to errors due to the noise and scarcity of reliable data in the very proximity of the Fermi level, one can make use of eq. 5.2, through $\lambda = -\frac{\mathrm{d}}{\mathrm{d}E_m}(E_m - E_b(k_m)) = \frac{E_b'(k)}{E_m'(k)} - 1$, to get

$$\lambda = \frac{v_b(E_F)}{v_r(E_F)} - 1 \tag{5.10}$$

Here, v_b (v_r) is the Fermi velocity of the bare (renormalized) band.

5.2 HIGHLY DOPED GRAPHENE

5.2.1 *Experimental results*

Figure 32 shows photoemission spectrum of potassium-intercalated graphene on Ir(111) around the K point along the Γ-K-M direction.

The spectrum shows a discernible asymmetry of the intensity, such that the part of the spectrum of the π^* band along K-M ($k > 1.7$ Å^{-1}) exhibits much stronger intensity than the part dispersing along K-Γ ($k < 1.7$ Å^{-1}). Notice that iridium surface state at the Fermi level, also present in the spectrum for graphene/Ir(111),[64] is not quenched by the intercalation of potassium. Potassium doping, however, has rather strong effect on the π bands of graphene — shifts the Dirac point to higher binding energies and renormalizes the band dispersion just below the Fermi level.

The position of the Dirac point, being defined as a single point in momentum space where the π bands cross each other, is not straightforward to determine. As can be seen from Figure 32 there is no such well-defined crossing point here. This is presumably due to a band gap, as a study by Varykhalov *et al.*[89] has shown that some metallic dopands do induce a band gap at the Dirac point. We estimate the width of the band gap to be 0.3 eV with the position of the Dirac point at 1.35 eV below the Fermi level, which is, within a tenth of an eV, equal to the values previously obtained for graphene/Ir(111)[76] and some other systems, such as graphene/SiC[73] and graphite[74].

The shift of the Dirac point to higher binding energies causes an increase of the Fermi surface, which is for higher doping levels characterized by trigonal warping; i. e. an effect when a transformation of the constant energy maps from circular to trigonal shape takes place.[66,73] The trigonal warping is clearly associated with different values of k_F for the π^* band dispersing from K to M or Γ. We have determined k_F along the directions K-Γ and K-M to be 0.18 Å^{-1} and 0.27 Å^{-1} respectively, and used these values to estimate the doping level of about 0.05 electrons per unit cell.

A prominent feature of the spectrum in Figure 32 is the renormalization of the K-M branch of the π^* band just below the Fermi level. No such renormalization is as obvious for the branch K-Γ. This kink-like change of the band dispersion is detailed in Figure 33.

As we have pointed out, two parts of the spectrum in Figure 32 show a considerable difference of spectral intensity. The change of the light polarization can additionally alter this intensity ratio. We used p polarization of the incident light in order to extinguish spectral features along K-Γ entirely, leaving only the part of the π^* band along the K-M direction visible. The origin of the diminishing spectral intensity has been explained by Gierz *et al.*[52] The change of the light polarization strongly enhances signal to noise ratio which shows to be essential in detailed spectrum analysis, as will be demonstrated in the following. Simple inspection of Figure 33 places the phonon induced dispersion kink at around 200 meV below the Fermi level. Notice how the dispersion kink is now even more pronounced, accompanied by a strong drop of the spectral intensity at the kink.

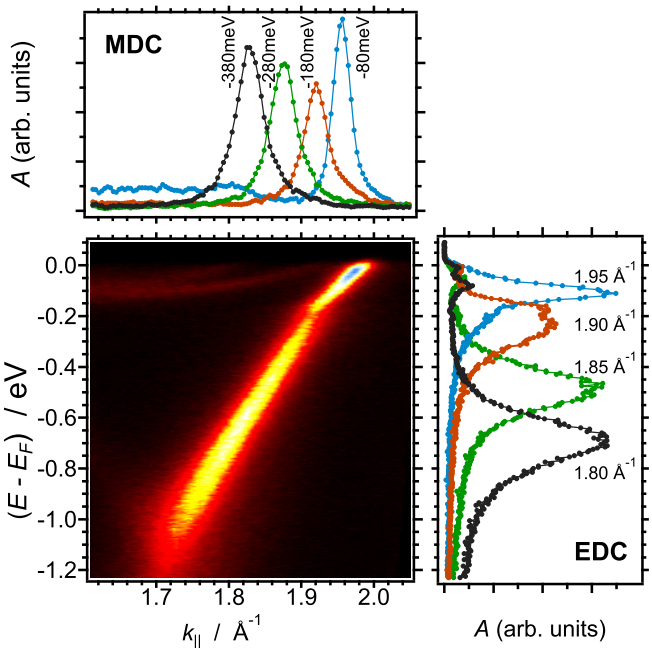

Figure 33: ARPES spectrum of potassium intercalated graphene/Ir(111) (excitation energy 40.5 eV, *p* polarization, scan direction Γ-K-M) along with a few selected MDC and EDC cuts at given energies and momenta.

5.2.2 *Analysis and discussion*

A set of MDC and EDC cuts in Figure 33 illustrates the kind of analysis made for each and every slice of the ARPES spectrum shown. MDCs are generally characterized by a continuous change of the peak position without any substantial change of the lineshape, apart for the width of the peaks. However, in the narrow region around the kink, the EDCs clearly exhibit double peak structure, that can be fitted with two Lorentzians (see the figure aside). The energy splitting between the peaks is found to be around 60 meV. Farther away, ±70 meV from the kink, EDCs can be described by a single Lorentzian. A small peak visible just below the Fermi level is associated with the S_1 surface state of Ir(111).[42]

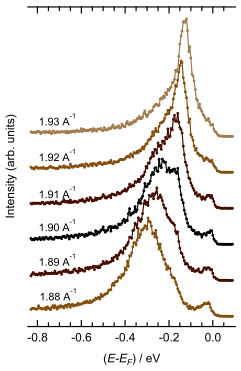

Note that the full width at half maximum of the MDC at an energy just below the Fermi level (Figure 32) is 0.022 Å^{-1}, which is even slightly smaller than the width measured for bare graphene on Ir(111)[65] and comparable to non-intercalated graphene on SiC[67]. Moreover, the measured width is substantially smaller than the previously reported value of 0.095 Å^{-1} for the same system.[76] This questions the conclusion by Bianchi *et al.*[76] that the doping of graphene on Ir(111) by potassium increases the electron scattering rate due to the loss of translation symmetry induced by the incommensurability of graphene and Ir(111). Our data imply that the intercalation of potassium, observed as a disappearance of graphene's moiré super-

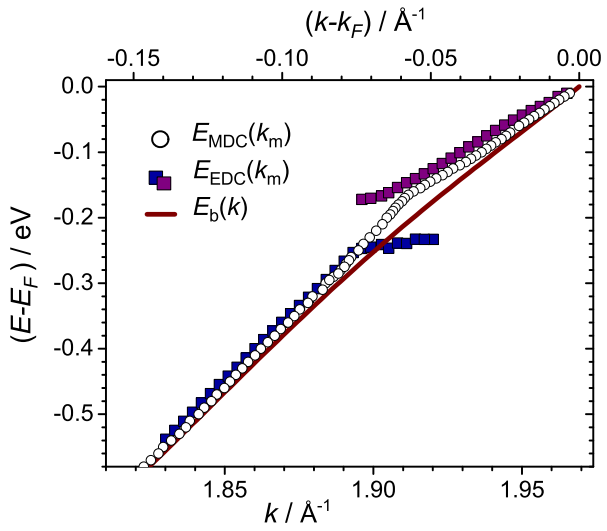

Figure 34: Peak positions extracted from MDC cuts (circles) and EDC cuts (squares) of the spectrum shown in Figure 33. Thick line shows the bare-band $E_b(k)$ obtained from the self-consistent procedure.

structure, does not increase the electron scattering rate compared to bare graphene on Ir(111). Therefore, we can conclude that potassium intercalated in a graphene/Ir(111) system does not act as an additional scattering center. As we will demonstrate later, the measured value of the MDC width translates into rather big quasiparticle scattering time. The MDC width increase (to 0.042 Å^{-1}) measured below the dispersion kink (Figure 32) fits into the picture of phonon-induced renormalization of the π^* band.

Figure 34 summarizes the peak positions obtained from MDC and EDC sets of spectra from Figure 33. Open circles represent peak positions obtained from the analysis of MDCs, while squares are obtained from EDCs. The fact that the two dispersions do not coincide, especially in the region above the kink is easy to understand when one takes into account that the spectral intensity of the band sharply changes, and that what is a local maximum k_m in a horizontal cut along $E = E_m$ does not have to be a local maximum in a vertical cut along $k = k_m$. The data below and above the kink are fitted with two linear functions with noticeably different slopes. The data far away from the Fermi level can be fitted with a linear curve and the corresponding band velocity equals to $0.7 \cdot 10^6$ m/s. This represents a reduction of about 30% compared to the π band of nearly neutral graphene on Ir(111), and is consistent with the predicted reduction of the Fermi velocity, as calculated by Park *et al.*[90] The set of MDC data between the Fermi level and the kink is also fitted with a linear function defined by the band velocity (which is in this case the Fermi velocity as well) $v_r(E_F) = 0.46 \cdot 10^6$ m/s. Note that this value is only about half the Fermi velocity of the π band in bare graphene on

Ir(111)[65] and the π^* band on SiC[69]. This renormalization of the velocity can lead to an overestimate of the coupling strength to phonons for the simple reason that the change of the electron velocity near E_F is largely due to the curvature of the π^* band induced by other interactions and only to small extent by electron-phonon coupling.[80]

In order to take into account the nonlinearity of the π^* band, the bare-band function $E_b(k)$ was self-consistently reconstructed from the MDC data, by the recursive procedure described above. The π^* band itself has been measured far below the phonon-induced kink, where the contribution to $\Re\mathfrak{e}\Sigma$ can be neglected and the bare-band approaches the measured.[82] This gives confidence to the functions obtained, as the problem of tails is greatly avoided. The corrections of $E_m(k)$ leading to $E_b(k)$ being mostly due to low-energy phonon excitations, the function $E_b(k)$ can be considered as one that takes into account all electron interactions except those with phonons.

The derivative of the bare function at the Fermi level gives the Fermi velocity for the bare band $v_b(E_F) = 0.56 \cdot 10^6$ m/s. The obtained values of band velocities, at the Fermi level and far away from the kink, are in very good agreement with the values of the band velocities for highly doped graphene, reported by Siegel *et al.*[69]

To summarize, it is clear that a large portion of the velocity reduction as we approach the Fermi level comes from the non-linear nature of the bare π^* band. The modification of the Fermi velocity due to the coupling to phonons is accordingly rather small, around $0.1 \cdot 10^6$ m/s, which is only a 10% change.

The ratio between the Fermi velocity of the bare band and the electron-phonon-induced renormalized velocity at the same energy gives, by equation 5.10, the value of the electron-phonon coupling strength. Accordingly, the value of λ along the K-M direction equals to 0.22. The same analysis on the K-Γ direction gives $\lambda = 0.19$. Previously, Bianchi *et al.*[76] obtained $\lambda = 0.28$ for both directions.

We use MDCs extracted from the spectrum shown in Figure 33 to plot (a) imaginary part of the self-energy, $\Im\mathfrak{m}\Sigma(E)$ (b) real part of the self-energy, $\Re\mathfrak{e}\Sigma(E)$ and (c) spectral intensity of the MDC peaks, $A(E)$. Figure 35 shows the results. The functions plotted in black were calculated from formulæ (5.1)–(5.3) using the bare-band from our self-consistent iterative procedure. The functions shown in red illustrate the degree of self-consistency achieved; the one for $\Im\mathfrak{m}\Sigma_{KK}$ in Figure 35a was obtained by Kramers-Kronig transformation of the data for $\Re\mathfrak{e}\Sigma$ from Figure 35b, and equally, the one for $\Re\mathfrak{e}\Sigma_{KK}$ from the data for $\Im\mathfrak{m}\Sigma$. The overall agreement is quite good. We find the data for FWHM and consequently for $\Im\mathfrak{m}\Sigma$ more reliable, the noise being pretty low and the relative error being smaller in determining the width of the MDCs than the peak positions, from which $\Re\mathfrak{e}\Sigma$ is calculated. The effects of experimental smearing also have a greater impact on the fine details of MDC peak positions, adding only a constant

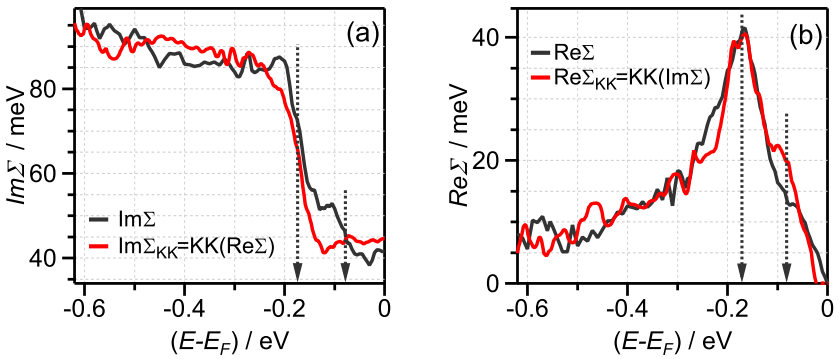

Figure 35: A set of self-consistent functions obtained from MDC cuts of the spectrum along the K-M direction shown in Figure 33 and the bare-band shown in Figure 34. (a) black line: $\Im\mathfrak{m}\Sigma$ calculated by equation 5.3; red line: $\Im\mathfrak{m}\Sigma_{KK}$ as a Kramers-Kronig transform of $\Re\mathfrak{e}\Sigma$; (b) black line: $\Re\mathfrak{e}\Sigma$ calculated by equation 5.2; red line: $\Re\mathfrak{e}\Sigma_{KK}$ as a Kramers-Kronig transform of $\Im\mathfrak{m}\Sigma$. Arrows indicate the energies of phonons that induce band renormalization.

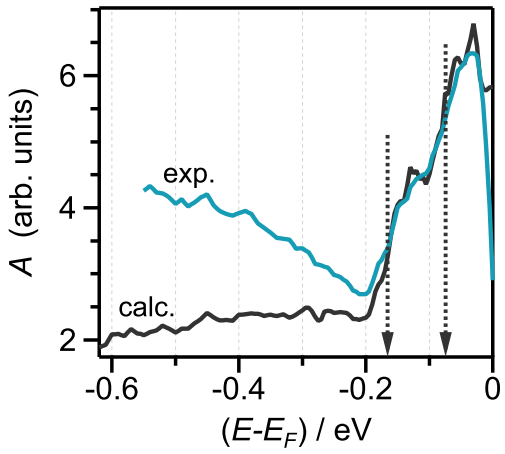

Figure 36: Spectral intensity $A(E)$ from the experiment (blue line) and calculated from the self-consistent data by equation 5.1 (black line). Arrows indicate the energies of phonons that induce band renormalization.

background to FWHMs and $\mathfrak{Im}\Sigma$. We suspect that the low-energy shoulder in $\mathfrak{Re}\Sigma$ (and the associated step in $\mathfrak{Im}\Sigma_{KK}$) are for these reasons less pronounced than the corresponding ones in $\mathfrak{Re}\Sigma_{KK}$ (and $\mathfrak{Im}\Sigma$). The difference in experimental and calculated spectral intensities in Figure 36 at the high-energy side probably comes from the fact that the calculated renormalized band $E_b(k_m) + \mathfrak{Re}\Sigma(E_m)$ does not come close enough to the measured band $E_m(k_m)$, as the increase of the spectral function would come from one approaching the other (see equation 5.1). We suspect this could be a still-observable consequence of the missing high-energy tails[82].

Generally, a step-like increase of $\mathfrak{Im}\Sigma(E)$ and a maximum of $\mathfrak{Re}\Sigma(E)$ at the same energy is associated with electron coupling to some excitation, in this case phonons. As pointed out by McChesney *et al.*[87] the coupling to a phonon should have a profound impact on the energy dependence of the spectral intensity $A(E)$ as well.

Instead of one, all displayed spectral parameters show consistently two features that can be accordingly associated with the coupling to two phonons, one at 170 meV and the second one at 75 meV. Arrows in Figures 35 and 36 indicate the energies of these two phonons.

The $\mathfrak{Im}\Sigma(E)$ (Figure 35a) shows a distinct step-like increase between 0.05 and 0.1 eV below the Fermi level with the initial value of 39 meV which reaches a local maximum of 52 meV at 0.1 eV. This increase of $\mathfrak{Im}\Sigma(E)$ is associated with the phonon of energy 75 meV. Further increase of $\mathfrak{Im}\Sigma(E)$ up to 85 meV induced by the coupling to a phonon of 170 meV takes place between 0.13 and 0.21 eV. Below that, $\mathfrak{Im}\Sigma(E)$ stays constant up to 0.4 eV, but then starts to increase with energy, due to other contributions to the lifetime (electron-electron, electron-plasmon).[67]

Electron-phonon coupling constant can be extracted from the change of $\mathfrak{Im}\Sigma(E)$ by equation 5.8.[73,88] The total increase of $\mathfrak{Im}\Sigma(E)$ equal to 46 meV, translates to $\lambda = 0.17 \pm 0.01$ along the K-M direction. A similar analysis of $\mathfrak{Im}\Sigma(E)$ along the K-Γ direction, shown in Figure 37, gives $\lambda = 0.18 \pm 0.02$.

$\mathfrak{Re}\Sigma(E)$, in consistence with $\mathfrak{Im}\Sigma(E)$ and $A(E)$, exhibits a peak at 170 meV and a distinct shoulder at a lower binding-energy side, which clearly implies an existence of two excitations that contribute to the renormalization of the bare band dispersion.

Using the imaginary part of the self-energy in the proximity of the Fermi level, we determine the photohole scattering time, $\tau = \frac{\hbar}{2\,\mathfrak{Im}\Sigma}$,[91] to be bigger than 10 fs. This is the same value as obtained for high quality graphene on SiC.[55] Note that this value is not to be compared to the scattering time in mobility measurements ($\sim$ 350 fs), as those include some more scattering mechanisms.[91]

As pointed out, the energy dependence of the spectral intensity $A(E)$ also indicates the existence of two distinct phonon excitations that couple to electrons. McChesney *et al.*[87] have demonstrated a high

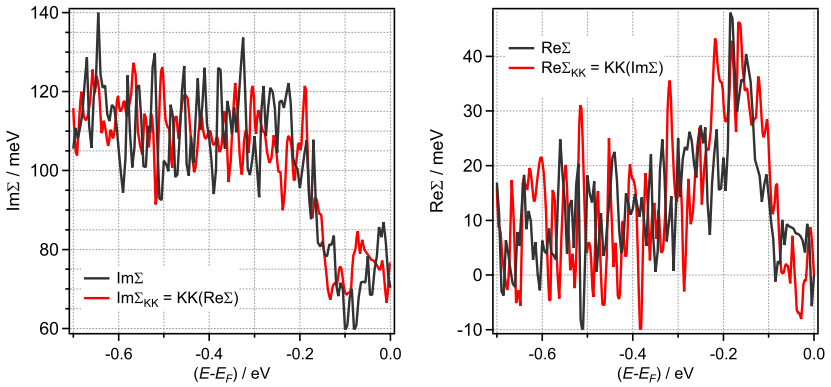

Figure 37: A set of self-consistent functions obtained from MDC cuts along the K-Γ branch of the π^* band that was recorded with *s* polarized light. (a) black line: $\Im\mathfrak{m}\Sigma$ calculated by equation 5.3; red line: $\Im\mathfrak{m}\Sigma_{KK}$ as a Kramers-Kronig transform of $\Re\mathfrak{e}\Sigma$; (b) black line: $\Re\mathfrak{e}\Sigma$ calculated by equation 5.2; red line: $\Re\mathfrak{e}\Sigma_{KK}$ as a Kramers-Kronig transform of $\Im\mathfrak{m}\Sigma$.

sensitivity of $A(E)$ to many-body interactions, drawing attention to the fact $A(E)$ can access even a faint contributions to the self-energy with a sensitivity even better than $\Im\mathfrak{m}\Sigma(E)$ can provide. In agreement with this model we observe two shoulders in $A(E)$ where an onset of each shoulder corresponds to a phonon excitation (see Figure 2 in[87]). Summarizing the features that have been observed in three parameters: $\Im\mathfrak{m}\Sigma(E)$, $\Re\mathfrak{e}\Sigma(E)$ and $A(E)$, we can conclude, with a high degree of consistency, that the phonon energies that induce the renormalization of the dispersion of the π^* band of doped graphene along the K-M direction have energies equal to 170 meV and 75 meV. These two phonons can be associated with an optical phonon (transverse or longitudinal) around K and an acoustic phonon, respectively. According to González and Perfetto[92], in non-interacting graphene these phonons should be in-plane oscillations as the symmetry does not allow coupling of the out of plane phonons to electrons in graphene. However the presence of the substrate might break the 2D symmetry of graphene and hence allow the coupling of both in-plane and out-of-plane oscillations to electrons in graphene.

Theoretical calculations also support the notion of a two-phonon spectrum that induces renormalization of graphene bands close to the Fermi level. According to Calandra and Mauri[91], the π^* band of doped graphene should show two kinks in the dispersion (accordingly accompanied by two steps in the MDC linewidth), one at 195 meV being attributed to A_1 mode and another at 160 meV which corresponds to a twofold degenerate E_{2g} mode. Previous measurements of Bianchi *et al.*[76] with graphene on Ir(111) showed signatures in the band dispersion and widths of spectral curves of apparently only one phonon. However, their self-consistent analysis showed that the experimental data can be modelled by contributions of five Ein-

stein oscillators with energies that are evenly distributed over the range from 21 meV to 190 meV.

Interestingly, the pattern of coupling similar to the one we observed in graphene/Ir(111) is also reported for CaC_6 where the contributions to the self-energy come from two phonons, one at 75 meV and the other at around 160 meV.[74] This agreement supports the notion that intercalated atoms (K or Ca) do not participate in the coupling of the π^* band to phonon modes apart from the doping effect.

The energy splitting between the EDC peaks has already been observed in materials with strongly coupled electrons and phonons.[93,94] Although the coupling in graphene is not as large, Badalyan and Peeters[95] find its two-dimensionality a possible reason for an enhancement of the effective coupling in the vicinity of the phonon energy. An electron-phonon complex quasiparticle forms, giving rise to a strong modification of the Dirac spectrum, seen as the branches of the π^* band in the neighborhood of the phonon emission threshold.

The value of the electron-phonon coupling constant obtained in this work (~ 0.2) is somewhat smaller than the one obtained by Bianchi *et al.*[76] for the same system (~ 0.3). Nevertheless, the value derived from our spectra does not support the notion of Siegel *et al.*[78] that the coupling in n-doped graphene on a metallic surface should be still a few times smaller (~ 0.04). Given sharp enough spectra, low in background intensity and noise, a pronounced kink in the π^* band dispersion, and especially a steplike increase of the spectral width at the phonon energy, must alone be a clear sign of a non-negligible strength of interaction, whatever the choice for the bare band is.

It would be interesting to see if different dispersions in the two directions are responsible for the kink being more obvious in the K-M direction. Spectral functions can be simulated with the same lambda ($\lambda = 0.2$) in the K-M and K-Γ direction. We do this by first recognizing that the same e-ph coupling parameter $\lambda = 0.2$ for the phonon of energy $\omega_{ph} = 170$ meV means, by equation 5.8, the same step in the imaginary part of the self energy. This would be $\Delta\Im\mathfrak{m}\Sigma = 55\,\text{meV}$ for both branches. The real part of the self energy is obtained by the Kramers-Kronig transformation of the imaginary part, assuming particle-hole symmetry. Figure 38 illustrates the functions obtained.

We then take two linear bare bands, one mimicking the dispersion of the K-Γ branch (band velocity $1 \cdot 10^6$ m/s), the other the dispersion of the K-M branch (band velocity $0.6 \cdot 10^6$ m/s), and simulate the spectral function by equation 5.1. The results are shown in Figure 39.

The renormalized bands can be either extracted from the spectral function following the dispersion of MDC peaks, or calculated by equation 5.2. This is done self-consistently, starting with $E_m^0 = E_b(k) + \Re\mathfrak{e}\Sigma(E_b(k))$ and iterating over $E_m^{i+1} = E_b(k) + \Re\mathfrak{e}\Sigma(E_m^i)$. The result can be immediately compared to the experimental data. It is evident from Figure 40 that even the simple linear band closely fol-

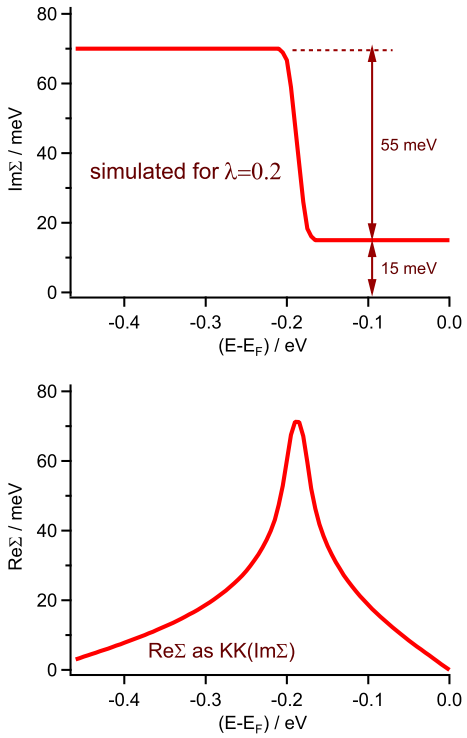

Figure 38: Simulation for $\lambda = 0.2$ of the jump in the imaginary part of self energy at $\hbar\omega_{ph} = 170$ meV and the real part of self energy as its Kramers-Kronig transform.

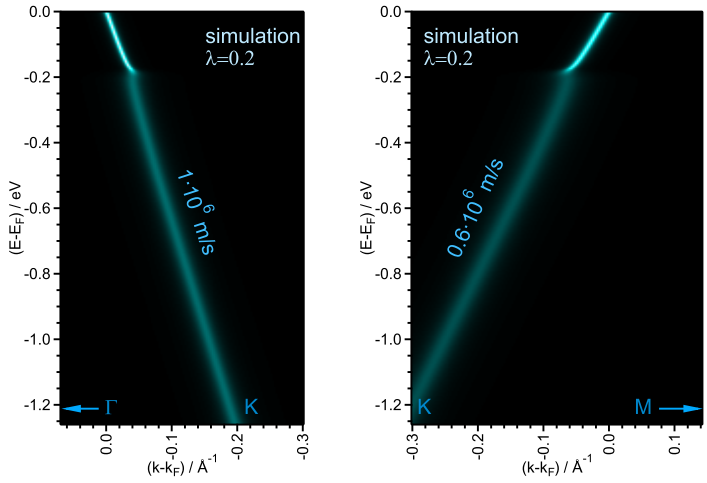

Figure 39: Spectral function simulated using equation 5.1 with linear bare bands reproducing high-energy tails of renormalized bands of doped graphene and the parts of self energy displayed in Figure 38.

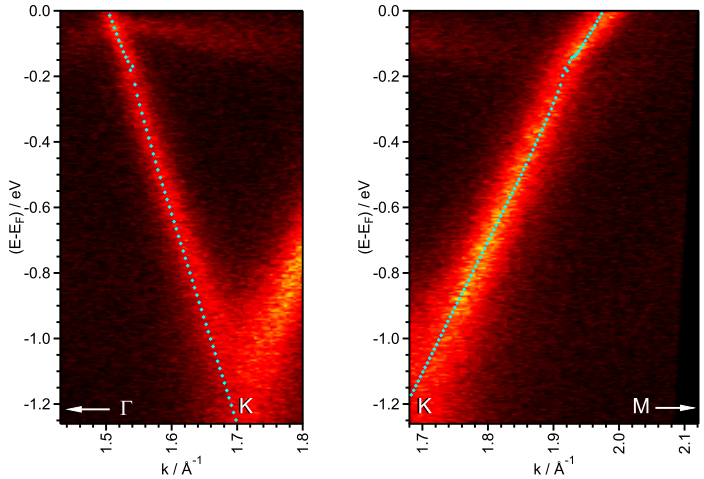

Figure 40: Comparison of experimentally determined branches (K-Γ and K-M) of the π^* band of doped graphene with the maxima of spectral function simulated in Figure 39.

lows the measured band in a wide range below the kink, as well as its renormalized part follows the band above the kink. And indeed, the kink is more obvious for the band dispersing more slowly, i. e. the band simulating the dispersion along the K-M direction.

6

SUMMARY AND OUTLOOK

We have seen that not only that graphene grown on Ir(111) brings some new physics with its superperiodic ordering but also provides an exceptional structural quality which can be utilized in studying some of more general properties, namely the interaction of phonons with quasiparticles — electrons and holes — in a genuinely two-dimensional system. The fundamental properties of graphene itself can be investigated owing to the weak interaction with the substrate, which is mainly of the van der Waals nature.

Our experiments single out graphene on Ir(111) as a material with unique properties among the known epitaxial graphenes. In distinction to graphene on Ni(111)[96,97] or Ru(0001)[28,98,99] it is weakly interacting. In distinction to graphene on SiC(0001)[51,59,60,61,62,100,101] or two-layer graphene on Ru(0001)[99] it is a simple system with no carbon-rich intermediate layer necessary to passivate the substrate. The electronic bands of graphene on Ir(111) near the K point are intact, with only marginal hole doping by the substrate. The superperiodic potential associated with the moiré gives rise to the formation of replica cones and opens a minigap in the π band.

Determination of the electron-phonon coupling strength in highly doped graphene turned out to quite reliable, as graphene remained unaffected (except for electron doping) by the presence of ionized potassium atoms that could act as scattering centers. The value of the electron-phonon coupling constant $\lambda = 0.2$ obtained from a new procedure of extracting the (photo)hole self energy adds to mostly dissonant discussion of the subject. The procedure itself is robust, efficient, and error prone and can be applied to many systems in the future.

In quest of the ways of patterning graphene for possible nanoelectronic integrated structures, one could count on the effects of the superperiodic potentials, antidot lattices produced by selective hydrogenation or complete removal of certain parts of the moiré. Yet another method would be to prepare graphene in the way we did, but on already patterned few-layer iridium that would be etched afterwards.

Whether or not there will be technological breakthroughs based on graphene remains to be seen, but physics has already benefited by gaining knowledge on this exotic two-dimensional material.

Part III

APPENDIX

A

EXPERIMENTAL SETUPS

A.1 PREREQUISITES

The main experimental prerequisite is a clean ultrahigh vacuum in the range well below 10^{-7} Pa. Residual gas pressure is monitored with ionization gauge and analyzed with mass spectrometer; the largest fraction in residual gases belonging to H_2 and CO. Demanding requirements are put on the equipment, as the experimental setups have to enable:

HEATING for the preparation of a clean and ordered iridium surface, as well as buildup of graphene. Steady sample temperatures of up to 1700 K have to be reached by electron-beam bombardment from the back of the sample.

COOLING during the preparation of graphene, when relatively short time (~10 minutes) between the cycles is desired for the iridium sample to reach the room temperature and accept new ethene adsorption. Beside that, cooling to cryogenic temperatures is required during the ARPES measurements, in order to refine the spectral features.

TEMPERATURE MEASUREMENTS in the high-temperature as well as cryogenic temperature range, with an accuracy better than 1%.

ION BOMBARDMENT for the cleaning of the sample surface by high energy (1000 eV) ions of argon or xenon; high flux ion gun should be available

PRECISION GAS DOSING of high-purity oxygen for surface cleaning and ethene for the production of graphene, through all-metal leak valves capable of maintaining a constant pressure in the range of 10^{-7} Pa to 10^{-4} Pa.

ALKALI EVAPORATION by current heated commercially available alkali getters (Li, Na, K, Cs) attached to ultrahigh-vacuum electrical feedthroughs, at a distance of 10-20 cm from the sample.

ORIENTATION CONTROL for polar, azimuthal, and tilt angle of the sample surface is highly desirable for one has to reach a specific *point* in momentum space far away from normal emission. Low energy electron diffraction (LEED) can be used as a rough check only, as the accuracy of reading an angle from the diffraction image is above 1°, and the manufacturing accuracy for the cham-

ber ports not better than 1°. Due to fast dispersing graphene's bands, even deviations of 0.1° are visible in spectra.

UV LIGHT of as high as possible intensity, monochromatic, of a known energy and polarization.

Additionally, parts of the sample holder in contact with the sample should be made of materials having high melting point that will in no circumstance form an alloy with iridium. The latter excludes tantalum and molybdenum, leaving only tungsten in consideration.

A.2 LABORATORIES

The experiments have been conducted at three systems equipped with high-resolution electron analyzers.

Surface physics laboratory, Institute of physics, Zagreb/Croatia

Most preliminary measurements, some of which are also shown in this work, have been made at the experimental setup of our laboratory at Zagreb. A vacuum chamber has been custom built out of μ-metal alloy to suit the needs of magnetic shielding in photoemission experiments and port arrangement for all the equipment planned. An unfortunate consequence of the choice of μ-metal as a building material for the chamber was intolerable outgassing through micropores left after welding, main constituents being argon and methane. The problem was solved by silvering the interior of the chamber, after many other unsuccessful tries.

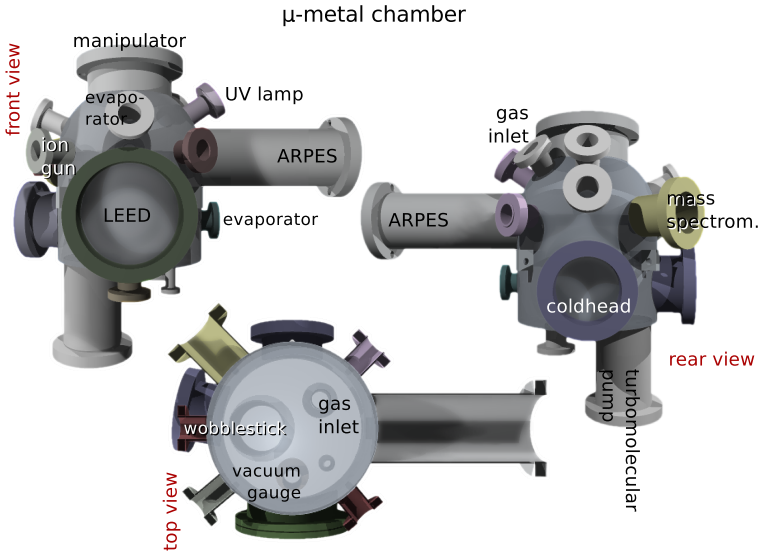

Pumping system is placed at the end of a basal plate 100 mm port, and consists of a 220 L/s turbomolecular pump backed up by a rotary vane pump, and a titanium sublimation pump located at an arm

of the same port. After a thorough system bakeout at 150°C, base pressures of $< 5 \cdot 10^{-8}$ Pa are usually achieved. A quadrupole mass analyzer measured H_2 as a dominant residual gas, but with a small addition of methane probably coming from the titanium film gathered at the wall of sublimation pump.

Experimental samples are mounted on an ultrahigh-vacuum manipulator capable of 150 mm z-axis and 25 mm x- and y-axis translation, as well as full circle rotation about the z-axis (equaling to alteration of sample's polar angle ϑ). The angle of rotation can be read off a vernier scale (nonius) with a precision of 0.1°. Several feedthroughs exist at the manipulator, allowing connections of thermocouples and electrical power wires. Sample holder is a versatile device built at Institute's mechanical workshop. A number of requests were put upon it — had to be small in size to fit the available space; had to encompass a floating filament as an e-beam source; it had to enable an inexpensive means of azimuthal rotation, by means of an improvised wobble stick at one of the horizontal ports; should have been easy to (re)connect to the cooling facility lower in the chamber by a flexible copper braid; should not outgass excessively when heated; all the front side wires should be uninsulated to avoid charge buildup under the ultraviolet light, etc.

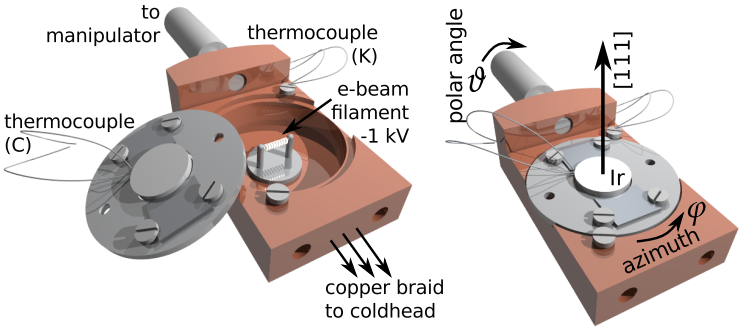

Heating by electron beam bombardment is powered from a custom built 1000 V, 150 W switching power supply. The sample being grounded for the sake of better thermal contact and faster cooling, the filament at the back of the sample is operated by a current source floated at high negative voltage.

For the cooling a closed-cycle helium refrigerator (Leybold corporation) is used with a 6 W cooling head capable of reaching temperatures of ~20 K at its tip. The coldhead, however, is never to be attached to the chamber during the system bakeout at 150°C, hence a special adapter has been devised to connect the coldhead without breaking the ultrahigh vacuum. Overall thermal losses at the adapter are by design less than 2 W. A thick copper braid connects the head of the adapter to the bottom side of the sample holder, enabling its cooling down to 45 K.

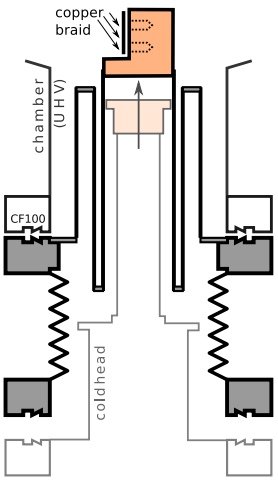

The temperatures are in ultrahigh vacuum usually measured by thermocouple wires attached to the sample. Most frequently used K-type thermocouple (chromel-alumel), however, has to be avoided here for its components make alloys with iridium. Moreover, when reaching the temperatures as high as 1700 K thermocouple type C ($W_{95}Re_5$-$W_{74}Re_{26}$) is a much better choice. However, the bottom of its operating range is limited to ~300 K, the thermocouple becoming far less sensitive and quite non-linear in the cryogenic temperatures. For those measurements, K type wires are attached to the sample holder, as close to the sample as possible.

All-metal leak valves are mounted at several ports of the chamber, allowing for precision dosage of oxygen (needed in firing of carbon chemisorbed at the sample surface), ethene (needed for graphene production), argon, deuterium, etc. The chamber pressures of these gasses can be controlled in minute steps from $1 \cdot 10^{-7}$ Pa to $5 \cdot 10^{-4}$ Pa.

Cleaning of the surface by sputtering is achieved by means of an ion gun capable of delivering high flux of high-energy ions, usually argon or xenon. The gun (SPECS IQE 12/38) is of a scanning type, having control of position and area of an ion beam.

Two high current vacuum feedthroughs were prepared to easily incorporate small alkali metal dispensers (SAES getters corporation). The dispensers filled with a mixture of alkali metal chromate with a reducing agent offer upon heating vapor flux of high controllability, stability and reproducibility. Although only results with potassium are shown here, lithium, sodium, and cæsium were tried as well.

Finally, a few notes about two pieces of equipment that are crucial for ARPES experiments — ultraviolet light source, and high-resolution electron analyzer.

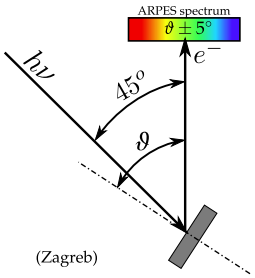

As the light source a noble gas discharge lamp is used (SPECS UVS 10/35). Depending on the gas flow conditions in the capillary where the high-voltage discharge is initiated, noble gas plasma emits distinct spectral lines of well defined frequency. Helium I spectrum is dominated by photon energy $h\nu$ of 21.22 eV. Neon I spectrum is always a doublet of energies 16.85 eV and 16.67 eV; these can hardly be used to reach the K point in graphene's spectrum, as the polar angle would need to be greater than 80°, as opposed to 55° when He I excitation is used. With a quartz capillary of 1 mm diameter acting as a light guide, a lower estimate of the beam spot size at the sample surface that is ~50 mm away from the capillary end is 1.5 mm. The light is not polarized.

The electron energy analyzer is a 100 mm mean radius hemispherical electrostatic device (Scienta SES100) equipped with an entrance electrostatic lens capable of resolving electron emission angles in the range of ±5°. The photoemission spectra are collected at the exit of the hemispheres by a microchannel plate as two-dimensional maps of the photoelectron intensity dependence on kinetic energy and emis-

sion angle relative to the lens axis, $I(E_{\text{kin}}, \Delta\vartheta)$. Although the nominal resolution of the analyzer is 5 meV (at 5 eV pass energy) and 0.1°, these values are hardly reached in final spectra where the resolution is spoiled by finite excitation line width, sizable UV-beam spot size, strain magnetic fields, roughness of the surface... Energy resolution has been previously determined from the Fermi edge blurring at low temperatures. A convolution of the theoretical Fermi distribution with a gaussian having parameter $\sigma = 20$ meV was found to emulate the observed feature in the spectrum the best. Angular resolution is harder to determine, and one can just hope that no considerable broadening due to finite beam size takes place, i. e. that the entrance lens focusing is such that it discriminates electrons emitted from any broader excitation area.

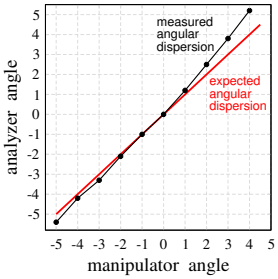

As a consequence of fast dispersing electronic bands of graphene, a nonlinearity in the angular dispersion of the analyzer has been discovered. Namely, in the geometry of our experiment, the absolute polar angle is set by means of manipulator rotation and the analyzer acquires a ±5° scan around that value. As the spectra taken in a series of manual polar-angle alterations did not overlap, the difference between the measured and expected angles being at the ends of the detector larger than 1°, a procedure of correcting them programmatically in 2D ARPES maps $I(E_{\text{kin}}, \Delta\vartheta)$ has been devised and subsequently applied to all the obtained spectra.

ELETTRA Synchrotron, Trieste/Italy

Elettra is the third generation storage ring where synchrotron radiation produced by electrons traveling at relativistic speeds (2 GeV) is used at 26 beamlines comprising photoemission, imaging, diffraction, reflection, absorption, and lithography techniques. The source of high brightness photons are insertion devices, i.e. arrays of magnetic poles that force the circulating electrons along serpentine trajectories. The wavelength of the light (hence the photon energy) is tunable by changing the magnetic field acting on the electron beam. Depending on the magnetic configuration these devices can also be made to produce either linearly or circularly polarized light.

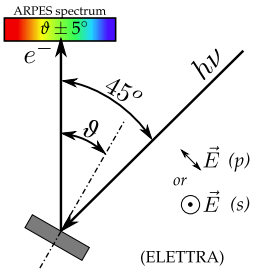

The ARPES experiments at Elettra have been conducted at the Advanced photoemission (APE) beamline,[102] offering a photon energy variable in the range 8–120 eV, polarizations from horizontal (p) and vertical (s) to circular of various kinds, as well as a beam spot of a minimal size of 50 μm.

The APE endstation consists of several interconnected vacuum chambers. Each chamber is dedicated to a few of preparation or characterization methods, the sample on a simple molybdenum/tungsten holder being transferred by a series of wobble sticks and ultrahigh-vacuum monorail trains. Sample mobility reflects in the inability of

accurate temperature measurements, for no connection to it can be made by thermocouple wires. In our experiments we relied on a precision pyrometer for high temperature measurements (>1000 K), and for cryogenic temperatures diodes attached to the cryostat head at the manipulator of the ARPES chamber.

Another misfortune with such an approach of sample handling was a slight tilt present in some of the ARPES measurements due to imperfect positioning of the sample holder at the manipulator. The problem could be partially lessened by appreciable azimuthal rotation of the sample (60° or 120°), transforming most of the tilt to an offset in the polar angle. The tilt itself was checked by LEED.

The electron analyzer at the APE endstation is Scienta SES2002 (hemispherical, mean radius of 200 mm). An estimate of its resolution, including those of the photon beam and thermal broadening, was set to 6 meV. The resolution in our measurements might have been a bit worse, though, due to higher pass energy and higher temperature.

Even at this setup we encountered a problem of uncalibrated angular dispersion. Assuming its linearity, a scale factor of about 10% had to be applied to the spectra to match the true dispersion of graphene's bands. The calibration was dependent on the pass energy used.

NSLS, Brookhaven National Laboratory, New York/USA

National Synchrotron Light Source (NSLS) of Brookhaven National Laboratory (BNL) is a second generation facility. For current standards the synchrotron has pretty low electron beam decay time, needing refills every 2-3 hours. Its U13UB beamline, where we have conducted our experiments, is a source of ultraviolet light of energies variable between 18 and 30 eV, beam spot diameter being of the order of 100 μm. The beamline consists of a magnetically shielded ultrahigh vacuum chamber equipped with standard surface science equipment and an electron analyzer Scienta SES200 of high nominal resolution of 1 meV and 0.1°. Heating of the sample is provided at the sample holder attached to the manipulator by a backside electron bombardment, temperature measurements being done with C type thermocouple wires. Cooling is enabled by means of a cryostat mounted in the core of differentially pumped rotatable manipulator. During our measurements, the base pressure couldn't have been made lower than $3 \cdot 10^{-7}$ Pa, residual gases consisting mostly of methane and molecular hydrogen.

A peculiarity of this setup is that the angle-resolving direction of the analyzer is turned perpendicular to the direction of polar angle rotation of the manipulator, acquiring electrons with respect to so-called tilt angle at a certain polar angle set at the manipulator. This arrangement enables then a continuous mapping of a stripe of the

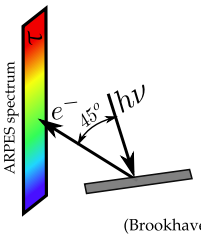

(Brookhaven)

Brillouin zone, that has an angular width of $\pm 6°$ at all possible polar angles.

The sample itself was slightly tilted, and incidentally set to an azimuth differing from the Γ-K-M direction by ~4°; these both could have been later programmatically corrected because of the continuous zone mapping. Individual $I(E_{kin}, \tau)$ spectra at discrete polar angles φ were first transformed to the dependence on momentum, then assembled into $I(E_{kin}, k_{||})$ maps, rotated in the 2D momentum plane to make the Γ-K-M direction coincide with the k_x axis, and finally cut at required planes of constant k_x, k_y or E value. In scanning the zone the relative polar angles were varied in steps of 0.5° or 1.0°, as read off from a vernier scale of a precision of 0.1°.

A note should be made here that the light at the beamline is strictly p polarized only for the electrons emerging at the zero tilt angles ($\tau = 0°$, any φ), other tilt angles having polarization unclassified in the theory of ARPES.

B

ITERATIVE EXTRACTION OF THE BARE BAND

Following the considerations of Chapter 5, we present here IGOR Pro[1] implementation of our iterative self-consistent procedure for extracting the bare band and both parts of the self energy from ARPES profiles of renormalized electronic bands. We first show how to prepare the input data from the analysis of MDC peak positions and linewidths, then discuss the code, and finally examine its output over the course of iterations.

INPUT DATA

As an input to the self-consistent iterative procedure two IGOR Pro waves are used. The wave named `km` contains the peak positions of MDCs obtained by cutting the analyzed spectrum on a set of evenly spaced energies, while `fwhm` provides their full widths at half maximum. Both are the result of fitting of MDCs to a Lorentzian lineshape.

IGOR Pro file `km.itx` contains the experimental dispersion, i. e. maxima of the spectral function at a given energy. For the presentation purposes, the wave is here downsampled to $\Delta = 0.012$ eV from $\Delta = 0.005$ eV used in the actual analysis. The x axis has been properly scaled, placing the position of the Fermi level to 0 eV.

```
IGOR
WAVES    km
BEGIN
    1.797    1.799    1.801    1.804    1.806
    1.809    1.812    1.814    1.817    1.819
    1.822    1.824    1.827    1.830    1.834
    1.836    1.838    1.841    1.844    1.846
    1.849    1.852    1.854    1.857    1.859
    1.862    1.864    1.867    1.870    1.872
    1.875    1.878    1.880    1.883    1.886
    1.889    1.891    1.893    1.895    1.898
    1.900    1.903    1.905    1.907    1.910
    1.913    1.918    1.922    1.927    1.932
    1.936    1.940    1.944    1.947    1.951
    1.955    1.959    1.963    1.968    1.971
    1.975
END
X SetScale/P x -0.7,0.012,"eV", km
X SetScale y 0,0,"1/A", km
```

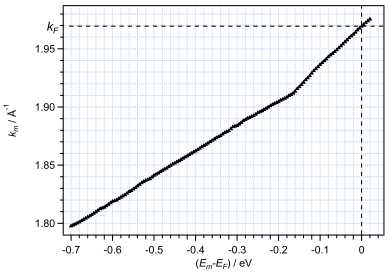

1 IGOR Pro (WaveMetrics Inc., USA) is an interactive software environment for experimentation with scientific and engineering data.

IgorPro file `fwhm.itx` contains the widths of Lorentzian peaks at a given energy. For the presentation purposes, the wave is here downsampled to $\Delta = 0.012$ eV from $\Delta = 0.005$ eV used in the actual analysis. The x axis has been properly scaled, placing the position of the Fermi level to 0 eV.

```
IGOR
WAVES    fwhm
BEGIN
    0.0464    0.0458    0.0453    0.0434    0.0430
    0.0445    0.0435    0.0442    0.0423    0.0414
    0.0420    0.0407    0.0418    0.0419    0.0415
    0.0405    0.0414    0.0420    0.0416    0.0408
    0.0398    0.0390    0.0400    0.0405    0.0408
    0.0397    0.0398    0.0399    0.0403    0.0405
    0.0408    0.0408    0.0413    0.0406    0.0399
    0.0419    0.0421    0.0411    0.0415    0.0418
    0.0433    0.0436    0.0428    0.0382    0.0361
    0.0315    0.0290    0.0282    0.0273    0.0279
    0.0278    0.0262    0.0243    0.0233    0.0230
    0.0228    0.0224    0.0245    0.0247    0.0246
    0.0222
END
X SetScale/P x -0.7,0.012,"eV", fwhm
X SetScale y 0,0,"1/A", fwhm
```

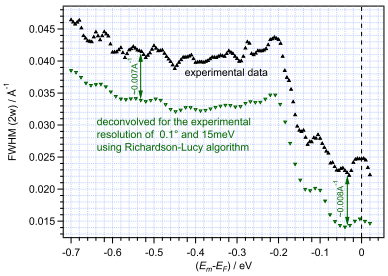

CODE

The first of procedures, `scKK_setup`, is used for initialization, with properly scaled one-dimensional waves containing data on the peak positions (`km`) and widths (`fwhm`) of MDC Lorentzians. It produces waves that will be used in the other procedure for the actual calculation. These serve to hold either the final results (`scEb`, `scEb_fit`, `scReS`, `scImS`) or some intermediate data.

```
Function scKK_setup(km,fwhm)
    Wave km,fwhm
// (km-kF) as a function of Em:
    Duplicate/O km,scKKm
// putting the origin of the k axis to kF (the point where Em=0):
    Variable kF=km(0);  scKKm=km-kF
    Duplicate/O fwhm,hwhm;  hwhm*=0.5
// sample ReS and Eb(Em) at the same energies as KKm:
    Duplicate/O scKKm,scReS
// sample ImS at the same energies as hwhm:
    Duplicate/O hwhm,scImS
// discrete bare band Eb; Em(km); and an auxiliary wave:
    Make/O/N=(numpnts(scKKm)) scEb,scEm,Em_scaling
// scaling from the first/last k-point of the experimental dispersion:
    SetScale/I x,scKKm[0],scKKm[numpnts(scKKm)], "A\S-1\M",scEb, scEm
    SetScale  y,0,0,"eV",scEb,scEm
// functional (i.e. smooth) form of the bare band:
    Duplicate/O scEb,scEb_fit
// this will be used in the interpolation to get Em(km) from km(Em):
    SetScale/I x,leftx(scKKm),leftx(scKKm)+deltax(scKKm)*(numpnts(scKKm)-1),Em_scaling
    Em_scaling=x
// Em as a function of (km-kF):
    scEm=interp(x,scKKm,Em_scaling)
// zeroth approximation to Eb: a line through (kF,EF)=(0,0) and the lowest point of the experimental
      dispersion
    Make/O cw={0,leftx(scKKm)/scKKm[0]}
    scEb=poly(cw,x)
// this will become symmetrized and resampled ImS:
    Make/O/N=(4*numpnts(scImS)) symmImS // double the data, double the resolution
    SetScale/I x,leftx(scImS),-leftx(scImS),"eV",symmImS
// this will become symmetrized and resampled ReS:
    Make/O/N=(4*numpnts(scReS)) symmReS // double the data, double the resolution
    SetScale/I x,leftx(scReS),-leftx(scReS),"eV",symmReS
End
```

Next, the procedure `scKK_iteration` is invoked for several times, until the convergence in the output waves is achieved.

The result of the procedure are the coefficients `cw` defining the bare band polynomial of order `polyN`. The polynomial is immediately calculated in the wave `scEb_fit`, but only in the range of momenta covered by the input waves. Non-smoothed bare band obtained in step 3 of the algorithm (cf. Figure 31) is contained in `scEb`. The waves `scReS` and `scImS` hold the self-consistent data for $\Re\mathfrak{e}\Sigma$ and $\Im\mathrm{m}\Sigma$ that were calculated from `km` and `fwhm` by the defining equations 5.2 and 5.3. Two related waves, `scHReS` and `scHImS`, are obtained as Kramers-Kronig transforms of `scImS` and `scReS`, respectively: `scHReS` = Kramers-Kronig(`scImS`), `scHImS` = Kramers-Kronig(`scReS`). The convergence of the procedure is monitored by comparing `scImS` with `scHImS`, `scReS` with `scHReS`, or by watching the changes in `scEb_fit` from one iteration to the other. The latter can be readily compared to `scEm` (which is just the inverse of the measured dispersion `km`) and `scEb`.

```
Function scKK_iteration(polyN)
    Variable polyN
    Wave scKKm, scEb, scReS, scImS
// some auxiliary waves:
    Wave scEm, hwhm, cw, symmReS, symmImS

// start from ImS:
    //scImS=poly(cw,scKKm(x)) - poly(cw,scKKm(x)-hwhm(x))
    // or
    scImS=poly(cw,scKKm(x)+hwhm(x)) - poly(cw,scKKm(x))
    // or
    //scImS=0.5*(poly(cw,scKKm(x)+hwhm(x)) - poly(cw,scKKm(x)-hwhm(x)))

//  ----- Kramers-Kronig transform of ImS to HReS
// symmetrize for HilbertTransform:
    symmImS=(x<=0) ? scImS(x) : scImS(-x)
// ReS from the K-K transform of ImS:
    HilbertTransform/DEST=scHReS symmImS
    scHReS*=-1
    SetScale/P x,leftx(symmImS),deltax(symmImS),"eV",scHReS

// ----- ansatz for Eb in the next iteration
// bare band as a function of km (thus of all the discrete k's present in the spectrum):
    scEb=scEm(x)-scHreS(scEm(x))

// ----- fit Eb to a polynomial (could be any other function), as we need some extrapolation
// initial values of the fitting polynomial coefficients: all 0
    Make/O/N=(polyN+1) cw=0
    String fmtStr
// keep c0=0, i.e. make the polynomial zero at (kF,EF)=(0,0):
    sprintf fmtStr,"1%0*.0f" polyN, 0;
// the output of this cmd will be used for the next iteration:
    CurveFit/Q/H=fmtstr/NTHR=1 poly (polyN+1), kwCWave=cw, scEb /D=scEb_fit
// print fitting coefficients:
    print cw

// ----- and just to check things out
// ReS from the very definition; poly(...) represents a smooth Eb function from this iteration:
    scReS=x - poly(cw,scKKm(x))
// antisymmetrize:
    symmReS=(x<=0) ? scReS(x) : (-scReS(-x))
// ImS from the K-K transform of ReS:
    HilbertTransform/DEST=scHImS symmReS
    SetScale/P x,leftx(symmReS),deltax(symmReS),"eV",scHImS
// offset, as HilbertTransform makes mean=0:
    scHImS+=mean(scImS)
End
```

As the point (k_F,E_F) can be read off the spectrum with high enough accuracy, it convenient to put (k_F,E_F)=(0,0) and make the bare band function pass through it. Instead of a polynomial, any fitting function (e. g. a tight-binding formula) should be easy to implement.

Calculating the spectral function `scAm` from the self-consistent data

```
Function scKK_A()
    Wave scReS,scImS,scEb_fit,scKKm
    Duplicate/O scKKm,scAm
    scAm=scImS(x) / ( ( x-scEb_fit(scKKm(x))-scReS(x) )^2 + ( scImS(x) )^2 )
End
```

CONVERGENCE

The figure below shows the convergence of the bare-band function. The iteration starts by postulating a linear band (i_o). Already the second iteration (i_2) gives a band indistinguishable from those obtained in further iterations. Also shown is how the coefficients of a third-order polynomial for E_b

$$E_b(k) = 0 + c_1 k + c_2 k^2 + c_3 k^3$$

converge oscillatory through the course of iterations.

Note that the renormalized and the bare-band merge in the very vicinity of the kink, giving confidence that the influence of the missing low energy tail of the measured band is negligible.

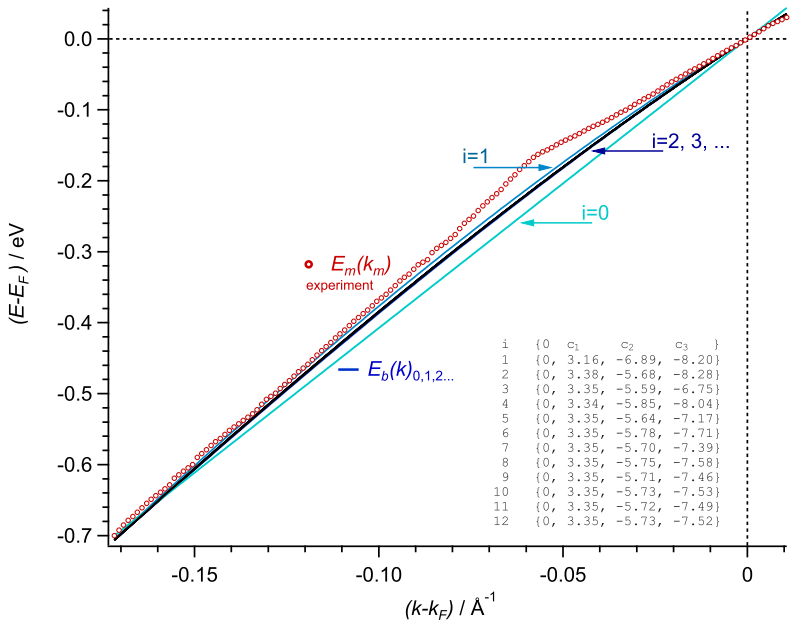

BIBLIOGRAPHY

[1] T. Land, T. Michely, R. Behm, J. Hemminger, and G. Comsa. STM investigation of single layer graphite structures produced on Pt(111) by hydrocarbon decomposition. *Surface Science*, 264(3):261–270, March 1992, doi:10.1016/0039-6028(92)90183-7. (Cited on page 1.)

[2] C. Oshima and A. Nagashima. Ultra-thin epitaxial films of graphite and hexagonal boron nitride on solid surfaces. *Journal of Physics: Condensed Matter*, 9(1):1–20, January 1997, doi:10.1088/0953-8984/9/1/004. (Cited on page 1.)

[3] X. Lu, M. Yu, H. Huang, and R. S. Ruoff. Tailoring graphite with the goal of achieving single sheets. *Nanotechnology*, 10(3):269–272, September 1999, doi:10.1088/0957-4484/10/3/308. (Cited on pages 1 and 12.)

[4] P. R. Wallace. Band theory of graphite. *Physical Review*, 71(9):622, 1947. (Cited on page 1.)

[5] G. Semenoff. Condensed-Matter Simulation of a Three-Dimensional Anomaly. *Physical Review Letters*, 53(26):2449, December 1984, doi:10.1103/PhysRevLett.53.2449. (Cited on page 1.)

[6] D. P. DiVincenzo and E. J. Mele. Self-consistent effective-mass theory for intralayer screening in graphite intercalation compounds. *Physical Review B*, 29(4):1685–1694, February 1984, doi:10.1103/PhysRevB.29.1685. (Cited on page 1.)

[7] H.-P. Boehm, R. Setton, and E. Stumpp. Nomenclature and terminology of graphite intercalation compounds (IUPAC Recommendations 1994). *Pure and Applied Chemistry*, 66(9):1893–1901, 1994, doi:10.1351/pac199466091893. (Cited on page 1.)

[8] K. S. Novoselov, A. K. Geim, S. V. Morozov, D. Jiang, Y. Zhang, S. V. Dubonos, I. V. Grigorieva, and A. A. Firsov. Electric field effect in atomically thin carbon films. *Science (New York, N.Y.)*, 306(5696):666–9, October 2004, doi:10.1126/science.1102896. (Cited on pages 1 and 12.)

[9] K. S. Novoselov, D. Jiang, F. Schedin, T. J. Booth, V. V. Khotkevich, S. V. Morozov, and A. K. Geim. Two-dimensional atomic crystals. *Proceedings of the National Academy of Sciences of the United States of America*, 102(30):10451–3, July 2005, doi:10.1073/pnas.0502848102. (Cited on pages 1 and 12.)

[10] K. S. Novoselov, a. K. Geim, S. V. Morozov, D. Jiang, M. I. Katsnelson, I. V. Grigorieva, S. V. Dubonos, and A. A. Firsov. Two-dimensional gas of massless Dirac fermions in graphene. *Nature*, 438(7065):197–200, November 2005, doi:10.1038/nature04233. (Cited on page 1.)

[11] Y. Zhang, Y.-W. Tan, H. L. Stormer, and P. Kim. Experimental observation of the quantum Hall effect and Berry's phase in graphene. *Nature*, 438(7065):201–4, November 2005, doi:10.1038/nature04235. (Cited on page 1.)

[12] D. Abergel, V. Apalkov, J. Berashevich, K. Ziegler, and T. Chakraborty. Properties of graphene: a theoretical perspective. *Advances in Physics*, 59(4):261–482, July 2010, doi:10.1080/00018732.2010.487978. (Cited on page 9.)

[13] C. Beenakker. Colloquium: Andreev reflection and Klein tunneling in graphene. *Reviews of Modern Physics*, 80(4):1337–1354, October 2008, doi:10.1103/RevModPhys.80.1337. (Cited on page 9.)

[14] C. Bena and G. Montambaux. Remarks on the tight-binding model of graphene. *New Journal of Physics*, 11(9):095003, September 2009, doi:10.1088/1367-2630/11/9/095003. (Cited on page 9.)

[15] A. Geim and A. MacDonald. Graphene: Exploring carbon flatland. *Physics Today*, 60(8), 2007. (Cited on page 9.)

[16] M. Katsnelson. Graphene: carbon in two dimensions. *Materials today*, 10(1-2):20–27, 2007. (Cited on pages 9 and 10.)

[17] C. Berger, Z. Song, X. Li, X. Wu, N. Brown, C. Naud, D. Mayou, T. Li, J. Hass, A. N. Marchenkov, E. H. Conrad, P. N. First, and W. A. de Heer. Electronic confinement and coherence in patterned epitaxial graphene. *Science (New York, N.Y.)*, 312(5777):1191–6, May 2006, doi:10.1126/science.1125925. (Cited on pages 12 and 13.)

[18] J. Hass, W. A. de Heer, and E. H. Conrad. The growth and morphology of epitaxial multilayer graphene. *Journal of Physics: Condensed Matter*, 20(32):323202, August 2008, doi:10.1088/0953-8984/20/32/323202. (Cited on page 12.)

[19] W. A. de Heer, C. Berger, X. Wu, P. First, E. Conrad, X. Li, T. Li, M. Sprinkle, J. Hass, and M. Sadowski. Epitaxial graphene. *Solid State Communications*, 143(1-2):92–100, July 2007, doi:10.1016/j.ssc.2007.04.023. (Cited on page 12.)

[20] K. V. Emtsev, A. Bostwick, K. Horn, J. Jobst, G. L. Kellogg, L. Ley, J. L. McChesney, T. Ohta, S. A. Reshanov, J. Röhrl,

E. Rotenberg, A. K. Schmid, D. Waldmann, H. B. Weber, and T. Seyller. Towards wafer-size graphene layers by atmospheric pressure graphitization of silicon carbide. *Nature materials*, 8(3):203–7, March 2009, doi:10.1038/nmat2382. (Cited on page 12.)

[21] F. Varchon, R. Feng, J. Hass, X. Li, B. Nguyen, C. Naud, P. Mallet, J.-Y. Veuillen, C. Berger, E. Conrad, and L. Magaud. Electronic Structure of Epitaxial Graphene Layers on SiC: Effect of the Substrate. *Physical Review Letters*, 99(12):126805, September 2007, doi:10.1103/PhysRevLett.99.126805. (Cited on page 12.)

[22] J. Hass, F. Varchon, J. Millán-Otoya, M. Sprinkle, N. Sharma, W. de Heer, C. Berger, P. First, L. Magaud, and E. Conrad. Why Multilayer Graphene on 4H-SiC(0001) Behaves Like a Single Sheet of Graphene. *Physical Review Letters*, 100(12):125504, March 2008, doi:10.1103/PhysRevLett.100.125504. (Cited on page 13.)

[23] J. Wintterlin and M.-L. Bocquet. Graphene on metal surfaces. *Surface Science*, 603(10-12):1841–1852, June 2009, doi:10.1016/j.susc.2008.08.037. (Cited on pages 13 and 14.)

[24] A. Varykhalov, J. Sánchez-Barriga, A. Shikin, C. Biswas, E. Vescovo, A. Rybkin, D. Marchenko, and O. Rader. Electronic and Magnetic Properties of Quasifreestanding Graphene on Ni. *Physical Review Letters*, 101(15):157601, October 2008, doi:10.1103/PhysRevLett.101.157601. (Cited on pages 14 and 32.)

[25] T. Brugger, S. Günther, B. Wang, J. H. Dil, M.-L. Bocquet, J. Osterwalder, J. Wintterlin, and T. Greber. Comparison of electronic structure and template function of single-layer graphene and a hexagonal boron nitride nanomesh on Ru(0001). *Physical Review B*, 79(4):045407, January 2009, doi:10.1103/PhysRevB.79.045407. (Cited on pages 14 and 32.)

[26] P. Sutter, J. T. Sadowski, and E. Sutter. Graphene on Pt(111): Growth and substrate interaction. *Physical Review B*, 80(24):1–10, December 2009, doi:10.1103/PhysRevB.80.245411. (Cited on page 14.)

[27] C. Busse, P. Lazić, R. Djemour, J. Coraux, T. Gerber, N. Atodiresei, V. Caciuc, R. Brako, A. N'Diaye, S. Blügel, J. Zegenhagen, and T. Michely. Graphene on Ir(111): Physisorption with Chemical Modulation. *Physical Review Letters*, 107(3):036101, July 2011, doi:10.1103/PhysRevLett.107.036101. (Cited on page 14.)

[28] S. Marchini, S. Günther, and J. Wintterlin. Scanning tunneling microscopy of graphene on Ru(0001). *Physical Review B*, 76(7):075429, August 2007, doi:10.1103/PhysRevB.76.075429. (Cited on pages 14 and 60.)

[29] H. Hattab, A. T. N'Diaye, D. Wall, G. Jnawali, J. Coraux, C. Busse, R. van Gastel, B. Poelsema, T. Michely, F.-J. Meyer zu Heringdorf, and M. Horn-von Hoegen. Growth temperature dependent graphene alignment on Ir(111). *Applied Physics Letters*, 98(14):141903, April 2011, doi:10.1063/1.3548546. (Cited on page 14.)

[30] J. Coraux, A. T. N'Diaye, C. Busse, and T. Michely. Structural coherency of graphene on Ir(111). *Nano letters*, 8(2):565–70, February 2008, doi:10.1021/nl0728874. (Cited on pages 14, 18, 19, 21, and 32.)

[31] E. Loginova, N. C. Bartelt, P. J. Feibelman, and K. F. McCarty. Factors influencing graphene growth on metal surfaces. *New Journal of Physics*, 11(6):063046, June 2009, doi:10.1088/1367-2630/11/6/063046. (Cited on page 14.)

[32] E. Loginova, S. Nie, K. Thürmer, N. Bartelt, and K. McCarty. Defects of graphene on Ir(111): Rotational domains and ridges. *Physical Review B*, 80(8):085430, August 2009, doi:10.1103/PhysRevB.80.085430. (Cited on pages 14 and 21.)

[33] E. Starodub, A. Bostwick, L. Moreschini, S. Nie, F. Gabaly, K. McCarty, and E. Rotenberg. In-plane orientation effects on the electronic structure, stability, and Raman scattering of monolayer graphene on Ir(111). *Physical Review B*, 83(12):125428, March 2011, doi:10.1103/PhysRevB.83.125428. (Cited on pages 14, 21, 32, and 41.)

[34] A. T. N'Diaye, J. Coraux, T. N. Plasa, C. Busse, and T. Michely. Structure of epitaxial graphene on Ir(111). *New Journal of Physics*, 10(4):043033, April 2008, doi:10.1088/1367-2630/10/4/043033. (Cited on pages 15, 22, and 36.)

[35] R. van Gastel, A. T. N'Diaye, D. Wall, J. Coraux, C. Busse, N. M. Buckanie, F.-J. Meyer zu Heringdorf, M. Horn von Hoegen, T. Michely, and B. Poelsema. Selecting a single orientation for millimeter sized graphene sheets. *Applied Physics Letters*, 95(12):121901, 2009, doi:10.1063/1.3225554. (Cited on page 15.)

[36] A. N'Diaye. private communication, 2008-2009. (Cited on pages 16 and 18.)

[37] A. T. N'Diaye, R. V. Gastel, A. J. Martínez-Galera, J. Coraux, H. Hattab, D. Wall, F.-J. M. Z. Heringdorf, M. H.-v. Hoegen, J. M. Gómez-Rodríguez, B. Poelsema, C. Busse, and T. Michely. In situ observation of stress relaxation in epitaxial graphene. *New Journal of Physics*, 11(11):113056, November 2009, doi:10.1088/1367-2630/11/11/113056. (Cited on page 21.)

[38] J. van der Veen, F. Himpsel, and D. Eastman. Experimental energy dispersions for valence and conduction bands of iridium. *Physical Review B*, 22(9):4226–4233, November 1980, doi:10.1103/PhysRevB.22.4226. (Cited on pages 24 and 25.)

[39] N. Müller, B. Kessler, B. Schmiedeskamp, G. Schönhense, and U. Heinzmann. Spin-resolved photoemission from Ir(111): Transitions into a secondary band and energetic position of the final state bands. *Solid State Communications*, 61(3):187–192, January 1987, doi:10.1016/0038-1098(87)90027-5. (Cited on page 24.)

[40] E. Tamura, W. Piepke, and R. Feder. Spin-resolved photoemission from (111) surfaces of Pd, Ir and Pt by circularly polarised light: theory and comparison with experiment. *Journal of Physics: Condensed Matter*, 1(36):6469–6482, September 1989, doi:10.1088/0953-8984/1/36/015. (Cited on page 24.)

[41] J. Noffke and L. Fritsche. Band structure calculation and photoemission analysis of iridium. *Journal of Physics F: Metal Physics*, 12(5):921–933, May 1982, doi:10.1088/0305-4608/12/5/011. (Cited on pages 24 and 25.)

[42] I. Pletikosić, M. Kralj, D. Šokčević, R. Brako, P. Lazić, and P. Pervan. Photoemission and density functional theory study of Ir(111); energy band gap mapping. *Journal of physics. Condensed matter : an Institute of Physics journal*, 22(13):135006, April 2010, doi:10.1088/0953-8984/22/13/135006. (Cited on pages 25, 27, 32, and 51.)

[43] A. Varykhalov, D. Marchenko, M. Scholz, E. Rienks, T. Kim, G. Bihlmayer, J. Sánchez-Barriga, and O. Rader. Ir(111) Surface State with Giant Rashba Splitting Persists under Graphene in Air. *Physical Review Letters*, 108(6):066804, February 2012, doi:10.1103/PhysRevLett.108.066804. (Cited on page 25.)

[44] R. Brako. private communication, 2008-2010. (Cited on pages 29, 30, and 43.)

[45] P. Feibelman. Pinning of graphene to Ir(111) by flat Ir dots. *Physical Review B*, 77(16):165419, April 2008, doi:10.1103/PhysRevB.77.165419. (Cited on page 32.)

[46] A. N'Diaye, S. Bleikamp, P. Feibelman, and T. Michely. Two-Dimensional Ir Cluster Lattice on a Graphene Moiré on Ir(111). *Physical Review Letters*, 97(21):215501, November 2006, doi:10.1103/PhysRevLett.97.215501. (Cited on page 32.)

[47] J. Sánchez-Barriga, A. Varykhalov, D. Marchenko, M. R. Scholz, and O. Rader. Minigap isotropy and broken chirality in graphene with periodic corrugation enhanced by cluster superlattices. *Physical Review B*, 85(20):201413, 2012, doi:10.1103/PhysRevB.85.201413. (Cited on pages 32 and 41.)

[48] H. Daimon, S. Imada, H. Nishimoto, and S. Suga. Structure factor in photoemission from valence band. *Journal of electron spectroscopy and related phenomena*, 76:487–492, 1995. (Cited on page 32.)

[49] E. Shirley, L. Terminello, A. Santoni, and F. Himpsel. Brillouin-zone-selection effects in graphite photoelectron angular distributions. *Physical Review B*, 51(19):13614, 1995. (Cited on pages 32 and 33.)

[50] M. Mucha-Kruczynski, O. Tsyplyatyev, A. Grishin, E. McCann, V. Fal'ko, A. Bostwick, and E. Rotenberg. Characterization of graphene through anisotropy of constant-energy maps in angle-resolved photoemission. *Physical Review B*, 77(19):195403, May 2008, doi:10.1103/PhysRevB.77.195403. (Cited on page 33.)

[51] A. Bostwick, T. Ohta, J. L. McChesney, K. V. Emtsev, T. Seyller, K. Horn, and E. Rotenberg. Symmetry breaking in few layer graphene films. *New Journal of Physics*, 9(10):385, October 2007, doi:10.1088/1367-2630/9/10/385. (Cited on pages 33, 38, and 60.)

[52] I. Gierz, J. Henk, H. Höchst, C. Ast, and K. Kern. Illuminating the dark corridor in graphene: Polarization dependence of angle-resolved photoemission spectroscopy on graphene. *Physical Review B*, 83(12):121408, March 2011, doi:10.1103/PhysRevB.83.121408. (Cited on pages 33 and 50.)

[53] Y. Liu, G. Bian, T. Miller, and T.-C. Chiang. Visualizing Electronic Chirality and Berry Phases in Graphene Systems Using Photoemission with Circularly Polarized Light. *Physical Review Letters*, 107(16):166803, October 2011, doi:10.1103/PhysRevLett.107.166803. (Cited on page 33.)

[54] C. Hwang, C.-H. Park, D. Siegel, A. Fedorov, S. Louie, and A. Lanzara. Direct measurement of quantum phases in graphene via photoemission spectroscopy. *Physical Review B*, 84(12):125422, September 2011, arXiv:1109.3680, doi:10.1103/PhysRevB.84.125422. (Cited on page 33.)

[55] M. Sprinkle, D. Siegel, Y. Hu, J. Hicks, A. Tejeda, A. Taleb-Ibrahimi, P. Le Fèvre, F. Bertran, S. Vizzini, H. Enriquez, S. Chiang, P. Soukiassian, C. Berger, W. a. de Heer, A. Lanzara, and E. H. Conrad. First Direct Observation of a Nearly Ideal Graphene Band Structure. *Physical Review Letters*, 103(22):226803, November 2009, doi:10.1103/PhysRevLett.103.226803. (Cited on pages 35 and 55.)

[56] G. Giovannetti, P. Khomyakov, G. Brocks, V. Karpan, J. van den Brink, and P. Kelly. Doping Graphene with Metal Contacts. *Physical Review Letters*, 101(2):026803, July 2008, doi:10.1103/PhysRevLett.101.026803. (Cited on page 35.)

[57] S. Rusponi, M. Papagno, P. Moras, S. Vlaic, M. Etzkorn, P. Sheverdyaeva, D. Pacilé, H. Brune, and C. Carbone. Highly Anisotropic Dirac Cones in Epitaxial Graphene Modulated by an Island Superlattice. *Physical Review Letters*, 105(24):246803, December 2010, doi:10.1103/PhysRevLett.105.246803. (Cited on page 35.)

[58] S. Reich, J. Maultzsch, C. Thomsen, and P. Ordejón. Tight-binding description of graphene. *Physical Review B*, 66(3):035412, July 2002, doi:10.1103/PhysRevB.66.035412. (Cited on pages 37 and 42.)

[59] G. M. Rutter, J. N. Crain, N. P. Guisinger, T. Li, P. N. First, and J. a. Stroscio. Scattering and interference in epitaxial graphene. *Science (New York, N.Y.)*, 317(5835):219–22, July 2007, doi:10.1126/science.1142882. (Cited on pages 38 and 60.)

[60] F. Varchon, P. Mallet, J.-Y. Veuillen, and L. Magaud. Ripples in epitaxial graphene on the Si-terminated SiC(0001) surface. *Physical Review B*, 77(23):235412, June 2008, doi:10.1103/PhysRevB.77.235412. (Cited on pages 38 and 60.)

[61] S. Zhou, D. Siegel, A. Fedorov, and A. Lanzara. Departure from the conical dispersion in epitaxial graphene. *Physica E: Low-dimensional Systems and Nanostructures*, 40(7):2642–2647, May 2008, doi:10.1016/j.physe.2007.10.121. (Cited on pages 38 and 60.)

[62] T. Ohta, A. Bostwick, T. Seyller, K. Horn, and E. Rotenberg. Controlling the electronic structure of bilayer graphene. *Science (New York, N.Y.)*, 313(5789):951–4, August 2006, doi:10.1126/science.1130681. (Cited on pages 38 and 60.)

[63] C.-H. Park, L. Yang, Y.-W. Son, M. L. Cohen, and S. G. Louie. Anisotropic behaviours of massless Dirac fermions in graphene under periodic potentials. *Nature Physics*, 4(3):213–217, February 2008, doi:10.1038/nphys890. (Cited on pages 41 and 42.)

[64] I. Pletikosić, M. Kralj, P. Pervan, R. Brako, J. Coraux, A. N'Diaye, C. Busse, and T. Michely. Dirac Cones and Minigaps for Graphene on Ir(111). *Physical Review Letters*, 102(5):056808, February 2009, doi:10.1103/PhysRevLett.102.056808. (Cited on pages 41, 45, and 50.)

[65] M. Kralj, I. Pletikosić, M. Petrović, P. Pervan, M. Milun, A. N'Diaye, C. Busse, T. Michely, J. Fujii, and I. Vobornik. Graphene on Ir(111) characterized by angle-resolved photoemission. *Physical Review B*, 84(7):075427, August 2011, doi:10.1103/PhysRevB.84.075427. (Cited on pages 42, 45, 51, and 53.)

[66] J. L. McChesney, A. Bostwick, T. Ohta, T. Seyller, K. Horn, J. González, and E. Rotenberg. Extended van Hove Singularity and Superconducting Instability in Doped Graphene. *Physical Review Letters*, 104(13):136803, April 2010, doi:10.1103/PhysRevLett.104.136803. (Cited on pages 44 and 50.)

[67] A. Bostwick, T. Ohta, T. Seyller, K. Horn, and E. Rotenberg. Quasiparticle dynamics in graphene. *Nature Physics*, 3(1):36–40, December 2007, doi:10.1038/nphys477. (Cited on pages 44, 51, and 55.)

[68] A. Bostwick, F. Speck, T. Seyller, K. Horn, M. Polini, R. Asgari, A. H. MacDonald, and E. Rotenberg. Observation of plasmarons in quasi-freestanding doped graphene. *Science (New York, N.Y.)*, 328(5981):999–1002, May 2010, doi:10.1126/science.1186489. (Cited on page 44.)

[69] D. A. Siegel, C.-H. Park, C. Hwang, J. Deslippe, A. V. Fedorov, S. G. Louie, and A. Lanzara. Many-body interactions in quasi-freestanding graphene. *Proceedings of the National Academy of Sciences of the United States of America*, 108(28):11365–9, July 2011, doi:10.1073/pnas.1100242108. (Cited on pages 44 and 53.)

[70] S. Das Sarma, E. Hwang, and W.-K. Tse. Many-body interaction effects in doped and undoped graphene: Fermi liquid versus non-Fermi liquid. *Physical Review B*, 75(12):121406, March 2007, doi:10.1103/PhysRevB.75.121406. (Cited on page 44.)

[71] K. F. Mak, J. Shan, and T. Heinz. Seeing Many-Body Effects in Single- and Few-Layer Graphene: Observation of Two-Dimensional Saddle-Point Excitons. *Physical Review Letters*, 106(4):046401, January 2011, doi:10.1103/PhysRevLett.106.046401. (Cited on page 44.)

[72] C.-H. Park, F. Giustino, M. L. Cohen, and S. G. Louie. Electron-phonon interactions in graphene, bilayer graphene, and graphite. *Nano letters*, 8(12):4229–33, December 2008, doi:10.1021/nl801884n. (Cited on page 44.)

[73] A. Grüneis, C. Attaccalite, A. Rubio, D. Vyalikh, S. Molodtsov, J. Fink, R. Follath, W. Eberhardt, B. Büchner, and T. Pichler. Electronic structure and electron-phonon coupling of doped graphene layers in KC8. *Physical Review B*, 79(20):205106, May 2009, doi:10.1103/PhysRevB.79.205106. (Cited on pages 44, 45, 50, and 55.)

[74] T. Valla, J. Camacho, Z.-H. Pan, A. Fedorov, A. Walters, C. Howard, and M. Ellerby. Anisotropic Electron-Phonon Coupling and Dynamical Nesting on the Graphene Sheets in Superconducting CaC6 using Angle-Resolved Photoemission Spectroscopy. *Physical Review Letters*, 102(10):107007, March 2009, doi:10.1103/PhysRevLett.102.107007. (Cited on pages 44, 50, and 57.)

[75] K. M. Borysenko, J. T. Mullen, E. A. Barry, S. Paul, Y. G. Semenov, J. M. Zavada, M. B. Nardelli, and K. W. Kim. First-principles analysis of electron-phonon interactions in graphene. *Physical Review B*, 81(12):121412, March 2010, doi:10.1103/PhysRevB.81.121412. (Cited on page 44.)

[76] M. Bianchi, E. D. L. Rienks, S. Lizzit, A. Baraldi, R. Balog, L. Hornekaer, and P. Hofmann. Electron-phonon coupling in potassium-doped graphene: Angle-resolved photoemission spectroscopy. *Physical Review B*, 81(4):041403, January 2010, doi:10.1103/PhysRevB.81.041403. (Cited on pages 44, 45, 48, 50, 51, 53, 56, and 57.)

[77] S. Zhou, D. Siegel, A. Fedorov, and A. Lanzara. Kohn anomaly and interplay of electron-electron and electron-phonon interactions in epitaxial graphene. *Physical Review B*, 78(19):193404, November 2008, doi:10.1103/PhysRevB.78.193404. (Cited on page 44.)

[78] D. Siegel, C. Hwang, A. Fedorov, and A. Lanzara. Electron-Phonon Coupling in Highly-Screened Graphene. *Arxiv preprint arXiv:1108.2566*, pages 1–5, August 2011, arXiv:1108.2566. (Cited on pages 44, 45, and 57.)

[79] Z.-H. Pan, J. Camacho, M. Upton, A. Fedorov, C. Howard, M. Ellerby, and T. Valla. Electronic Structure of Superconducting KC_{8} and Nonsuperconducting LiC_{6} Graphite Intercalation Compounds: Evidence for a Graphene-Sheet-Driven Superconducting State. *Physical Review Letters*, 106(18):187002, May 2011, doi:10.1103/PhysRevLett.106.187002. (Cited on page 44.)

[80] C.-H. Park, F. Giustino, J. McChesney, A. Bostwick, T. Ohta, E. Rotenberg, M. Cohen, and S. Louie. Van Hove singular-

ity and apparent anisotropy in the electron-phonon interaction in graphene. *Physical Review B*, 77(11):113410, March 2008, doi:10.1103/PhysRevB.77.113410. (Cited on pages 44, 45, and 53.)

[81] P. Hofmann, I. Y. Sklyadneva, E. D. L. Rienks, and E. V. Chulkov. Electron-phonon coupling at surfaces and interfaces. *New Journal of Physics*, 11(12):125005, December 2009, doi:10.1088/1367-2630/11/12/125005. (Cited on pages 45 and 47.)

[82] A. Kordyuk, S. Borisenko, A. Koitzsch, J. Fink, M. Knupfer, and H. Berger. Bare electron dispersion from experiment: Self-consistent self-energy analysis of photoemission data. *Physical Review B*, 71(21):214513, June 2005, doi:10.1103/PhysRevB.71.214513. (Cited on pages 45, 46, 47, 53, and 55.)

[83] C. Veenstra, G. Goodvin, M. Berciu, and A. Damascelli. Spectral function tour of electron-phonon coupling outside the Migdal limit. *Physical Review B*, 84(8):085126, August 2011, doi:10.1103/PhysRevB.84.085126. (Cited on pages 45 and 46.)

[84] A. Tontegode and E. V. Rut'kov. Intercalation by atoms of a two-dimensional graphite film on a metal. *Physics-Uspekhi*, 36(11):1053–1067, 1993. (Cited on page 45.)

[85] A. Kordyuk. Details of the photoemission spectra analysis. *Arxiv preprint cond-mat/0510421*, October 2005, arXiv:0510421. (Cited on page 46.)

[86] M. R. Norman, H. Ding, H. Fretwell, M. Randeria, and J. C. Campuzano. Extraction of the electron self-energy from angle-resolved photoemission data: Application to BiSrCaCuO. *Physical Review B*, 60(10):7585–7590, 1999. (Cited on pages 47 and 48.)

[87] J. McChesney, A. Bostwick, T. Ohta, K. Emtsev, T. Seyller, K. Horn, and E. Rotenberg. Self-consistent analysis of electron-phonon coupling parameters of graphene. *Arxiv preprint arXiv:0809.4046*, page 4, September 2008, arXiv:0809.4046. (Cited on pages 47, 55, and 56.)

[88] J. Fink, A. Koitzsch, J. Geck, V. Zabolotnyy, M. Knupfer, B. Büchner, A. Chubukov, and H. Berger. Reevaluation of the coupling to a bosonic mode of the charge carriers in (Bi,Pb)2Sr2CaCu2O8+δ at the antinodal point. *Physical Review B*, 74(16):165102, October 2006, doi:10.1103/PhysRevB.74.165102. (Cited on pages 49 and 55.)

[89] A. Varykhalov, M. Scholz, T. Kim, and O. Rader. Effect of noble-metal contacts on doping and band gap of graphene. *Physical Review B*, 82(12):121101, September 2010, doi:10.1103/PhysRevB.82.121101. (Cited on page 50.)

[90] C.-H. Park, F. Giustino, C. D. Spataru, M. L. Cohen, and S. G. Louie. Angle-resolved photoemission spectra of graphene from first-principles calculations. *Nano letters*, 9(12):4234–9, December 2009, doi:10.1021/nl902448v. (Cited on page 52.)

[91] M. Calandra and F. Mauri. Electron-phonon coupling and electron self-energy in electron-doped graphene: Calculation of angular-resolved photoemission spectra. *Physical Review B*, 76(20):205411, November 2007, doi:10.1103/PhysRevB.76.205411. (Cited on pages 55 and 56.)

[92] J. González and E. Perfetto. Many-body effects on out-of-plane phonons in graphene. *New Journal of Physics*, 11(9):095015, September 2009, doi:10.1088/1367-2630/11/9/095015. (Cited on page 56.)

[93] M. Hengsberger, D. Purdie, P. Segovia, M. Garnier, and Y. Baer. Photoemission study of a strongly coupled electron-phonon system. *Physical review letters*, 83(3):592–595, 1999. (Cited on page 57.)

[94] S. LaShell, E. Jensen, and T. Balasubramanian. Nonquasiparticle structure in the photoemission spectra from the Be (0001) surface and determination of the electron self energy. *Physical Review B*, 61(3):2371–2374, 2000. (Cited on page 57.)

[95] S. Badalyan and F. Peeters. Electron-phonon bound state in graphene. *Physical Review B*, 85(20):205453, May 2012, doi:10.1103/PhysRevB.85.205453. (Cited on page 57.)

[96] A. Grüneis, C. Attaccalite, T. Pichler, V. Zabolotnyy, H. Shiozawa, S. Molodtsov, D. Inosov, A. Koitzsch, M. Knupfer, J. Schiessling, R. Follath, R. Weber, P. Rudolf, L. Wirtz, and A. Rubio. Electron-Electron Correlation in Graphite: A Combined Angle-Resolved Photoemission and First-Principles Study. *Physical Review Letters*, 100(3):037601, January 2008, doi:10.1103/PhysRevLett.100.037601. (Cited on page 60.)

[97] Y. Dedkov, M. Fonin, U. Rüdiger, and C. Laubschat. Rashba Effect in the Graphene/Ni(111) System. *Physical Review Letters*, 100(10):107602, March 2008, doi:10.1103/PhysRevLett.100.107602. (Cited on page 60.)

[98] A. de Parga, F. Calleja, B. Borca, M. Passeggi, J. Hinarejos, F. Guinea, and R. Miranda. Vázquez de Parga et al. Reply:. *Physical Review Letters*, 101(9):99704, August 2008, doi:10.1103/PhysRevLett.101.099704. (Cited on page 60.)

[99] P. W. Sutter, J.-I. Flege, and E. a. Sutter. Epitaxial graphene on ruthenium. *Nature materials*, 7(5):406–11, May 2008, doi:10.1038/nmat2166. (Cited on page 60.)

[100] S. Y. Zhou, G.-H. Gweon, A. V. Fedorov, P. N. First, W. A. de Heer, D.-H. Lee, F. Guinea, A. H. Castro Neto, and A. Lanzara. Substrate-induced bandgap opening in epitaxial graphene. *Nature materials*, 6(10):770–5, October 2007, doi:10.1038/nmat2003. (Cited on page 60.)

[101] K. Novoselov. Mind the gap. *Nature materials*, 6:720, 2007. (Cited on page 60.)

[102] G. Panaccione, I. Vobornik, J. Fujii, D. Krizmancic, E. Annese, L. Giovanelli, F. Maccherozzi, F. Salvador, A. De Luisa, D. Benedetti, A. Gruden, P. Bertoch, F. Polack, D. Cocco, G. Sostero, B. Diviacco, M. Hochstrasser, U. Maier, D. Pescia, C. H. Back, T. Greber, J. Osterwalder, M. Galaktionov, M. Sancrotti, and G. Rossi. Advanced photoelectric effect experiment beamline at Elettra: A surface science laboratory coupled with Synchrotron Radiation. *The Review of scientific instruments*, 80(4):043105, April 2009, doi:10.1063/1.3119364. (Cited on page 66.)

CURRICULUM VITÆ

Ivo Pletikosić was born in Sinj in 1977. Upon finishing his secondary education he moves to Zagreb to study physics at the Faculty of science. Graduating in both theoretical and experimental physics, he starts working as a research assistant in the group of dr. Petar Pervan at the Institute of physics in 2004, and becomes a postgraduate student in condensed matter physics at the Faculty of science in 2005. For three years he has been a teaching assistant at undergraduate courses in General physics I-IV.

Initially, his experimental research interest were electronic properties and many-body interactions in low dimensional systems, switching to the physics of graphene in 2008. He has contributed to four international conferences, and appears as a co-author at eight peer-reviewed articles.

LIST OF PUBLICATIONS:

1. I. Pletikosić, M. Kralj, M. Milun, and P. Pervan: *Finding the bare band: Electron coupling to two phonon modes in potassium-doped graphene on Ir(111)*. Physical Review B. 85 (2012), 155447

2. V. Mikšić Trontl, I. Pletikosić, M. Milun, and P. Pervan: *Temperature dependence of photo-hole decay in 4d derived Quantum Well States in monolayer Ag(111) films on Pd(111), Ni(111), Mo(110) and Cu(100)*. Surface science. 606 (2012), 840

3. M. Kralj, I. Pletikosić, M. Petrović, P. Pervan, M. Milun, A. N'Diaye, C. Busse, T. Michely, J. Fujii, and I. Vobornik: *Graphene on Ir(111) characterized by angle-resolved photoemission*. Physical Review B. 84 (2011), 075427

4. I. Pletikosić, M. Kralj, D. Šokčević, R. Brako, P. Lazić, and P. Pervan: *Photoemission and DFT study of Ir(111); energy band gap mapping*. Journal of physics. Condensed matter. 22 (2010), 135006

5. I. Pletikosić, M. Kralj, P. Pervan, R. Brako, J. Coraux, A. N'Diaye, C. Busse, and T. Michely: *Dirac Cones and Minigaps for Graphene on Ir(111)*. Physical Review Letters. 102 (2009), 056808

6. I. Pletikosić, V. Mikšić Trontl, M. Milun, D. Šokčević, R. Brako, and P. Pervan: *d-band quantum well states in Ag(111) monolayer films; substrate-induced shifts*. Journal of Physics – Condensed Matter. 20 (2008), 355004

7. V. Mikšić Trontl, I. Pletikosić, P. Pervan, and M. Milun: *Atomic structure of surfaces and ultrathin films*. Croatica Chemica Acta. 79 (2006), 311

8. V. Mikšić Trontl, I. Pletikosić, M. Milun, P. Pervan, P. Lazić, D. Šokčević, and R. Brako: *Experimental and ab initio study of the structural and electronic properties of subnanometer thick Ag films on Pd(111)*. Physical review B. 72 (2005), 235418

COLOPHON

This thesis was typeset in LyX using André Miede's `classicthesis` style for LaTeX.

The text face is *URW Palladio*, a font inspired by Hermann Zapf's *Palatino*. The typewriter text is set in *Bera Mono*, originally developed by Bitstream Inc. as *Bitstream Vera*.

Unless otherwise noted, all figures in the thesis were created by the author, using Wavemetrics IGOR Pro data analysis software, Grace 2D plotting tool, the Persistence of Vision Raytracer (POV-Ray), GNU Image Manipulation Program (GIMP) or Inkscape, a scalable vector graphics editor.

Printed in Zagreb, June 2012